

DOCTORAL THESIS

Weighing galaxy clusters on Stripe 82 through weak gravitational lensing

Author:

Maria Elidaiana DA SILVA PEREIRA

Advisor:

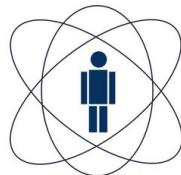
Dr. Martin MAKLER

*A thesis submitted in fulfilment of the requirements
for the degree of Doctor of Philosophy*

in the

Brazilian Center for Physics Research

Rio de Janeiro – September 2017



CBPF

**Centro Brasileiro de
Pesquisas Físicas**

Declaration of Authorship

I, Maria Elidaiana DA SILVA PEREIRA, declare that this thesis titled, 'Weighing galaxy clusters on Stripe 82 through weak gravitational lensing' and the work presented in it is my own. I confirm that this work submitted for assessment is my own and is expressed in my own words. Any uses made within it of the works of other authors in any form (e.g., ideas, equations, figures, text, tables, programs) are properly acknowledged at any point of their use. A list of the references employed is included.

Signed:

Date:

Abstract

Galaxy clusters are powerful tools to study the content and evolution of the Universe. Determining their abundances as a function of mass and redshift is one of the main observables for current and forthcoming surveys such as the *Dark Energy Survey* (DES) and the *Large Synoptic Survey Telescope* (LSST). Galaxy clusters act as gravitational lenses producing effects on the background sources such as shear (weak lensing), magnification and multiple images (strong lensing). The study of these effects enables us to obtain the mass distribution of the clusters without relying on assumptions about their physical and dynamical states. A widely used method to obtain average mass estimates of clusters is based on the measurements of the tangential shear profiles of the background sources, which can be converted to a projected mass density contrast and fitted by theoretical models, such as the *Navarro-Frenk-White* (NFW) profile. In this work we focus on the weak lensing mass measurements for galaxy clusters in the *CfTH Stripe 82 survey* (CS82) footprint and identified in the Sloan Digital Sky Survey (SDSS) by the redMaPPer and the Voronoi Tessellation (VT) algorithms. We present the first weak lensing calibration of μ_* , a new galaxy cluster mass proxy corresponding to the total stellar mass of red and blue members, in these two cluster samples: 230 redMaPPer clusters at redshift $0.1 \leq z < 0.33$ and 136 VT clusters at $0.1 \leq z < 0.6$. We use the CS82 shear catalog and stack the clusters in μ_* bins to measure a mass-observable power law relation. We show that our results are consistent, internally and with the literature, indicating that our method can be applied to any cluster finding algorithm. In particular, we have seen that μ_* is the suitable mass proxy for VT clusters. Catalogs including μ_* measurements will enable its use in studies of galaxy evolution in clusters and cluster cosmology. In the strong lensing regime we describe how to obtain a mass estimate for the galaxy clusters through the measurements of the curvature radius of gravitational arcs. This technique will be applied to systems with arcs in the SOAR Gravitational Arc Survey (SOGRAS). We also present the preliminary results for stacked weak lensing mass measurements of a sample of SOGRAS clusters in the CS82 footprint.

Dedicated to my grandma, Salustiana Maria da Silva, which could not see her first family member become a Ph.D., but I am sure if she was here she would be very proud. Thank you for everything, grandma.

Dedicado à minha avó, Salustiana Maria da Silva, que não pôde ver a primeira pessoa da família se tornar doutora, mas estou certa de que se estivesse aqui ela estaria muito orgulhosa. Obrigada por tudo, vó.

Acknowledgements

I thank my advisor Martin Makler for his supervision, since my undergrad until today. It has been long years of learning, discussions, frustrations, attempts and successes in this search for understanding nature. I am grateful to all your support, even in my most pessimistic moments. I have learned a lot during these years, thanks to your patience and because you believed in me. “What matters is that the derivative is positive”. Thank you for everything.

I would like to thank Marcelle Soares-Santos for the opportunity to go to Fermilab and to start to develop the work that is now the main topic of this thesis. Thank you for the collaboration, advices and supervision. As a women in science, you are a great example for me.

I also thank my Fermilab collaborators who welcomed me and provided excellent discussions and ideas: Jim Annis, Huan Lin, Antonella Palmese, Brian Welch and the astro people; as well my collaborators throughout the world: Aldeé Charbonnier, Bruno Moraes, André Vitorelli, Leandro Beraldo, Mariana Penna-Lima and the people from the CS82 collaboration and the SOGRAS team.

I am grateful to the [Bayesian] people in AstroHackWeek [un]conference, in particular, Phil Marshall, Katalin Takats, Lucas Secco, Oleg Burgueño and Franco N. Bellomo for their help in developing parts of the codes used for this thesis.

I would like to thank CNPq, Fermilab, IUPAP Women in Physics, Columbia University, LSST Corporation, GitHub Inc and École de Physique des Houches for the grants and financial support, which made this work possible.

Ich danke Felix für alle Liebe und Unterstützung in guten und schlechten Zeiten.

Gostaria de agradecer a todos os amigos que fizeram parte desta jornada, seja na pesquisa em si seja nas horas livres. São muitas pessoas, mas em especial gostaria de agradecer à Vanessa Guida, Mariana e ao pessoal de Curicica pelos momentos de diversão e por sempre acreditarem em mim; à Patota Feliz e Mechas Coloridas por aturar minhas frustrações e sempre dar a motivação necessária para eu continuar tentando, além das reuniões gastronômicas e momentos de diversão muito necessários para combater o estresse do dia-a-dia.

Agradeço também ao pessoal da UERJ (em especial Caio, Richard, Alex, Thiagão, Otávio, Gustavo, Aline, Laís, Paulinha) pelos pastéis gigantes, rodízios na Parmê e momentos de nostalgia de nosso tempo na querida e resistente UERJ; agradecimentos também ao pessoal antigo do CBPF, em especial à Daniele Tostes, Thamys, Bruno, Grasi, Edu, Bia, Rafaéis, aos strong lensing guys (Gabriel Caminha, Clécio, Carlos) e ao CosmoObs team, pelas discussões científicas e computacionais, QTO no sujinho e torneios de sinuca.

Finalmente, e mais importante, eu gostaria de agradecer a minha família por toda a compreensão e ajuda durante todos esses anos nesta minha jornada para obter o doutorado em Física. Eu tenho

muito orgulho de hoje poder dizer que depois de tanto esforço, renúncias e dedicação, eu, a Maria Elidaiana, a filha do porteiro José, filha da auxiliar de creche Maria Eliete, e cotista da UERJ vai se tornar Doutora sim! E se reclamar, vai ter mais! (não, brincadeira, não aguento outro doutorado).

Eu não poderia terminar sem deixar de agradecer ao povo brasileiro trabalhador, o que sofre todo dia para sobreviver e pagar seus impostos. Impostos estes que tornaram a realização deste trabalho possível. É deste povo que eu tenho orgulho e não de nossa elite financeira e política (e golpista), que sabe do valor da educação e faz de tudo para tirar isso de nosso povo. Mas eles não tiraram isso de mim. Por isso, agradeço às oportunidades criadas durante os governos de Luiz Inácio Lula da Silva e Dilma Rousseff, que tornaram possível a alguém como eu obter um Doutorado. E eu torço pelo dia em que pobre virar doutor não seja exceção, mas algo normal.

Fora Temer. Volta MCTI.

Contents

Declaration of Authorship	i
Abstract	ii
Acknowledgements	iv
Contents	vi
List of Figures	viii
List of Tables	ix
Abbreviations	x
1 Introduction	1
1.1 Historical review of Gravitational Lensing	4
1.2 Thesis Outline	8
2 Gravitational Lensing Theory	10
2.1 Gravitational lensing basics	10
2.1.1 Lens properties	11
2.1.2 The deflection angle	12
2.1.3 Distortion and magnification	13
2.2 Strong gravitational lensing	14
2.2.1 Lens models	14
2.2.1.1 SIS	14
2.2.1.2 Pseudo-elliptical and elliptical models	15
2.2.2 Gravitational lensing modeling	16
2.3 Weak gravitational lensing	17
2.3.1 From ellipticities to shear	17
2.3.2 Tangential and cross shear components	19
2.3.3 Density profiles and mass estimates	21
3 Astronomical Surveys	22
3.1 Sloan Digital Sky Survey	23

3.2	CFHT Stripe 82 Survey	23
3.3	SOAR Gravitational Arc Survey	25
3.4	Dark Energy Survey	25
3.5	VISTA-CFHT Stripe 82 Survey	26
4	WL Analysis and Mass Calibration	28
4.1	Measuring the tangential shear profile	28
4.1.1	Voronoi Tessellation lens catalog	28
4.1.1.1	Assigning the new mass proxy μ_*	30
4.1.1.2	Investigating cluster fragmentation	31
4.1.1.3	Redefining the cluster central galaxy	32
4.1.2	redMaPPer lens catalog	32
4.1.3	Source catalog with Lensfit	34
4.1.4	Density profile measurements	36
4.2	Profile-fitting of redMaPPer and VT clusters	39
4.3	Mass-calibration of redMaPPer and VT clusters	42
4.3.1	redMaPPer mass-richness relation	49
4.3.2	VT – μ_* mass-calibration	51
4.4	Matching redMaPPer and VT clusters	54
4.5	Weak lensing on SOGRAS	55
5	Summary	58
5.1	Imaging surveys	58
5.2	Strong lensing studies	59
5.3	Weak lensing mass-calibration of VT and redMaPPer clusters	60
A	Bayesian approach and MCMC	62
B	Strong Lensing studies	65
B.1	Arcs visual search in DES	65
B.2	Morphometric modeling with Mediatrix	65
C	List of publications and talks	69
	Bibliography	73

List of Figures

1.1	Image of the 1919 total solar eclipse in Sobral	5
1.2	Galaxy cluster MACS j1149.5+223 and the lensed Refsdal supernova	7
2.1	Gravitational Lensing geometry	11
2.2	Shear components	20
4.1	Example of a Voronoi Tessellation	29
4.2	Red sequence of the cluster Abell 1084	33
4.3	Redshift distributions of the redMaPPer and VT clusters	37
4.4	Triangle plots of the profile-fitting of z_{low} redMaPPer clusters in λ bins	43
4.5	Triangle plots of the profile-fitting of z_{low} redMaPPer clusters in μ_* bins	44
4.6	Triangle plots of the profile-fitting of z_{low} and z_{high} VT clusters in μ_* bins	45
4.7	$\Delta\Sigma$ measurements for z_{low} redMaPPer clusters in λ and μ_* bins	46
4.8	$\Delta\Sigma$ measurements for z_{low} VT clusters in μ_* bins	47
4.9	$\Delta\Sigma$ measurements for z_{high} VT clusters in μ_* bins	48
4.10	Comparison of the z_{low} redMaPPer mass-richness relation with literature	51
4.11	Mass-calibration for z_{low} redMaPPer clusters in μ_* bins	52
4.12	Mass-calibration for z_{low} VT clusters in μ_* bins	53
4.13	Mass-calibration for z_{high} redMaPPer clusters in μ_* bins	54
4.14	Sky distribution of SOGRAS clusters in the CS82 footprint.	56
4.15	Best-fit results for SOGRAS clusters in different bins of z and richness N_{gals}	57
B.1	DES images of six strong lensing systems	66
B.2	Steps in the Mediatrix Filamentation method	67
B.3	Input image of Mediatrix	68

List of Tables

4.1	Binning scheme and properties of the redMaPPer clusters	37
4.2	Binning scheme and properties of the VT clusters	37
4.3	Summary of the systematics in the WL analysis	41
4.4	Best-fit results for redMaPPer clusters and for VT clusters	49
4.5	Results of the z_{low} redMaPPer mass-richness relation comparison with literature . .	50
4.6	Summary of mass- μ_* calibration for redMaPPer and VT clusters	53
4.7	Preliminary results for SOGRAS cluster weak lensing masses	56

Abbreviations

BCG	Brightest Cluster Galaxy
BPZ	Bayesian Photometric Redshifts
CAMIRA	Cluster finding Algorithm based on Multi-band Identification of Red-sequence gAlaxies
CCD	Charge–Coupled Device
CFHT	Canada–France–Hawaii Telescope
CFHTLens	CFHT Lensing Survey
CS82	CFHT Stripe 82 Survey
CTIO	Cerro Tololo Inter–American Observatory
DECam	Dark Energy Camera
DES	Dark Energy Survey
DR	Data Release
GMOS	Gemini Multi-Object Spectrograph
GREAT	GRAVitational Enlightenment Accuracy Testing
HSC	Hyper Suprime-Cam
KiDS	Kilo–Degree Survey
KSB	Kaiser, Squires and Broadhurst algorithm
MCMC	Markov Chain Monte-Carlo
NIR	Near Infrared
NFW	Navarro–Frenk–White
PSF	Point Spread Function
PSFEx	Point Spread Function Extractor
redMaPPer	red–sequence Matched–filter Probabilistic Percolation
SDSS	Sloan Digital Sky Survey
SExtractor	Source Extractor
SIS	Singular Isothermal Sphere

SOGRAS	SOAR GRavitational Arc Survey
S-PLUS	Southern Photometric Local Universe Survey
STEP	Shear TEsting Programme
SV	Science Verification
UKIDSS	UKIRT InfraRed Deep Sky Survey
VICS82	VISTA–CFHT Stripe 82 Survey
VIRCAM	VISTA InfraRed CAMera
VISTA	Visible and Infrared Survey Telescope for Astronomy
VT	Voronoi–Tessellation
WIRCam	Wide-field InfraRed Camera
XCS	X-ray Correlation Spectroscopy
XMM	X-ray Multi–Mirror

Chapter 1

Introduction

Galaxy clusters are the largest and most massive gravitationally bound structures in the Universe. They are formed by a large number of galaxies (30–300 in rich clusters, usually with one large elliptical central), hot gas and dark matter evolving in strongly coupled processes. Cluster properties depend on both the dynamical processes that take place inside them and on the evolution of the Universe. As such they can be used as a powerful tool to probe its content, to study the formation and evolution of structures, and to test modified gravity theories [Haiman et al. 2001, Voit 2005, Allen et al. 2011, Kravtsov and Borgani 2012, Ettori and Meneghetti 2013, Penna-Lima et al. 2014, Harvey et al. 2015, Menci et al. 2016, Pizzuti et al. 2016]

Galaxy clusters also act as powerful gravitational lenses. Their intense gravitational fields generate distortions in the shape (shear) of the background galaxies (sources) and may produce giant arcs and multiple images. The former effect is known as the weak lensing regime and occurs in the outer regions of the galaxy clusters, and the later, known as strong lensing regime occurs in the central regions of the clusters. However, the strong lensing effects are rare due to the necessary alignment between the observer, the intervening matter distribution (i.e. the lenses) and the sources. The most common effect is due to shear in the weak lensing regime, which is the regime we will focus on this work. Through this effect we can assess the mass distribution of the galaxy clusters to use them as cosmological tools [Schneider 2005].

At the depths of ongoing and planned wide-field surveys, it is not possible to measure this signal from individual clusters, except for the most massive ones. However, we can combine the lensing signal of a large number of clusters to obtain a higher signal-to-noise. This *stacking* procedure requires

the large statistics enabled by wide-field surveys such as the Dark Energy Survey¹ (DES; [Jarvis et al. 2016](#), [Melchior et al. 2017](#)), the Canada–France–Hawaii–Telescope (CFHT) Lensing Survey² [CFHTLens; [Velander et al. 2014](#), [Ford et al. 2015](#), [Kettula et al. 2015](#)], the Sloan Digital Sky Survey [SDSS; [Sheldon et al. 2001](#), [Simet et al. 2012](#), [Wiesner et al. 2015](#), [Gonzalez et al. 2017](#), [Simet et al. 2017](#)], and the Kilo-Degree Survey³ [KiDS; [de Jong et al. 2013](#), [Kuijken et al. 2015](#)].

Clusters can be identified in several wavelengths such as in X-rays, radio and optical. In particular, the identification in the optical can be made through the search for overdensities (from matched-filters to more complex Voronoi tessellations) of multi-band optically detected galaxies. These multi-band optical cluster catalogs usually provide good cluster photometric redshifts (photo-z), which are crucial information for weak lensing measurements.

Observationally, galaxy clusters are ranked not by the mass of the halo but by some proxy for mass. A mass-observable relation must be calibrated in order to make the connection between the observable and the true halo mass. The technique of stacking the weak lensing signal for many systems within a given observable interval provides one of the most direct and model independent ways to accurately calibrate such mass-observable scaling relations. Many efforts have been made to determine the scaling relations empirically using an observable mass proxy for the cluster mass. However, comparing the empirical measurements is challenging since there are several methods to identify the clusters, which lead to different cluster samples, and different definitions of the mass proxy to be used [[Johnston et al. 2007](#), [Oguri 2014](#), [Ford et al. 2015](#), [Wiesner et al. 2015](#), [Simet et al. 2017](#)].

In this work we use the stacked weak lensing technique on galaxy clusters identified by two different algorithms to estimate their mass and to obtain the scaling relations for two different mass proxies. The clusters are identified by the red-sequence Matched-filter Probabilistic Percolation⁴ [redMaPPer; [Rykoff et al. 2014](#)] optical cluster finder and the geometric Voronoi Tessellation⁵ algorithm [VT; [Soares-Santos et al. 2011](#)] in the Sloan Digital Sky Survey (SDSS) Stripe 82 region. We use the weak lensing shear catalog from the CFHT Stripe 82 Survey [CS82; [Moraes et al. 2014](#), [Erben et al. 2018](#)], which has excellent image quality and thus we expect our mass estimates to be less affected by shape systematics than the results obtained from the SDSS data alone (e.g. [Gonzalez et al. in](#)

¹<https://www.darkenergysurvey.org/>

²<http://www.cfhtlens.org/>

³<http://kids.strw.leidenuniv.nl/>

⁴<https://github.com/erykoff/redmapper>, version 0.0.0.0

⁵<https://github.com/soares-santos/vt>, v1.11

prep.). In our analysis, we obtain the scaling relations for both the redMaPPer optical richness λ [Rykoff et al. 2012, 2014] and for a new mass proxy μ_* [Palmese et al. 2018, Welch et al. 2018].

The new mass proxy μ_* is defined as the sum of the stellar masses of cluster galaxies weighted by their membership probabilities. This quantity can be estimated reliably from optical photometric surveys [Palmese et al. 2016] and shows a tight correlation with the total cluster mass [e.g. Andreon 2012]. Palmese et al. [2018] perform a matching between redMaPPer DES clusters and XMM X-ray clusters at a redshift (z) range of $0.1 < z < 0.7$ and demonstrate that μ_* has low scatter with respect to X-ray mass observables. They compute the scaling relation between the X-ray temperature (T_X) and this new mass proxy, $T_X - \mu_*$, obtaining a scatter of $\sigma_{\ln T_X | \mu_*} = 0.20$, which is comparable with results found for the redMaPPer richness estimator λ by Rykoff et al. [2016] using XMM and Chandra X-ray samples at $0.2 < z < 0.9$ and by Rozo and Rykoff [2014] using the XCS X-ray sample at $0.1 < z < 0.5$.

When using the redMaPPer mass-proxy λ , we obtain a $M_{200} - \lambda$ relation that is consistent with previous measurements found in the literature. When using μ_* on the same sample our results show a similar level of uncertainty. Our results for the VT sample on the same redshift range are consistent with those we obtain with redMaPPer, showing that our mass calibration is robust against the specifics of the cluster selection algorithms. Finally, we extend our analysis to a higher redshift VT sample. We do not see evolution of the mass-observable relation at the level of precision of this analysis.

Although the weak lensing mass-calibration of redMaPPer and VT clusters is the main topic of this thesis, I also will describe some other analyses in which I have been involved such as the weak and strong lensing measurements in the SOGRAS survey, my participation in a visual arc search in DES survey, and tests and validation of detection and morphology catalogs in the VICS82 and CS82 surveys.

In the next sections we present a brief historical review of the gravitational lensing effect and the outline of this thesis. In this work, the distances are expressed in physical coordinates, magnitudes are in the AB system and we assume a flat Λ CDM cosmology with $\Omega_m = 0.3$ and $H_0 = 100 h \text{ km s}^{-1} \text{Mpc}^{-1}$.

1.1 Historical review of Gravitational Lensing⁶

In 1704, Isaac Newton conceptually speculated on the possibility of light deviation by massive bodies. In the year 1783, astronomer John Mitchell based on Newton's speculations developed a method for measuring the mass of a star through the decrease of the speed of light due to the star's gravitational field. He sent a letter about this method to Henry Cavendish, who applied it to calculate the light deflection⁷ angle $\hat{\alpha}$ given by

$$\hat{\alpha} = \frac{2GM}{c^2 r}, \quad (1.1)$$

where G is the universal gravitational constant, c is the speed of light in vacuum and r is the minimum distance from the light ray to the object with mass M (impact parameter). But this result was not published. Only in 1801 Johann von Soldner published the first work on this topic and is therefore considered the first to explore the deflection of light to infer that the light rays are deflected from an angle $\hat{\alpha} = 0.83''$ by passing near the disk of the Sun [Jaki 1978]. However, the ideas based on the corpuscular nature of light were no longer popular at this time and these results did not have much repercussion.

A century later, in 1911, using the *Equivalence Principle* Albert Einstein was able to repeat von Soldner's calculations and obtained the same value for the deflection angle [Einstein 1911]. He also proposed that this angle could be measured during a solar eclipse and the first attempt was made in 1912 in Brazil by an Argentinian expedition to the city of Cristina, in the south of Minas Gerais, led by Carlos Dillon Perrine. On this occasion the weather prevented the observations [Moreira and Videira 1995]. The second attempt occurred in 1914, when Erwin Freundlich directed an expedition to the Crimean Peninsula in Russia. However he and his team were detained because of World War I [Cornell and Lightman 1983].

In 1915, with the *General Relativity* theory developed, Einstein remade his calculations of the light deflection angle in the vicinity of the Sun and this time he obtained

$$\hat{\alpha} = \frac{4GM}{c^2 r}, \quad (1.2)$$

which is twice its first result (as well the Newtonian result), leading to an approximate deviation of $1.7''$ near by the solar disk [Einstein 1916]. However, it was only with the 1919's eclipse (see Figure

⁶This historical review was largely based on the content of the masters dissertations of Caminha [2009], Pereira [2012] and the Ph.D. thesis of Montoya [2011]. Some changes and updates have been added.

⁷Assuming a corpuscular nature for the light and that the acceleration of the bodies in a gravitational field is independent of their masses.

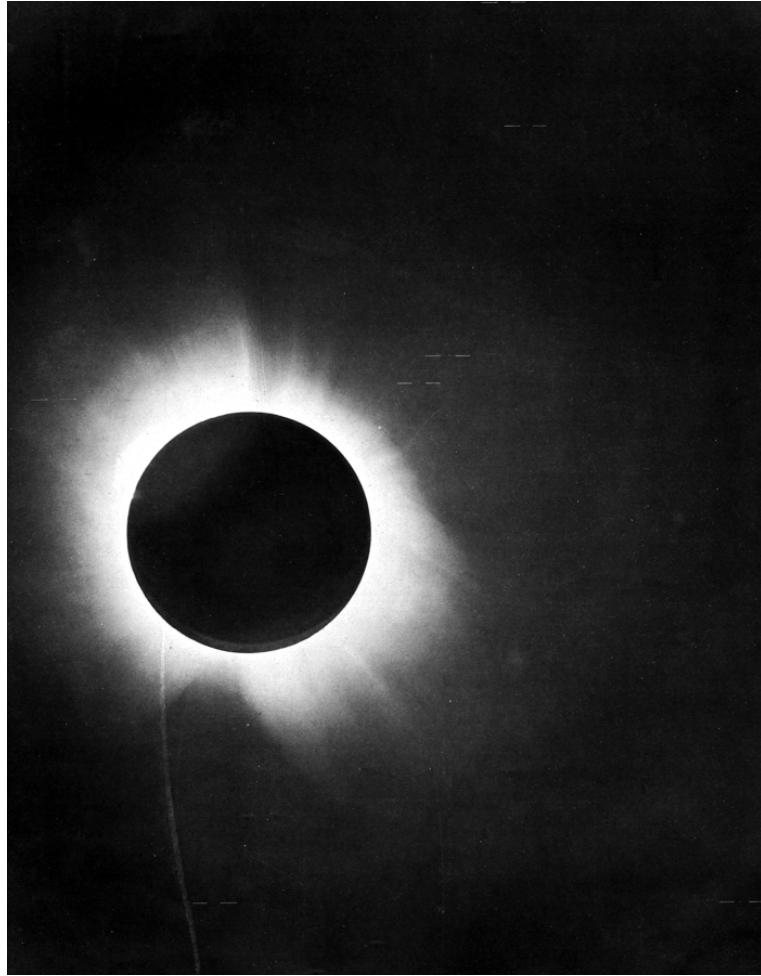


FIGURE 1.1: Plate 1 image with the 4-inch lens of the 1919 total solar eclipse, observed in Sobral, Brazil. The white lines show the positions of the identified stars that would be used for measuring the light deflection due to the presence of the Sun. Credits: Royal Society of London/Dyson, Eddington, Davidson.

1.1) that the expeditions to Sobral, Ceará (northeast of Brazil), and Príncipe Island (West Africa) could prove that the Einstein’s result was correct. This experiment became the most famous test of General Relativity [Dyson et al. 1920].

Until that moment the studies focused only in the light deflection effect, however, in 1921 Arthur Eddington mentioned the possibility of the formation of multiple images if two stars are sufficiently well aligned [Eddington 1921]. Three years later, the Russian physicist Orest Chwolson published a brief communication describing the idea of an “imaginary double star” [Chwolson 1924]. In this work, he describes that a second image forms near to the star that cause the light deflection, so that is not possible to detect them separately. He even noticed that in the case of perfect alignment between the observer and the stars, a ring-shaped image centered on the foreground star should result. Nowadays this effect is known as “Einstein ring”.

In 1936, Einstein published a brief article in Science magazine describing the same results obtained by Chwolson, however, he additionally discusses the increase in the brightness of the lensed object. In this work he also introduces the theoretical foundation of gravitational lensing: lens equation, double images and magnification [Einstein 1936].

In the following year, the Swiss astronomer Fritz Zwicky postulated that extragalactic objects (e.g. galaxy and galaxy clusters) and not only stars act as lens [Zwicky 1937a,b]. This enabled the gravitational lensing phenomena to change from a simple curiosity to a potential astronomical tool. Unfortunately, it seems there was no interest from the scientific community to search for this phenomenon by that time.

After a long time with almost no work in the field, the gravitational lensing was once again discussed after the discovery of the first quasar in 1963 [Schmidt 1963], when Jean M. Barnothy was the first to connect that class of objects with the lensing phenomena [Barnothy 1965]. He noticed that quasars would be ideal sources to be lensed by an detectable extragalactic object, because of their spectral peculiarities, high redshift, extreme luminosity and point-like shape.

Since then, many theoretical aspects of gravitational lensing were developed. However, this was not enough to perform a systematic search for gravitational lensing systems. Only in 1979 the first lensed object was observed [Walsh et al. 1979], a double image of a quasar. In the middle of the 1980s the first gravitational arcs were observed [Lynds and Petrosian 1986, Soucail et al. 1987], which is the result from the lensing of extended sources, i.e., galaxies that are lensed by massive galaxies or galaxy clusters.

In 1989 the first microlensing of a quasar was observed [Irwin et al. 1989]. This event occurs when the source passes through a region where the lens significantly increases its brightness. Shortly before, ring-shaped radio sources were observed [Hewitt et al. 1988].

Finally, around two hundred years after the first calculations of the light deflection by a star, the first microlensing event by a star was observed [Alcock et al. 1993]. In 2004 the first extrasolar planet was discovered by means of the same technique [Bond et al. 2004]. Until now 62 planets were discovered with this technique⁸

A very important contribution for the gravitational lensing studies came from the launch of the Hubble Space Telescope (HST), which allowed the first identification of strong lensing systems through the galaxy-galaxy lensing effect behind Abell 2218 [Kneib et al. 1996]. After many advances in this

⁸Interactive Extrasolar Planets Catalog: <http://exoplanet.eu/catalog-microlensing.php>

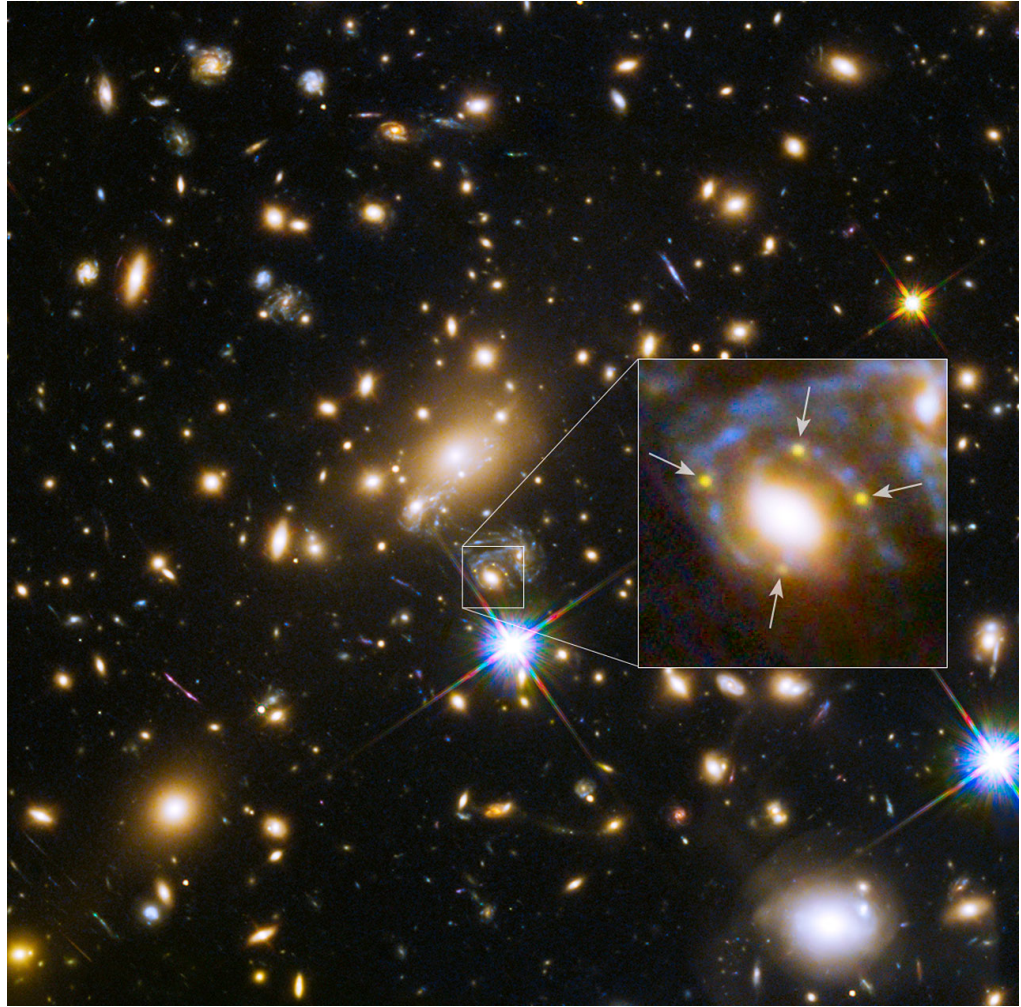


FIGURE 1.2: Galaxy cluster MACS j1149.5+223 and a supernova four times over, in a formation known as Einstein cross. Credits: NASA, ESA, S. Rodney (JHU) and the FrontierSN team; T. Treu (UCLA), P. Kelly (UC Berkeley) and the GLASS team; J. Lotz (STScI) and the Frontier Fields team; M. Postman (STScI) and the CLASH team; and Z. Levay (STScI).

field, surprisingly, in 2015 the first lensed supernova was discovered in the HST imaging [Kelly et al. 2015]. Such type of system was hypothesized by Refsdal [1964]. The discovered system has four images of a single supernova forming an Einstein cross configuration around an elliptical galaxy in the MACS J1149.6+2223 cluster, as shown in Figure 1.2.

In recent years, many astronomical surveys have been carried out and planned, which specifically focus on the weak gravitational lensing effect. The projects CS82 and DES were particularly good for this purpose because they are relatively deep, have very good image quality and cover large areas of the sky. Therefore they enable a large number of background galaxy sources to have their shapes precisely measured. From the shapes of these sources we measure the lensing signal to infer the amount of matter in the foreground lens (e.g. a galaxy cluster). The lensing effect is not only sensitive to the visible (barionic) matter but also to the dark matter in the lens. Once we have the

weak lensing mass of the cluster we can compare it to its stellar mass, for example, since the stellar mass inside a dark matter halo can be expected to trace the dark matter halo mass.

1.2 Thesis Outline

In the previous section we have noted that the gravitational lensing has become a very important tool to probe the matter distribution in the Universe. The lensing studies can be carried out in different regimes and scales. In this thesis our main focus will be the measurements in the weak lensing regime. In this regime we are able to perform a statistical measurement of the lensing signal by background sources around galaxy clusters with higher significance. Once we measure the signal we can obtain a weak lensing mass estimate for these galaxy clusters and compare with the visible mass provided by some proxy (e.g. stellar mass, richness) in order to have a mass calibration for these clusters. In this work we use two mass proxies that rely on different assumptions to quantify the visible matter content of the clusters. We want to verify if the choice of a given mass proxy present some bias in the mass measurements.

Besides the weak lensing, we also present a few steps we performed in the strong lensing regime, in addition to some tests and validations for the detection and morphological measurements of objects in astronomical surveys. In the theoretical chapter we will present the general aspect for both regimes, but the main chapters are dedicated to the weak lensing measurements, while the strong lensing work is presented as an appendix, since it is still in an early stage of development.

This thesis is distributed as follows:

- in Chapter 2 we present a brief review of the gravitational lensing theory starting from the basic principles to obtain the lensing observables, for both the weak and strong lensing regimes. We start from the Lens Equation and derive properties such as the shear and magnification. At the end, we summarize the observables with a special attention to the average tangential shear profile in the weak regime;
- in Chapter 3 we describe the astronomical surveys and data we use throughout this thesis with particular focus on the CS82 and SDSS surveys, in which we perform our main analyses. In the case of the CS82 survey I have participated in the generation and validation of the detection catalogs as well the morphology catalogs with a combination of SExtractor and PSFEx codes. The detection catalog was the starting point for several analyses in the survey including the

shape measurements with Lensfit, performed by collaborators. This shape catalog is the one used in my weak lensing analysis in this thesis.

- in Chapter 4 we focus on the mass estimates for galaxy cluster samples from two different catalogs: one that identifies the clusters by the search for red-sequences and one that uses the geometric technique of the Voronoi Tessellation (VT). The former is implemented by redMaPPer and the later by the VT algorithm. The mass estimates for these two cluster samples are performed through a weak lensing analysis. From the average masses derived for clusters binned in observable quantities we derive mass-observable relations, i.e., a mass-calibration for the samples. We do so for two different mass proxies: the redMaPPer- λ and VT- μ_* . This is the main result from this thesis. In this Chapter, we also describe an additional analysis in which we have searched for galaxy clusters with a large fraction of stellar forming galaxies (“blue clusters”) by the matching between the catalogs. We also present a weak lensing analysis we started to develop in the SOGRAS survey.
- in Chapter 5 we present the summary and a discussion of the measurements and projects developed in this thesis.
- in Appendix A we present a small review of the Bayesian inference basic principles and its association with the Markov chain Monte-Carlo technique and Metropolis-Hastings algorithm, which were used in our profile-fitting of the weak lensing profiles.
- in Appendix B we describe the strong lensing studies developed: the DES visual search for strong lensing systems and first steps to obtain cluster mass estimates via the curvature radius derived by the Mediatrix method.
- Finally, Appendix C contains the list of publications of the author and a list of talks presented during the development of this thesis.

Chapter 2

Gravitational Lensing Theory

The gravitational lensing theory is based on one of the main predictions of the Einstein's General Relativity theory, in which the light rays are deflected when propagating through an inhomogeneous medium. Formally, the light propagates along null geodesics as described by the perturbed Friedmann–Robertson–Walker (for the Standard Cosmological Model case). In most cases of importance to astrophysics, the lensing equations can be linearised and the light ray propagation is well described when adopting the *weak field* and *small angle* approximations. For a description of the lensing by clusters and individual galaxies the *thin lens* approximation is often used, and is equivalent to assuming that the deflection of light occurs in a single plane in which the lens is located. For the lensing by galaxies and clusters this approximation is sufficient, since the deflecting mass is located in a very small region in comparison to the distance between observer and source.

In the next sections, widely based on the references [Bradac 2004](#), [Pereira 2012](#), [Caminha 2014](#), I will present a brief review of the Gravitational Lensing theory, from the basic aspects to the observables of the weak and strong regimes. For a more formal literature in the topic, see the references: [Refsdal 1964](#), [Blandford and Narayan 1986](#), [Schneider et al. 1992](#), [Refsdal and Surdej 1994](#), [Narayan and Bartelmann 1996](#), [Petters et al. 2001](#) and [Mollerach and Roulet 2002](#).

2.1 Gravitational lensing basics

The geometry of the gravitational lensing is presented in Figure 2.1 where we place the matter distribution in the deflector's plane \mathcal{D} at a redshift z_d , corresponding to an angular diameter distance D_d of observer \mathcal{O} . The source is located in the source plane \mathcal{S} , at a redshift z_s , with angular diameter

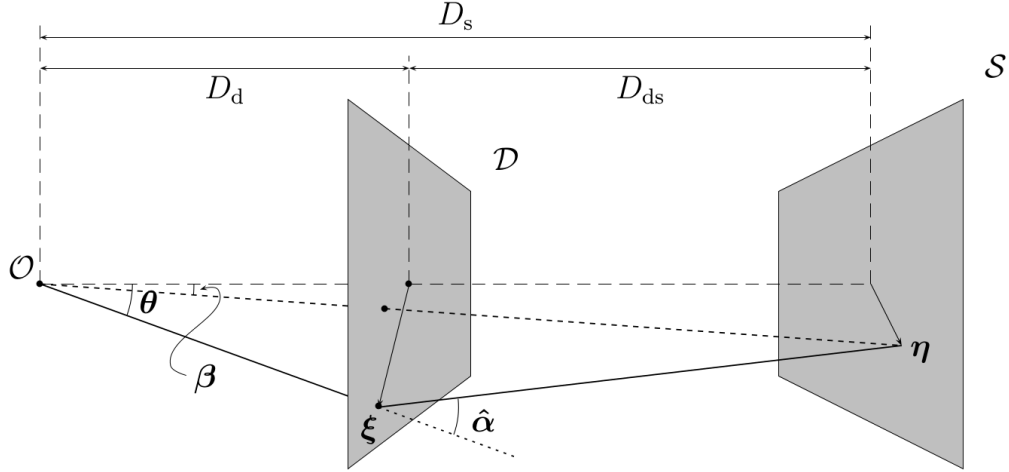


FIGURE 2.1: Typical geometry of a gravitational lensing scheme. Credits: [Bradac \[2004\]](#).

distances D_s to the observer and D_{ds} to the lens. Following the thin lens approximation, the light ray between the observer and the lens planes and between the lens plane and source plane is described by a geodesic in the homogeneous background metric. The effects of the space-time curvature due to an approximately homogeneous universe are incorporated into the angular diameter distances [Petters et al. \[2001\]](#). The deflection of the light ray when passing by the plane \mathcal{D} is represented by the deflection angle vector $\hat{\alpha}$, which depends on the mass distribution in the lens plane and on the impact vector ξ .

2.1.1 Lens properties

The optical axis can be defined as the line connecting the observer and the center of the lens (the choice of the optical axis is arbitrary). The source should be viewed at an angular position β with respect to the optical axis in the absence of the lens. We denote by η the distance from the source to the optical axis in the source plane and by ξ the “impact parameter” (or impact vector) in the lens plane. With these simple geometric considerations and assuming a single lens plane, we can write

$$\eta = \frac{D_s}{D_d} \xi - D_{ds} \hat{\alpha}(\xi), \quad (2.1)$$

or equivalently

$$\beta = \theta - \frac{D_{ds}}{D_s} \hat{\alpha}(D_d \theta) = \theta - \alpha(\theta), \quad (2.2)$$

which is called the *lens equation*. $\boldsymbol{\alpha}$ is referred as the reduced deflection angle. The lens equation provides us the angular position $\boldsymbol{\theta}$ in which we see the lensed images for a given source that is located in $\boldsymbol{\beta}$. The reduced deflection angle $\boldsymbol{\alpha}(\boldsymbol{\theta})$ commonly depends on $\boldsymbol{\theta}$ non-linearly, and then it is possible to obtain multiple solutions of $\boldsymbol{\theta}$ for a single source position $\boldsymbol{\beta}$ (multiple images).

2.1.2 The deflection angle

As previously mentioned, the thin lens approximation is valid when the characteristic size of the lens is much smaller than the cosmological distances involved. Thus, instead of using the three-dimensional distribution of the density of matter, we can use its projection, $\Sigma(\boldsymbol{\xi})$, in the lens plane (i.e., integrating along the line of sight), that is

$$\Sigma(\boldsymbol{\xi}) \equiv \int dr_3 \rho(\boldsymbol{\xi}, r_3). \quad (2.3)$$

The properties of the lens mass distribution appear in the lens equation only in the form of the deflection angle $\boldsymbol{\alpha}$, which in turn depends on the projected mass density $\Sigma(D_d \boldsymbol{\theta})$ and on the system's geometry, i.e. the angular diameter distances between source, observer and the lens. The strength of the lens can be described in terms of a dimensionless surface mass density $\kappa(\boldsymbol{\theta})$, known as *convergence*, which is defined as

$$\kappa(\boldsymbol{\theta}) = \frac{\Sigma(D_d \boldsymbol{\theta})}{\Sigma_{crit}}, \quad (2.4)$$

where Σ_{crit} is the critical surface mass density given by

$$\Sigma_{crit} = \frac{c^2 D_s}{4\pi G D_d D_{ds}}, \quad (2.5)$$

which depends on the cosmological parameters through the angular-diameter distances.

For $\kappa \ll 1$ we are in the *weak lensing* regime. Under such regime it is not possible to produce multiple images. A sufficient condition (but not required) to produce multiple images is that $\kappa(\boldsymbol{\theta}) > 1$ for at least one $\boldsymbol{\theta}$. This regime is called *strong lensing*. We will discuss these regimes in more detail later. Writing $\boldsymbol{\alpha}$ in terms of κ we have

$$\boldsymbol{\alpha}(\boldsymbol{\theta}) = \frac{1}{\pi} \int_{\mathbb{R}^2} d^2 \boldsymbol{\theta}' \kappa(\boldsymbol{\theta}') \frac{\boldsymbol{\theta} - \boldsymbol{\theta}'}{|\boldsymbol{\theta} - \boldsymbol{\theta}'|^2}. \quad (2.6)$$

Since the lens equation 2.2 depends only on $\kappa(\boldsymbol{\theta})$ we cannot measure the surface mass density Σ without knowing Σ_{crit} , that is, without knowing the redshift of lens and source and the underlying cosmology.

The form of the equation 2.6 implies that the deflection angle can be written as the gradient of a potential

$$\boldsymbol{\alpha}(\boldsymbol{\theta}) = \nabla \psi(\boldsymbol{\theta}), \quad (2.7)$$

where

$$\psi(\boldsymbol{\theta}) = \frac{1}{\pi} \int_{\mathbb{R}^2} d^2\theta' \kappa(\boldsymbol{\theta}') \ln |\boldsymbol{\theta} - \boldsymbol{\theta}'|. \quad (2.8)$$

It can be shown that $\psi(\boldsymbol{\theta})$ satisfies the analogue of the Poisson equation of the Newtonian gravitational theory, i.e.,

$$\nabla^2 \psi(\boldsymbol{\theta}) = 2\kappa(\boldsymbol{\theta}). \quad (2.9)$$

2.1.3 Distortion and magnification

The lens equation can be linearized for a source with a size much smaller than the typical length at which the properties of the lens change. The mapping can be described by the Jacobian matrix $\mathcal{A}(\boldsymbol{\theta})$

$$\mathcal{A}(\boldsymbol{\theta}) = \frac{\partial \boldsymbol{\beta}}{\partial \boldsymbol{\theta}} = \delta_{ij} - \frac{\partial^2 \psi(\boldsymbol{\theta})}{\partial \theta_i \partial \theta_j} = \begin{pmatrix} 1 - \kappa - \gamma_1 & -\gamma_2 \\ -\gamma_2 & 1 - \kappa + \gamma_1 \end{pmatrix}, \quad (2.10)$$

where the complex quantity $\gamma = \gamma_1 + i\gamma_2$ is the *shear* and is defined as

$$\gamma_1 = \frac{1}{2}(\psi_{,11} - \psi_{,22}), \quad \gamma_2 = \psi_{,12} = \psi_{,21}. \quad (2.11)$$

Lensing locally transforms circular sources into ellipses with the semi-axes given by the eigenvalues of the Jacobian matrix $\mathcal{A}(\boldsymbol{\theta})$. The ratio of the solid angles that a source occupies in the source plane \mathcal{S} and in the lens plane \mathcal{D} is given by the determinant of the matrix \mathcal{A} , which corresponds to the inverse of the magnification factor μ , given by

$$\mu(\boldsymbol{\theta}) = \frac{1}{\det \mathcal{A}} = \frac{1}{(1 - \kappa)^2 - |\gamma|^2}, \quad (2.12)$$

where $\gamma \equiv \sqrt{\gamma_1^2 + \gamma_2^2}$. The eigenvalues of the matrix \mathcal{A}^{-1} are

$$\mu_1 = \frac{1}{1 - \kappa - \gamma}, \quad (2.13)$$

$$\mu_2 = \frac{1}{1 - \kappa + \gamma}. \quad (2.14)$$

Lensing preserves the surface brightness, so if an isophote in the source plane delimits a small enough area a (to apply a local linearization) the area delimited by the same isophote in the lensed image will be μa .

It is common to consider the limits of the strong and weak lensing regimes from the values of the convergence: $\kappa \ll 1$ (weak) and $\kappa \gtrsim 1$ (strong). Even if the lens is “strong” enough to produce multiple images, we can treat the background population of the sources either by using strong lensing (for sources that produce observable multiple images and using the images that are not independent) as well as the weak lensing principles (for all sources that are independent one another). In the ideal case, we could combine both methods to obtain better constraints on the lens properties.

2.2 Strong gravitational lensing

In the strong lensing regime multiple images are formed. Mathematically, this means that there are multiple solutions to the lens equation 2.2. In the following, we will sketch some aspects of the strong lensing formalism.

2.2.1 Lens models

In studies using analytic expressions for the lenses, axially symmetric, elliptical and pseudo-elliptical models are often used. In particular, two popular models for the radial density profile are given by the NFW [Navarro et al. 1996, see Sec. 4.2] and the Singular Isothermal Sphere (SIS; Tremaine and Gunn 1979). In this section we focus on the SIS models for pedagogical reasons.

2.2.1.1 SIS

In the SIS model the density profile is obtained by assuming a spherically symmetric matter distribution and the behavior of an ideal isothermal gas in hydrostatic equilibrium Kormann et al. [1994].

This model is convenient for modeling systems on galactic scales [Binney and Tremaine 1987] and its density distribution is given by

$$\rho(r) = \frac{\sigma_v^2}{2\pi G r^2}, \quad (2.15)$$

where σ_v is the one-dimensional velocity dispersion of the particles and r the distance to the center of the sphere. Calculating the projection of this density in the lens plane, we have

$$\Sigma(\xi) = \frac{\sigma_v^2}{2\pi G} 2 \int_0^\infty \frac{dz}{\xi^2 + z^2} = \frac{\sigma_v^2}{2G\xi}. \quad (2.16)$$

We see that the density diverges when $\xi \rightarrow 0$, and therefore this model is *singular*.

Solving the lens equation 2.2, the corresponding angular positions of the images are given by

$$\theta_\pm = \beta \pm \theta_E, \quad (2.17)$$

where θ_E is the *Einstein radius*, defined as

$$\theta_E = \sqrt{\frac{4GM(\theta_E)}{c^2} \frac{D_{ds}}{D_d D_s}}, \quad (2.18)$$

where $M(\theta_E)$ is the mass within the Einstein radius. Using suitable units, we can obtain the mass by this expression

$$M(\theta_E) \approx 1.1 \times 10^{14} M_\odot \left(\frac{\theta_E}{30''} \right)^2 \left(\frac{D_d D_s}{D_{ds} 1 \text{Gpc}} \right). \quad (2.19)$$

The angular separation between two images in the SIS case is $\Delta(\theta) = 2\theta_E$. In general, the Einstein radius defines the typical separation between multiple images.

2.2.1.2 Pseudo-elliptical and elliptical models

Most of the mass distribution models for gravitational lenses are constructed from spherically symmetric models, whose projections have circular symmetry. However, both simulations and observational data show that most galaxies and clusters have a triaxial structure, which can be roughly approximated by ellipsoids. The projection in a plane of an ellipsoid is an ellipse, and a significant part of these projections have ellipticity e (defined here as $e \equiv 1 - b/a$, where a and b are respectively the major and minor semi-axes) greater than 0.5, and therefore, it is essential to consider elliptical models.

For this sake it is common to replace the radial variable with one that is constant over ellipses (“elliptical coordinate”). By introducing the elliptical symmetry into the lens potential we build the so-called pseudo-elliptical models, which offer the possibility of obtaining analytic expressions for the deflection angle (since it is written in terms of the derivative of the potential). This is a good approximation for a wide range of ellipticities and masses, but for large values of e ($\gtrsim 0.5$) this approximation loses its physical meaning (the mass distribution becomes dumbbell shaped) and this approach does not adequately describe the lensing. In this case it is necessary to consider models with projected elliptical matter distribution, constructed by replacing the elliptical coordinate into the expression for the projected density profile. In this case it is generally not possible to obtain an analytical expression for the potential, requiring the use of numerical algorithms to compute the deflection angle and its derivatives. However, it is possible to obtain the derivatives of the lens potential in terms of simple integrals. These elliptical modes are more realistic, but on the other hand are more computationally expensive. The pseudo-elliptical models are simpler to compute, but are valid on a limited ellipticity range.

2.2.2 Gravitational lensing modeling

In systems with the formation of gravitational arcs and/or multiple images by the same source it is possible to model the mass distribution (or the lens potential) of the object that acts as a lens. An initial estimate for the mass of the lens can be obtained by using the Equation 2.19, in which we associate the curvature radius of the arc (distance to the center of the lens) with the Einstein radius. But we recall that this equation assumes axial symmetry of the lens and lens–source–observer alignment, providing an inner boundary for the mass in the more central region of the cluster.

The most accurate way to model the lens is by using the positions of multiple images. We can use this position information to compare a model of mass distribution of the lens with the observations, leaving the position of the source free. Thus, what is needed is to find the model of the lens that best reproduces the configuration of multiple images observed in a given system. For cases where we have gravitational arcs formed by the merging multiple images it is common to use the position of the arc’s brightness peaks to constrain the lens model. This modeling of the lens by the use of multiple images can be carried out both in the lens or source planes, with the first being the most precise form of modeling.

In order to perform the modeling in the lens plane we define the function

$$\chi_{lens}^2 := \sum_i \left(\frac{\theta^{obs} - \theta^{mod}(\beta, \Pi)}{\sigma_i^{obs}} \right)^2, \quad (2.20)$$

where the parameters to be determined by minimization are Π , the parameter of the lens, and β , the source position. Here, to calculate χ_{lens}^2 at a specific point it is necessary to invert the lens equation. Depending on the complexity of the model, the numerical inversion is not trivial and makes the mapping of the parameter space computationally expensive. However, this way of obtaining the lens parameters is more robust and does not require one to map the observational error σ^{obs} to the source plane.

2.3 Weak gravitational lensing

In the weak gravitational lensing regime it is not possible to visually identify the effects as in the case of the strong regime. The sources suffer a slight distortion in preferred directions, inducing an ellipticity on circular sources. However for this effect to be measured a large number of sources and precise measurements of their shapes are necessary, since the effect is very weak compared to the intrinsic ellipticity of the sources.

For the weak lensing analyses the starting point is the measurement of the ellipticity of the sources, which is connected to the lensing signal. From the measured ellipticities, in particular their tangential components, the mass profile of the lenses ($\Delta\Sigma$) can be estimated. In the following sections we will present a brief summary, deeply based on references [Figueiró \[2011\]](#) and [Pereira \[2012\]](#), on how to obtain the density profiles from the ellipticity of objects.

2.3.1 From ellipticities to shear

If a galaxy has elliptic isophotes with the same center, ellipticity and orientation, its shape and size can simply be defined in terms of the axial ratio and the area delimited by a given isophote. However, the shapes of faint galaxies may be quite irregular and not so well represented by ellipses. In this way, a definition of shape or ellipticity is necessary to take into account the irregularities of the images and that is well adapted to the observational data.

Considering an isolated galaxy with surface brightness $I(\theta)$ and choosing a coordinate system such that the first moments of surface brightness disappear, i.e., the origin of the coordinate system is

placed in the centroid of the light distribution, we define the second moments Q_{ij} of this galaxy as

$$Q_{ij} = \frac{\int d^2\theta W[I(\boldsymbol{\theta})]I(\boldsymbol{\theta})\theta_i\theta_j}{\int d^2\theta W[I(\boldsymbol{\theta})]I(\boldsymbol{\theta})}, \quad (2.21)$$

where $W[I(\boldsymbol{\theta})]$ is a suitably chosen weight function such that the shape of the source inside a limiting isophote contour would be obtained, for example, the Heaviside step function. The trace Q describes the size of the images, while the off-diagonal portion of Q contains information about ellipticities. From Q_{ij} we can define two complex ellipticities

$$\epsilon = \frac{Q_{11} - Q_{22} + 2iQ_{12}}{Q_{11} + Q_{22}} = \epsilon_1 + i\epsilon_2 \quad \text{and} \quad e = \frac{Q_{11} - Q_{22} + 2iQ_{12}}{Q_{11} + Q_{22} + 2(Q_{11}Q_{22} - Q_{12}^2)^{\frac{1}{2}}} = e_1 + ie_2. \quad (2.22)$$

Both have the same phase (because the numerator is the same), but different moduli (however, they can be converted one into the other). For an image with elliptic isophotes of axial ratio $r \leq 1$, we obtain

$$|\epsilon| = \frac{1 - r^2}{1 + r^2}; \quad |e| = \frac{1 - r}{1 + r}, \quad (2.23)$$

with $r = \frac{b}{a}$, where b is the semi-minor axis and a is the semi-major axis.

We can apply Equation 2.21 to the source and define a complex ellipticity in the source plane. The transformation of the source ellipticity ($\epsilon^{(s)}/e^{(s)}$) in the source plane to the ellipticity of the image (ϵ/e) in the lens plane is given by

$$\epsilon^{(s)} = \frac{-2g + \epsilon + g^2\epsilon^*}{1 + |g|^2 - 2\Re(g\epsilon^*)} \quad \text{and} \quad e^{(s)} = \begin{cases} \frac{\epsilon - g}{1 - g^*\epsilon}, & \text{if } |g| \leq 1 \\ \frac{1 - ge^*}{e^* - g^*}, & \text{if } |g| > 1, \end{cases} \quad (2.24)$$

where the reduced shear $g(\theta)$ is defined by

$$g(\theta) = \frac{\gamma(\theta)}{1 - \kappa(\theta)} = \frac{|\gamma|}{1 - \kappa} e^{2i\phi}, \quad \text{with } g \equiv g_1 + ig_2. \quad (2.25)$$

In the weak lensing regime, $\kappa \ll 1$ and $|\gamma| \ll 1$. Thus, the reduced shear is approximately equivalent to the shear, $|g| \sim |\gamma|$ and $g \ll 1$.

These expressions allow us to obtain the ellipticities of the images from the brightness distribution of the source galaxies, and therefore, relate the ellipticities to the induced gravitational shear. As mentioned, galaxies have irregular shapes (they are not intrinsically circular) and have ellipticities distributed in a wide range of values. Moreover, assuming a homogeneous and isotropic universe, there is no preferred direction to which galaxies tend to align. Therefore, the orientations of galaxy

shapes are randomly distributed, which leads to an expected value of the probability distribution of the intrinsic ellipticities equal to zero, when we average over many galaxies:

$$\langle \epsilon^s \rangle = \langle e^s \rangle = 0. \quad (2.26)$$

Thus, by measuring the ellipticities of distant galaxies in a given region we can obtain an unbiased estimate of the local shear field. Using the above assumptions, the relationship between ellipticities and induced shear is the following

$$\frac{\langle \epsilon \rangle}{2} = \langle e \rangle \approx g \approx \gamma. \quad (2.27)$$

Finally, in the weak lensing regime, the shape of a source galaxy is directly related to the induced shear according to

$$e = e_1 + ie_2 = (e_1^s + \gamma_1) + i(e_2^s + \gamma_2) \quad (2.28)$$

$$\epsilon = \epsilon_1 + i\epsilon_2 = (\epsilon_1^s + 2\gamma_1) + i(\epsilon_2^s + 2\gamma_2). \quad (2.29)$$

Since it is not possible to infer the induced shear of a single galaxy, the accuracy of the shear estimate depends on the number of galaxies within a given region, reflecting the statistical nature of the weak lensing measurement.

2.3.2 Tangential and cross shear components

As previously mentioned, in the case of a circularly symmetric lens, the effect of the lensing is to produce a deformation on the tangential and radial directions. The images will tend to be aligned along the tangential direction for positive mass concentrations (such as galaxies and galaxy clusters) and along the radial direction for negative mass concentrations (i.e. for underdensities, such as voids). Therefore, it is convenient to define a coordinate system that specifies these properties. The *tangential* and *cross* components of the shear are defined by

$$\gamma_t = -\Re[\gamma \times e^{-2i\phi}] \quad \text{and} \quad \gamma_x = -\Im[\gamma \times e^{-2i\phi}], \quad (2.30)$$

where ϕ is the polar angle between the horizontal axis and the position of the lensed object relative to the deflector, as shown in Figure 2.2. Equations (2.30) lead to the following expressions for the components

$$\gamma_t = -\gamma_1 \cos(2\phi) - \gamma_2 \sin(2\phi) \quad \text{and} \quad \gamma_x = \gamma_1 \sin(2\phi) - \gamma_2 \cos(2\phi). \quad (2.31)$$

From these equations we can see that, if $\gamma = \gamma_1$ and $\phi = 90^\circ$ there is tangential alignment (real and positive shear); if $\gamma = \gamma_1$ and $\phi = 0^\circ$ the alignment is radial (real, but negative shear). In both cases, the value of the cross component of the shear is zero, since the gravitation can only induce tangential or radial alignments, corresponding to the real part of the shear. If we get a cross shear, it means that other factors besides gravitation are contributing, such as telescope optics or galaxy alignments. Thus, a cross shear component is an important tool to check for systematic errors in the measurements. This decomposition in the tangential and cross components of the shear signal are commonly referred to E and B modes, respectively.

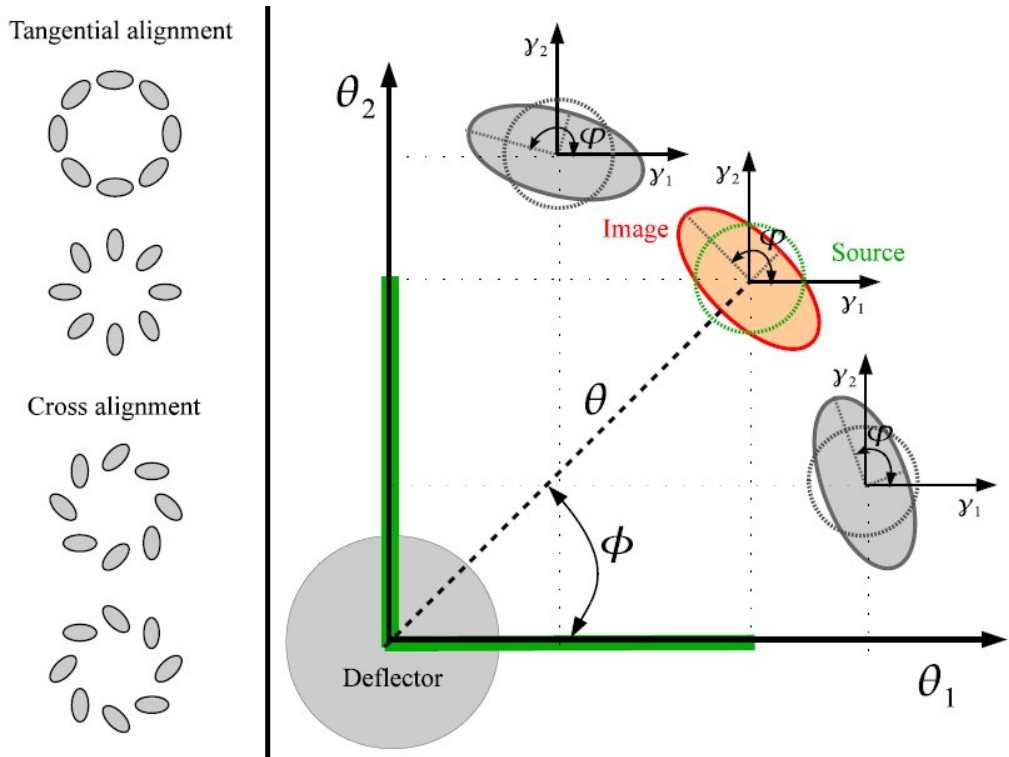


FIGURE 2.2: On the left we show the tangential and cross alignments in the weak lensing regime. Mass distributions can produce tangential or radial alignments (real part of shear), but cannot produce cross-alignments (imaginary part). Nonzero measurements for the cross shear component indicate systematic errors. On the right we show a source galaxy (green circle), which has a projected distance θ to the deflector. At the source plane, the galaxy has a circular shape. The weak lensing changes the shape of this galaxy, such that in the lens plane its image becomes an ellipse (red ellipse). In the Cartesian system, the shear γ is expressed in terms of the components γ_1 and γ_2 . In the tangential-cross coordinate system, the deflector is the reference point, such that the tangential and cross components are computed in terms of γ_1 , γ_2 and the phase ϕ . Credits: [Figueiró \[2011\]](#)

In the weak lensing regime, the measurement of the projected mass distribution (κ) of the lens from the shear signal (tangential component) is limited due to the so-called *mass sheet degeneracy*. This effect arises due to the fact that the observed quantity is not the shear itself, but the reduced shear. Therefore, two different mass distributions that differ by λ can not be distinguished by measuring

only the image distortions. In this case, the mass distribution is determined up to a constant, or formally [Falco et al. 1985, Schneider and Seitz 1995]: $\kappa \rightarrow \kappa' = \lambda\kappa + \kappa(1 - \lambda)$, where λ is an arbitrary constant. To break this degeneracy, we need to use additional information, such as assumptions about κ , magnification, etc.

2.3.3 Density profiles and mass estimates

The shear signal is obtained by combining the measurements made on background sources for many foreground lenses, grouping these lenses with similar properties (for example, in a same luminosity bin, in the case of galaxies, or richness interval for clusters). This is done in order to mitigate the problem of noise caused by the intrinsic shape of the sources and the limited number of sources per unit area. For any projected mass distribution, it is possible to show that the azimuthal average of the tangential shear at a projected radius R from the center of the distribution [Miralda-Escude 1991] is given by

$$\gamma_t(R) = \frac{\Delta\Sigma}{\Sigma_{crit}} \equiv \frac{\bar{\Sigma}(< R) - \langle \Sigma(R) \rangle}{\Sigma_{crit}}, \quad (2.32)$$

where $\Sigma(R)$ is the 2D projected mass density at radius R , $\bar{\Sigma}(< R)$ is the average value of Σ within a disk of radius R , $\langle \Sigma(R) \rangle$ is the azimuthal average of $\Sigma(R)$ in a thin ring of radius R and Σ_{crit} is given by Equation 2.5. We can then define the density contrast (i.e., average tangential profiles) as

$$\Delta\Sigma(R) \equiv \bar{\Sigma}(< R) - \langle \Sigma(R) \rangle = \gamma_t(R) \times \Sigma_{crit}. \quad (2.33)$$

As mentioned above, this quantity is not usually measured for an individual lens but for several lenses that present similar physical properties (e.g., richness, redshift) so that it is possible to increase the shear signal. This method is known as *stacking* of the tangential profiles. Thus, in practice, we obtain the ellipticities of the sources, calculate the shear γ and its components γ_t and γ_x from where it is possible to obtain the average tangential profiles.

To the measured average tangential profiles we can fit the theoretical density profiles of the clusters/halos and, finally, obtain estimates for the mass of these objects. This is the simplest way to obtain mass estimates from weak lensing since it is sufficient to use parametric models, such as NFW or Einasto [Einasto 1965, Merritt et al. 2006], to derive the mass and concentration of the clusters. When a model for the radial density profile is assumed, we can do the 2D projection of this model (i.e., calculate $\Delta\Sigma(R)$), fit to the measured $\Delta\Sigma(R)$ and determine the best fitting parameters.

Chapter 3

Astronomical Surveys

Imaging surveys are key to detect the gravitational lensing effects. In this thesis all the data for weak lensing analyses comes from surveys carried out on the so-called *Stripe 82*, which is an equatorial region in the celestial sphere that was scanned multiple times as part of the Sloan Digital Sky Survey (SDSS) supernovae search [Frieman et al. 2008], leading to a 5-band co-add of selected images about two magnitudes deeper than the main SDSS survey [Annis et al. 2014]. Stripe 82 has become a well studied ~ 100 sq-deg scale region, with extensive spectroscopy from SDSS and other wide-field spectroscopic surveys [Croom et al. 2001, Colless et al. 2001, Croom et al. 2004, Jones et al. 2009, Croom et al. 2009a, Croom et al. 2009b, Drinkwater et al. 2010, Eisenstein et al. 2011], reaching fainter magnitudes in smaller regions [Garilli et al. 2008, Coil et al. 2011, Newman et al. 2013, de la Torre et al. 2013, Le Fèvre et al. 2013], and a large spectral coverage from several synergistic surveys [see, e.g. LaMassa et al. 2016, Timlin et al. 2016, Geach et al. 2017, and references therein], including NIR photometry from UKIRT Infrared Deep Survey [UKIDSS, Lawrence et al. 2007] and from a combination of CFHT WIRCam and Visible and Infrared Survey Telescope for Astronomy (VISTA) VIRCAM (VISTA InfraRed CAMERA) data [Geach et al. 2017]. It serves as a precursor of future datasets, and is being covered by ongoing surveys at higher depths (e.g. DES, HSC¹) and denser wavelength coverage (S-PLUS²; Mendes de Oliveira et al. 2018).

In this section we will describe the SDSS and the *CFHT Stripe 82 Survey* (CS82), which provided the data used for the measurements of weak lensing masses. For completeness, we also describe the *Dark Energy Survey* (DES) and the *SOAR Gravitational Survey* (SOGRAS), in which I have been involved in some strong lensing studies during the PhD.

¹<http://hsc.mtk.nao.ac.jp/ssp/>

²<https://confluence.astro.ufsc.br:8443/>

3.1 Sloan Digital Sky Survey

SDSS [Abazajian et al. 2003, Albareti et al. 2017] is a spectroscopic and optical imaging project that makes observations with a dedicated 2.5 meter aperture telescope located at the Apache Point Observatory, New Mexico (USA). The project has already obtained the spectrum of about 2,400,000 galaxies and 480,000 quasars³. Optical imaging has already been finalized, but the spectroscopy continues in the project called SDSS-IV, enhancing the number of galaxy and quasar spectra in the survey.

Thanks to the 2004-2007 seasons for the supernovae search in Stripe 82 (with $-50 < RA < 59$; $-1.25 < DEC < 1.25$), the final co-add data in the *ugriz* bands attained a limiting magnitude of about $r \sim 23.5$ for galaxies. These co-add images were processed with the SDSS pipeline to generate catalogs with basic information (positions, magnitudes, etc.), among other products that were made publicly available in Data Releases (DR). In this work, we use two catalogs from SDSS: i) a cluster catalog resulting from the Voronoi Tessellation algorithm [Soares-Santos et al. 2011] applied to the SDSS stripe 82 co-add catalog [Annis et al. 2014] with neural network photometric redshift measurements [Reis et al. 2012]; ii) a catalog of galaxy clusters identified by the redMaPPer algorithm [Rykoff et al. 2014] on the SDSS 8th Data Release [DR8; Aihara et al. 2011]. The mass measurements of the clusters identified in these datasets are described in the paper presenting the results of this thesis [Pereira et al. 2018b].

3.2 CFHT Stripe 82 Survey

CS82 is a collaboration involving researchers from several countries, which used French, Canadian and Brazilian time on the Canada-France-Hawaii Telescope (CFHT) — a 3.6 meter aperture (optical and infrared) telescope located on Mount Mauna Kea, Hawaii — to image ≈ 170 square degrees ($-42.5 < RA < 45$ and $-1 < DEC < +1$) in the Stripe 82 [Kneib et al. 2010, Erben et al. 2018]. Motivated by the high availability of data at different wavelengths in that region, our group and the collaborators designed CS82 to be the weak lensing survey on Stripe 82, profiting from the excellent image quality provided by the CFHT telescope. The region was imaged in the *i* band, providing data with a depth up to $i = 23.5$ with excellent seeing conditions (average value of $0.6''$). The CS82 survey also motivated a new survey in the infrared, VICS82, which will be described in section 3.5.

³<http://www.sdss.org/dr13/scope/>

After the observations, the collaborators reduced the data (combination of the images and elimination of the instrument’s signature), and also performed the astrometric and photometric calibrations of the 177 images (1 square degree each). After this initial treatment of the images, our group at CBPF was responsible for generating the catalogs with the detections of the objects and their basic information such as positions, magnitudes, radius, etc. I contributed to the generation of these catalogs performing tests to obtain the optimized parameters for detection. The detection catalogs are key to all analyses in CS82 and were first used in [Comparat et al. \[2013\]](#). Subsequently, our group obtained the morphological information of these objects by modeling the Point Spread Function (PSF) of the images and fitting brightness profiles to the objects, as will be described below. I have also carried out several tests to optimize the generation of these morphology catalogs. Due to my contributions to the survey I was considered part of the *core team* of the project and could participate in several papers, such as [[Liu et al. 2015](#), [Li et al. 2016](#), [Charbonnier et al. 2017](#), [Leauthaud et al. 2017](#), [Niemiec et al. 2017](#), [Shan et al. 2017](#)] and the submitted papers [[Soo et al. 2018](#), [Wang et al. 2018](#)]. In particular, the methodology in [Leauthaud et al. \[2017\]](#), [Niemiec et al. \[2017\]](#), and [Shan et al. \[2017\]](#) is closely related to the one described in this thesis.

The brightness profile-fitting is a method applied to the images of galaxies to obtain robust measurements of their shapes. For this sake, common analytic profiles for the galaxies (e.g. de Vaucouleur, Sérsic) are used, convolved with a model for the anisotropic blurring caused by the atmosphere and by the telescope optics (i.e. the PSF), which is obtained from the images of the stars in the field. In CS82 we use this technique, by combining the SExtractor and PSFEx codes to obtain the morphology of the objects. I performed optimization tests for the SExtractor+PSFEx morphology runs, similar to the ones I performed for the detection runs, and I have validated the morphological parameters (e.g. ellipticity) that we measured (see details in my Master’s work [[Pereira 2012](#)]). The derived morphological catalogs are described in a paper in preparation by [Moraes et al. \[2018\]](#). Applications of these catalogs are described in the published paper by [Charbonnier et al. \[2017\]](#), which uses the morphological parameters in a study of compact quiescent galaxies, and the submitted paper by [Soo et al. \[2018\]](#), which uses the morphological information to derive or improve photometric redshifts estimates.

Finally, the detections that we obtained were used as a basis for the shape measurements and the photometric redshifts from matched SDSS co-add [[Annis et al. 2014](#)] and UKIDSS YJHK [[Lawrence et al. 2007](#)] photometry. The catalog containing shapes and photometric redshifts was used in all weak lensing measurements in this work. The details of these measurements are described in Chapter 4, which is also part of the paper [Pereira et al. \[2018b\]](#).

The CS82 survey defines the sky footprint for our analyses and all cluster catalogs in this work are matched to it. The CS82 photo-zs were computed by [Bundy et al. \[2015\]](#) with the BPZ code [[Benítez 2000](#)]. These are more precise than previously available photo-z measurements [see also [Leauthaud et al. 2017, Soo et al. 2018](#)] and therefore we use them throughout this analysis, namely, in the computation of membership probabilities, for determining absolute magnitudes, and in the stacked weak lensing analysis.

3.3 SOAR GRavitational Arc Survey

The SOAR GRavitational Arc Survey (SOGRAS) project observed 47 massive clusters, most of them in Stripe 82, to search for strong lensing features. The observations were made in the $g'r'i'$ bands of the 4.2m SOAR telescope located at Cerro Pachón (Chile). The clusters were observed at two redshift intervals ($z \simeq 0.3$ and $z \simeq 0.5$) with a required seeing of $\leq 0.8''$. Four clusters in this sample that have very good arc candidates were followed-up for deeper imaging and multi-object spectroscopy with the Gemini South Telescope, aiming to determine their dynamical masses and to improve the shape measurements for deriving weak lensing masses (see Chapter 4). I also participated in the selection of these clusters contributing to the description of the survey in the paper [Furlanetto et al. \[2013\]](#). In Chapter 4, I describe the mass measurements for these systems obtained from their weak lensing measurements, which will contribute to a paper currently in development [[Pereira et al. 2018a](#)].

3.4 Dark Energy Survey

DES is an optical imaging survey that will observe, in 5 years, 5000 square degrees of the celestial southern hemisphere with a 570 megapixels camera with red-sensitive CCDs (DECam) installed on the 4m Blanco Telescope, located at the Cerro Tololo Inter-American Observatory (CTIO) in Chile. DES uses the $grizY$ bands to obtain photometric redshifts and will reach limiting magnitudes of $i \sim 24$ when finalized.

The observations are carried out during roughly one semester per year, and the first season took place in 2012-2013, a period called Science Verification (SV). The SV data covered 250 square degrees reaching almost the depth of the complete survey. For this dataset, a thorough search for strong gravitational lensing systems was carried out, involving several selection criteria and including the

visual inspection of the images. Our group had an active participation in this search, which identified 53 candidate systems, 6 of which were later confirmed by spectroscopic observations. A paper describing the spectroscopic confirmation and characterization of these systems has recently been published [Nord et al. 2016] (see Appendix B). Many data products from SV are publicly available at <http://des.ncsa.illinois.edu>.

Recently, the first results using data from a full operating season of DES, the so-called year 1 (Y1) data set, were made public⁴. The Y1 data covers 1500 sq.-deg at 40% of the final depth of the survey. The data from the third season, Y3 (covering 5000 sq.-deg at 50% of the depth), has already been processed, but the catalogs are still being vetted. The data taking for Y5 has already been completed.

3.5 VISTA-CFHT Stripe 82 Survey

The CFHT and the VISTA telescopes have instruments that allow the imaging of large areas of the sky in the near-infrared. The CFHT has the WIRCam mounted in its primary focus, while the VISTA (4m telescope located at the Cerro Paranal Observatory in Chile) is equipped with VIRCAM. The potential of these two instruments was combined to image in the near-infrared the same region of Stripe 82 observed by CS82 forming the so-called “VISTA-CFHT Stripe 82 Survey” (VICS82). VICS82 is a collaborative project between researchers from Taiwan, Canada, France and Brazil which observed 150 square degrees in the Stripe 82 [Geach et al. 2017].

The imaging was performed on the J and K_s bands and a moderate depth of $K_s \sim 22$ and average seeing of $0.7'' - 0.8''$ was obtained. The main scientific objectives of VICS82 are the study of high redshift clusters, stellar masses, quasars and gravitational lensing. VICS82 sits in a relatively unexplored region of the area \times depth diagram for surveys in the same bands, interpolating between the shallow wide-field surveys and the deep “pencil beam” surveys [Geach et al. 2017]. VICS82 is also useful to develop/test tools that can be applied in large surveys in the future.

I have performed initial analyses in the VICS82 detection catalogs and images, optimizing the detection catalogs, computing limiting magnitudes, and identifies features in the image. In this

⁴ And are available at <https://www.darkenergysurvey.org/news-and-results/publications/>

preliminary analysis I have tested and created masks for the images with the *automask*⁵ code [Dietrich et al. 2007, Erben et al. 2009]. These masks are necessary to define reliable objects for many applications.

⁵https://marvinweb.astro.uni-bonn.de/data_products/THELIWWW/automask.html

Chapter 4

WL Analysis and Mass Calibration

In this chapter we present the weak lensing measurements for CS82 data using the redMaPPer and VT cluster catalogs. In section 4.1 we present the lens and source catalogs and how the weak lensing signal is measured in practice, from shapes to shear, and how we use the stacking technique to measure the average tangential density profiles. In the section 4.2 we present the modeling of these density profiles by the NFW model in order to obtain the cluster mass estimates. In the section 4.3 we present the mass-observable scaling relations for the two cluster samples. This chapter is totally based on the submitted paper [Pereira et al. \[2018b\]](#).

4.1 Measuring the tangential shear profile

In order to get the tangential density profiles, we first need to obtain a catalog with the ellipticity of the background sources and a catalog with the lenses. Then, when measuring the density profiles, we perform a *stacking* technique, which consists of grouping the lenses with similar properties to increase the signal-to-noise ratio of the lensing. Each cluster sample is separated by redshift and mass proxy (i.e. richness or μ_*) intervals. In the next sections we detail each of these steps and the results obtained.

4.1.1 Voronoi Tessellation lens catalog

When getting the image of a large area of the sky, in practice, what we have are objects (stars, galaxies) distributed in a plane. In this context, an intuitive way to identify clusters is to search for

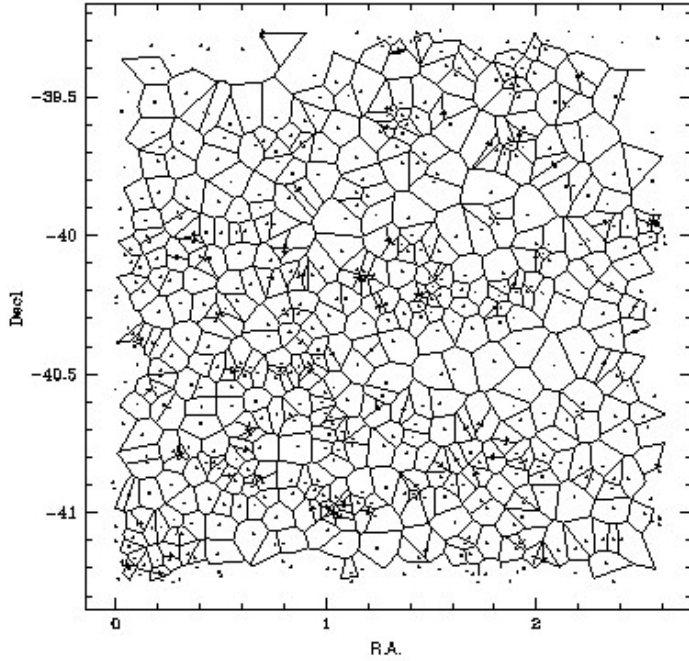


FIGURE 4.1: Example of a Voronoi Tessellation constructed for a galaxy distribution. Credits: [Ramella et al. \[1999\]](#).

regions with a high density of objects (in our case, galaxies), i.e. look for a large concentration of points in the image. A technique that was developed a long time ago (since the 17th century with Descartes and with a modern algorithm implementation in the 80's by [Fortune 1986](#)) and that can be used to identify a concentration of points in a plane is the Voronoi Tessellation [[van de Weygaert and Icke 1989](#), [Ramella et al. 1999](#)]. An implementation of this method – VT cluster finder – was performed by [Soares-Santos et al. \[2011\]](#) in SDSS co-add data.

The VT cluster finder uses a geometric technique to construct the Voronoi cells that contain only one object each. The cell sizes are inversely proportional to the local density and a galaxy cluster candidate is defined as a high-density region composed of small adjacent cells (see Figure 4.1). The raw number of member galaxies, N_{VT} , is thus the number of VT cells. The key point is to estimate the density threshold to separate an overdensity (a galaxy cluster) from the background and take into account the projection effects due to the fact that the Voronoi cells are computed in a 2D-distribution of objects in the sky. In order to achieve that, the VT algorithm is built in photo-z shells and uses the two-point correlation function of the galaxies in the field to determine the density threshold for detection of the cluster candidates and their significance. Since it is a geometric technique, there is no need of *a priori* assumption on galaxy colors, the presence of a red-sequence or any assumptions about their astrophysical properties.

In this thesis we use the VT catalog produced for the SDSS Stripe 82 co-add [[Wiesner et al. 2015](#)].

Since that release version (v1.10) the VT team has developed an improved membership assignment scheme and a new mass proxy, μ_* . In this work we incorporate those developments (see section 4.1.1.1 for details) and add two new improvements, namely, a defragmentation algorithm and a redefinition of the cluster central galaxy (described in sections 4.1.1.2 and 4.1.1.3, respectively). The former mitigates the effect of photometric redshift shell edges and of multiple density peaks within individual clusters. The latter allows us to extend the probabilistic approach of membership to the determination of the central cluster galaxy.

4.1.1.1 Assigning the new mass proxy μ_*

N_{VT} performs poorly as a mass proxy, as shown by the scatter in the richness-mass relation presented in Saro et al. [2015]. The new mass proxy, μ_* , is based on a probabilistic membership assignment scheme [Welch et al. 2018]¹ and on measurements of stellar masses [Palmese et al. 2018]². In particular, Palmese et al. [2018] showed that the scatter in the μ_* to X-ray temperature relation is comparable to that of other mass proxies for an X-ray selected sample, and that it allows interesting cluster evolution analyses, having a clear physics meaning of the cluster stellar mass.

The first step in computing μ_* is to compute the membership probability P_{mem} for each cluster galaxy

$$P_{\text{mem}} = P_z \cdot P_r \cdot P_c, \quad (4.1)$$

where the three components represent the probability of the galaxy being a member given its redshift (P_z), its distance from the cluster center (P_r) and its color (P_c):

- P_z is the integrated redshift probability distribution of each galaxy within a $\Delta z = 0.1$ window of the cluster.
- P_r is computed assuming a projected Navarro-Frenk-and-White profile.
- P_c is determined via Gaussian mixture modeling of the galaxy color distribution with two components, red sequence and blue cloud; it is defined as the sum of the probability that the galaxy color is drawn from either the blue or red component.

For membership assignment purposes we use a subsample of the galaxy catalog cut at $M_r < -19$. That subsample is volume limited over our redshift range. We calculated the absolute magnitudes

¹<https://github.com/bwelch94/Memb-assign>, commit 1d6eabd

²<https://github.com/apalmese/BMAStellarMasses>, commit 487c650

using kcorrect v4_2 [Blanton and Roweis 2007] taking the BPZ photo-z as the galaxy redshift. We constructed a grid of $g - r$, $r - i$, and $i - z$ colors from the templates in kcorrect and chose the closest to the observed galaxy colors. That chosen template provides the K-correction from observed i band to rest-frame r -band, which, together with our chosen cosmology, allows us to calculate M_r .

After computing the membership probabilities for each galaxy i within 3 Mpc of each cluster j , we compute their stellar masses assuming that every member galaxy is at the redshift of its host, $M_{\star,i}(z_j)$. Because the cluster redshifts have smaller uncertainties than individual galaxies, this minimizes the uncertainties on $M_{\star,i}$ measurements. Finally, once the stellar masses are computed, we define the new mass proxy as the sum of the individual galaxy stellar masses weighted by their membership probability

$$\mu_{\star} = \sum_i P_{\text{mem},i} M_{\star,i}. \quad (4.2)$$

The membership assignment and μ_{\star} computation methods were applied only to VT clusters with $N_{\text{VT}} > 20$, to avoid poorly detected galaxy groups. After applying the CS82 mask and a photometric redshift cut at $z < 0.6$, where the VT sample is most reliable, we obtain a sample of 136 clusters, which are used throughout this analysis.

4.1.1.2 Investigating cluster fragmentation

Fragmentation of large clusters into smaller components in the VT catalog is one of the sources of scatter in the observable-mass relation. We uncovered the issue by performing cylindrical matching (angular separation $\theta < 1$ arcmin and $\Delta z < 0.05$) between redMaPPer and VT catalogs. This comparison showed some cases where one redMaPPer cluster was split into two or more VT clusters.

When applied to a cluster fragment, the new probabilistic membership method will result in a full fledged list of members, as the probabilities are computed out to 3 Mpc radius. This is a designed feature. For two fragments located near each other, the result will be two instances of the same cluster with slightly different membership probabilities. In that case, only one instance should be maintained in the catalog. In order to ensure that, we developed a defragmentation method using the membership probabilities P_{mem} . For a given pair of cluster candidates we define the “true” cluster as the one for which $\sum P_{\text{mem}}$ is the largest.

In practice we first attribute a flag for each cluster in the catalog as if they were all unique real clusters (`cluster_frag=1`). Then, we rank them by mass proxy and compute the angular separation

between each other. If the separation is smaller than the largest R_{200} between the two and the redshift difference is $\Delta z < 0.05$, those clusters are considered to be two instances, i and j , of a fragmented pair. We compute the summation of the member probabilities of the fragmented clusters i and j as $P_i = \sum P_{\text{mem}}^i$ and $P_j = \sum P_{\text{mem}}^j$, respectively. We then match their members list (in our membership scheme, clusters may share members) and then compute the quantity $P_{\text{match}} = \sum P_{\text{mem}}^{i,\text{match}} = \sum P_{\text{mem}}^{j,\text{match}}$ for the matched members. Once we have these quantities we compute the fractions

$$f_{ij} = \frac{P_{\text{match}}}{P_i} \quad \text{and} \quad f_{ji} = \frac{P_{\text{match}}}{P_j}. \quad (4.3)$$

Since P_{match} is the same for both, the only difference is in the denominator. If $f_{ij} \leq f_{ji}$, then i is kept in the catalog while j is removed (i.e. set `cluster_frag=0`). We apply this procedure to VT clusters in the range $0.1 \leq z < 0.6$ and we find that ~ 16 per cent of the clusters were affected by this issue. This is therefore a non-negligible correction and future versions of VT catalog should have this new procedure applied to them before being released.

4.1.1.3 Redefining the cluster central galaxy

The brightest cluster galaxy (BCG) is a good proxy for the center of the cluster and that fact is used in several cluster finding methods [Koester et al. 2007, Hao et al. 2010, Oguri 2014]. The original VT algorithm, however, takes a purely spatial approach and defines the cluster central galaxy as the one inside the highest density VT cell. After computing μ_\star we redefine the central cluster galaxy as the member galaxy with maximum probability of membership. The probability P_{cen}^\star that this newly defined central galaxy is the true center of the cluster is proportional to its membership probability

$$P_{\text{cen}}^\star \propto \max(P_{\text{mem}}). \quad (4.4)$$

Although not normalized, this centering probability is analogous to that of the redMaPPer algorithm.

4.1.2 redMaPPer lens catalog

In recent years, one of the techniques for identifying galaxy clusters (our lenses) that has become standard is that based on the empirical relation between the color and magnitude of the *early-type* (elliptical and lenticular) galaxies known as the *red sequence* [Gladders and Yee 2000].

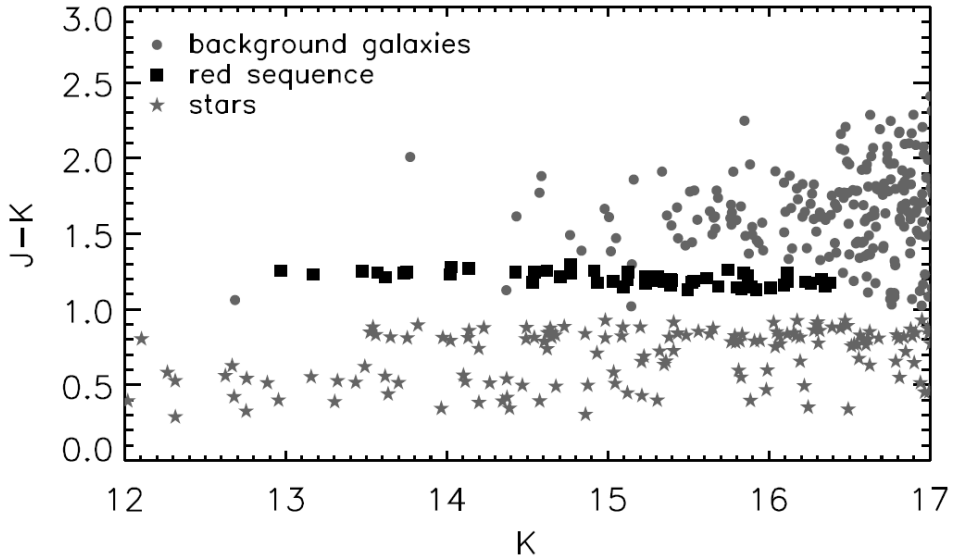


FIGURE 4.2: Red sequence of the Abell 1084 cluster. The color-magnitude diagram was obtained in the infra-red bands. In these bands it is easy to separate the red sequence galaxies (*black squares*) from the stars (*grey stars*) and regular galaxies (*grey circles*) in the field. Credits: [Stott et al. \[2009\]](#).

In the most massive clusters the population of galaxies more common are the early-type ones, that are the oldest galaxies and do not present regions of stellar formation, being thus the reddish objects in the galaxy clusters.

As previously mentioned, a linear relationship between the color and magnitude of the early-type galaxies of a cluster (in a given redshift) was empirically found, where the brightest galaxies are the most reddish (see Figure 4.2) – and that is why for the set of galaxies that obey this relation we named “red sequence”.

The linear relationship for color-magnitude was observed in several clusters with different characteristics and has been shown to be a “universal” relation and valid with a good level of reliability up to $z \sim 1.3$. Therefore, identifying red sequences in regions of the sky is a direct way of finding overdensity regions, i.e, it is a robust way of finding clusters of galaxies (lenses).

Several codes based on this technique have now been developed and widely used in large surveys, such as the redMaPPer [[Rykoff et al. 2014, 2016](#)] and maxBCG [[Koester et al. 2007](#)] codes. In this work, besides the VT algorithm, we use galaxy clusters identified with redMaPPer.

The redMaPPer cluster finder uses multi-band colors to find overdensities of red-sequence galaxies around candidate central galaxies. In SDSS data, redMaPPer uses the five band magnitudes ($ugriz$) and their errors to spatially group the red-sequence galaxies at similar redshifts into cluster candidates. For each red galaxy, redMaPPer estimates its membership probability (p_{mem}) following a

matched-filter technique. At the end, for each identified cluster, redMaPPer will return an optical richness estimate λ (the total sum of the p_{mem} of all galaxies that belong to that cluster), a photo-z estimate z_λ , and the positions and probabilities of the five most likely central galaxies (P_{cen}).

In this work we use the most recent version (v6.3) of the SDSS redMaPPer public catalog [Rykoff et al. 2016], which covers an area of 10^4 deg^2 , down to a limiting magnitude of $i = 21$ for galaxies. The full sample of redMaPPer clusters in the catalog has $0.08 \lesssim z_\lambda < 0.6$ and $20 \lesssim \lambda < 300$. After restricting the catalog to the $\sim 170 \text{ deg}^2$ of the CS82 footprint, we restrict our mass measurements to the low redshift bin $0.1 \leq z_\lambda < 0.33$ to enable comparison with previous SDSS weak lensing measurements and because the redMaPPer cluster catalog from single epoch SDSS data is most reliable at these redshifts. The redMaPPer sample used in this work, after all selection criteria are applied, contains 230 clusters.

We compute μ_* as well for the redMaPPer clusters, employing the same steps described in section 4.1.1.1. This means that new membership probabilities are computed for every cluster and enables direct comparison between the $\Delta\Sigma$ profiles obtained for λ and μ_* , as discussed in section 4.1.4. The defragmentation step was not needed for redMaPPer.

4.1.3 Source catalog with Lensfit

One of the most important steps in measuring the weak lensing signal is the measurement of the background galaxy (sources) ellipticities. In this step, it is necessary to overcome the difficulty of measuring the shapes of very faint galaxies that suffer from observational and optical effects such as PSF, noise, etc. As we mentioned, PSF is due to variations in both the atmosphere and the optics of the telescope and can result in isotropic and anisotropic blurs in the shape of the sources, thereby diluting the shear signal produced by the gravitational effect. Therefore, it is necessary to correct this effect to avoid bias in determining the shape of the sources.

Many methods and their code implementations have been developed to accurately measure the shapes (ellipticities) of the galaxies, e.g. *Imcat/KSB* [Kaiser et al. 1995], *Shapelets* [Kuijken 2006] and the *Lensfit* [Miller et al. 2007, Kitching et al. 2008]. In the *Shapelets* method a Gauss-Hermite (Gaussian multiplied by polynomials) base is created in order to reconstruct models for the PSF, noise and the form of observed galaxies. The advantage of this method is the possibility of using several models for the PSF, unlike the methods based on the profile fitting, which assume an arbitrary model for the PSF, in general. These methods were used by initiatives such as the GRAVitational Enlightenment

Accuracy Testing [Bridle et al. 2009, Mandelbaum et al. 2014] and The Shear TEsting Program [Heymans et al. 2006], which aimed to test the codes used to obtain the shear measurements of the sources in simulations and real data. Lensfit was one of the codes that presented a higher value for the figure of merit Q (see Bridle et al. 2010 for details), which is a quantity in the challenges used to determine the successful method. This quantity represent a method's ability to both filter the noise effectively and remove the significant PSF kernel in the observed galaxy image. Besides the precise recovery of the ellipticities, Lensfit also presented a good computational performance, which makes it suitable for the use in large surveys. Imcat/KSB, despite being a robust code that uses the formalism of the polarizability tensors P^{sr} and P^{sm} [Kaiser et al. 1995, Pereira 2012] for the blurring corrections, it has shown a code with limitations for use in future large surveys.

We use the shape measurements from CS82 survey, which has a limiting magnitude of 24 and mean seeing of 0.6 arcsec [Leauthaud et al. 2017] providing excellent imagining quality for precise shape measurements. The shape estimates were obtained with Lensfit code that performs a Bayesian profile-fitting of the surface brightness to obtain an unbiased estimate of the the shear components from the average ellipticities. The code was tested in simulations and real data [Kitching et al. 2008, Miller et al. 2013], achieving very good results [Kitching et al. 2012] and became a suitable tool for precise shape estimates in surveys with the imagining quality of CS82.

Lensfit was applied to the masked imaging data following the same pipeline as the CFTHLenS collaboration [Miller et al. 2013] and applying the shear calibration factors and testing the systematics in the same way as Heymans et al. [2012]. For each source an additive calibration correction factor c_2 is applied to the ϵ_2 shear component and a multiplicative shear calibration factor as a function of the signal-to-noise ratio and size of the source, $m(\nu_{SN}, r)$, is also computed. Besides that, the Lensfit shear measurements were also compared with other independent shear calibration methods [Reyes et al. 2012, Melchior et al. 2014, Clampitt and Jain 2015] by Leauthaud et al. [2017] who have found that a large unknown and unaccounted for bias in the Lensfit measurements is an unlikely possibility. From the Lensfit output catalog we select the objects with weight $w > 0$, FITCLASS = 0 and MASK ≤ 1 . These quantities are computed by Lensfit, where w is an inverse variance weight for each source, FITCLASS is a star/galaxy separation flag to remove stars and select galaxies with well measured shapes and MASK is a flag that indicates the quality of the photometry, where for most of the weak lensing analysis MASK ≤ 1 is a robust cut to apply, as shown by Erben et al. [2013]. We also select only galaxies with magnitudes $20 \leq i' \leq 24.7$.

The BPZ photometric redshift catalog includes, in addition to the photo-zs and errors, the parameter

BPZ_ODDS that varies between 0 to 1 and indicates catastrophic redshift errors. We removed from our source galaxy sample all objects with $\text{BPZ_ODDS} \leq 0.5$. According to [Hildebrandt et al. \[2012\]](#) and [Benjamin et al. \[2013\]](#) the photo-z of the sources degrade at $z_s > 1.3$, which could be a concern for our measurements. However, [Leauthaud et al. \[2017\]](#) performed a test computing the CS82 lensing signal with and without this redshift cut and have shown no statistically significant shift in the signal. Therefore we do not apply any restriction on the maximum value of z_s so as to maximize the number of background sources. Finally, after applying all the aforementioned cuts we obtained a final catalog with 2 809 764 sources, which give an effective weighted galaxy number density of $n_{\text{eff}} = 4.5$ galaxies arcmin $^{-2}$.

4.1.4 Density profile measurements

In this section we present how we measure the stacked lensing signal of redMaPPer and VT clusters using the CS82 shear catalog. For the stacking of the lenses we define bins of redshift and observable mass proxy.

In Figure 4.3 we show the redshift distributions for redMaPPer and VT clusters used in our stacked measurements highlighting the boundaries of the low and high z bins. For the low redshift bin we follow [Simet et al. \[2017\]](#) (hereafter S17), and define $0.1 \leq z_{\text{low}} < 0.33$. We have 230 redMaPPer clusters at those redshifts, with $20 \leq \lambda \leq 128.7$. The corresponding range of μ_* for these clusters is $3.82 \times 10^{12} M_\odot \leq \mu_* \leq 13.85 \times 10^{12} M_\odot$. For the VT sample we have 41 clusters in the low-redshift bin. We also consider a higher redshift bin, $0.33 \leq z_{\text{high}} \leq 0.6$, for which there are 95 clusters in the catalog. The VT clusters in these two redshift bins lie within the range $1.47 \times 10^{12} M_\odot \leq \mu_* \leq 16.53 \times 10^{12} M_\odot$.

Inside each redshift bin we separate the samples into four mass proxy bins, in such a way that we have a similar number of clusters in each bin. For the redMaPPer catalog we repeat this procedure twice, once for λ and once for μ_* (see Table 4.1). The stacking in λ allows us to compare our mass-richness results with S17 and other measurements reported in the literature. The binning in μ_* will enable us to compute the first mass-calibration of redMaPPer cluster using this new mass proxy. Table 4.2 shows the z and μ_* bins for the VT catalog.

As described in Section 2.3.3, from Equation (2.32) we can compute the surface density contrast $\Delta\Sigma$ over several lenses with similar physical properties to increase the lensing signal and reduce the

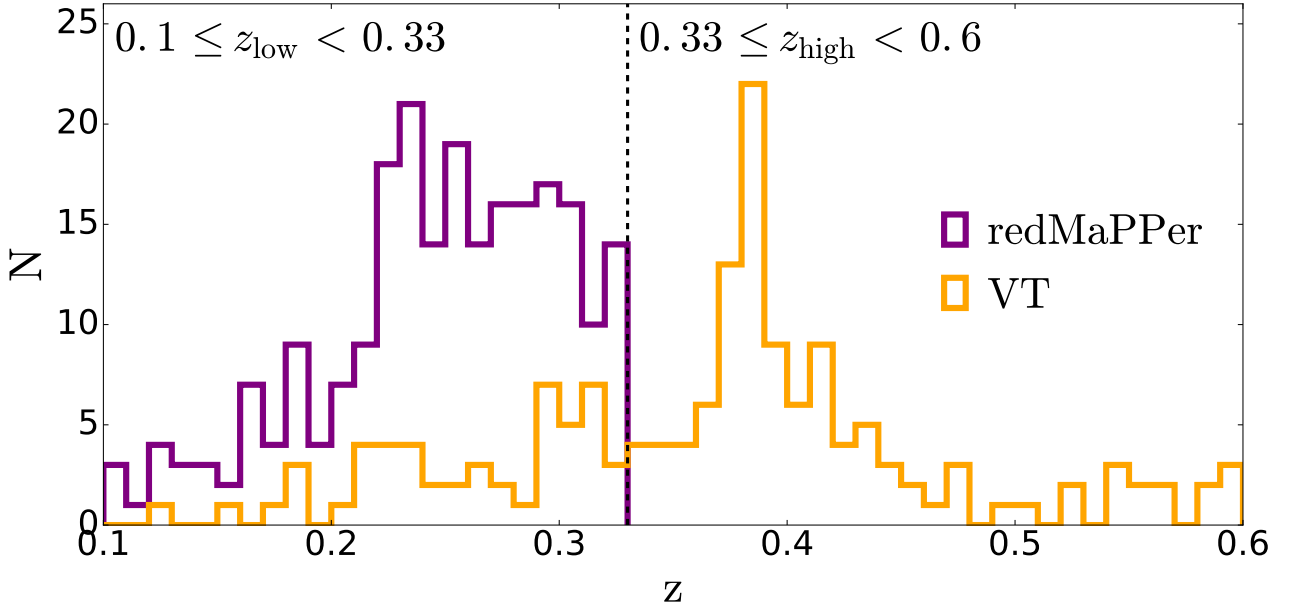


FIGURE 4.3: Redshift distributions of the redMaPPer (purple) and VT (orange) clusters used in our analysis. For our measurements we selected the redMaPPer sample in a low redshift bin ($0.1 \leq z_{\text{low}} < 0.33$) and the VT sample in two redshift bins ($0.1 \leq z_{\text{low}} < 0.33$ and $0.33 \leq z_{\text{high}} < 0.6$).

Credits: [Pereira et al. \[2018b\]](#)

Mean z	λ range	Mean λ	No. of clusters
0.249	[20, 23.42)	21.72	59
0.244	[23.42, 28.3)	25.64	59
0.247	[28.3, 39.7)	32.90	59
0.249	[39.7, 145)	58.06	53
Mean z	μ_* range	Mean μ_*	No. of clusters
0.228	[0, 4.15)	3.40	59
0.252	[4.15, 5.20)	4.72	59
0.251	[5.20, 6.84)	5.97	59
0.259	[6.84, 14)	8.41	53

TABLE 4.1: Binning scheme and properties of the redMaPPer cluster sample. We use the same low redshift bin as S17, but for the binning in λ we use a different scheme where we have a similar number of clusters in each of the four richness bins. Here μ_* is given in units of $10^{12} M_\odot$.

z range	Mean z	μ_* range	Mean μ_*	No. of clusters
$[0.1, 0.33)$	0.220	[0, 5.78)	4.42	11
	0.279	[5.78, 7.59)	6.84	11
	0.278	[7.59, 10.55)	8.60	10
	0.290	[10.55, 17)	11.45	9
$[0.33, 0.6)$	0.457	[0, 5.38)	4.17	28
	0.428	[5.38, 6.58)	5.94	24
	0.410	[6.58, 8.90)	7.57	24
	0.380	[8.90, 17)	11.03	19

TABLE 4.2: Binning scheme and properties of the VT cluster sample. We separate in two redshift bins and choose the μ_* bins so as to have a similar number of clusters in each of the four bins. Here μ_* is in units of $10^{12} M_\odot$.

effect of substructures, uncorrelated structures in the line of sight, shape noise and shape variations of individual halos.

In practice we use the inverse variance weight w from Lensfit to optimally weight shear measurements, accounting for shape measurement error and intrinsic scatter in galaxy ellipticity. Then, for a given lens i and a given source j , the inverse variance weight for $\Delta\Sigma$ is derived for Equation (2.32) and expressed as $w_{ls,ij} = w_j \Sigma_{\text{crit},ij}^{-2}$. The quantity w_{ls} is used to compute $\Delta\Sigma$ through a weighted sum over all lens-source pairs

$$\Delta\Sigma = \frac{\sum_{i=1}^{N_l} \sum_{j=1}^{N_s} w_{ls,ij} \times \gamma_{t,ij} \times \Sigma_{\text{crit},ij}}{\sum_{i=1}^{N_l} \sum_{j=1}^{N_s} w_{ls,ij}}, \quad (4.5)$$

where N_l is the number of cluster lens and N_s is the number of source galaxies.

We compute $\Delta\Sigma$ in 20 logarithmically spaced radial bins from $R \sim 0.1 h^{-1}$ Mpc to $R \sim 10 h^{-1}$ Mpc. In Miller et al. [2013] it was pointed out that a multiplicative correction for the noise bias needs to be applied after stacking the shear. This correction can be computed from the multiplicative shear calibration factor $m(\nu_{\text{SN}}, r)$ provided by Lensfit. An often used expression for this correction [Velander et al. 2014, Hudson et al. 2015, Leauthaud et al. 2017, Shan et al. 2017] is given by

$$1 + K(z_l) = \frac{\sum_{i=1}^{N_l} \sum_{j=1}^{N_s} w_{ls,ij} [1 + m(\nu_{\text{SN},ij}, r_{ij})]}{\sum_{i=1}^{N_l} \sum_{j=1}^{N_s} w_{ls,ij}}, \quad (4.6)$$

and the calibrated lensing signal is computed as

$$\langle \Delta\Sigma^{\text{cal}} \rangle = \frac{\Delta\Sigma}{1 + K(z_l)}. \quad (4.7)$$

In order to reduce the dilution of the lensing signal due to uncertainties in the photo-zs that can cause some background sources to be placed as foreground sources and vice-versa, we impose that $z_s > z_l + 0.1$ and $z_s > z_l + \sigma_{95}/2$ where z_l is the lens redshift, z_s is the source redshift and σ_{95} is the 95 per cent confidence limit on the source redshift provided by BPZ. These cuts were validated by Leauthaud et al. [2017], who have found that the lensing signal is invariant over a range of lens-source separation cuts, suggesting that dilution caused by foreground or physically associated galaxies is not a large concern for CS82 weak lensing measurements (see their Appendix A1 for more details).

We compute the weak lensing signal $\Delta\Sigma$ from Equation (4.7) in 20 logarithmic bins in the range $(0.1 - 10)h^{-1}$ Mpc. As the errors on the weak-lensing signals are expected to be dominated by shape noise, we do not expect a noticeable covariance between adjacent radial bins and we treat them as independent in our analyses. The error bars in our lensing signals are obtained by bootstrapping on

the individual clusters with $N = 100$ resamplings in each stack. Vitorelli et al. [2018] have tested several bootstrap resampling values (e.g. $N = 50, 150, 200, 300$) and found no significant variation of the error bars down to $R \lesssim 4$ Mpc.

We computed the cross component of the lensing signal ($\Delta\Sigma_{\times}$) and found no evidence of spurious correlations in the weak-lensing signals, i.e. the $\Delta\Sigma_{\times}$ measurements are consistent with zero.

In Table 4.3 we present a summary of the systematics considered in this work, both for obtaining the weak lensing signal $\Delta\Sigma$ and in the profile-fitting. Previous lensing works showed that the statistical uncertainties dominate the error budget in CS82 [Battaglia et al. 2016, Leauthaud et al. 2017, Shan et al. 2017], then we will assume systematics are sub-dominant in our lensing measurements such that all error bars reported in this work are statistical only.

4.2 Profile-fitting of redMaPPer and VT clusters

To model the average lensing signal around each lens and then obtain their mass estimates we use a model with two components: a perfectly centered dark matter halo profile and a miscentering term where the assumed center does not correspond to the dynamical center of the dark matter halo. For the first term we assume the clusters are well modeled by spherical NFW [Navarro et al. 1996] haloes, on average, in which the 3-dimensional density profile is given by

$$\rho(r) = \frac{\delta_c \rho_{\text{crit}}}{\frac{r}{r_s} \left(1 + \frac{r}{r_s}\right)^2}, \quad (4.8)$$

where r_s is the cluster scale radius, δ_c is the characteristic halo overdensity, $\rho_{\text{crit}} = 3H^2(z)/8\pi G$ is the critical density of the universe at the lens redshift and $H(z)$ is the respective Hubble parameter.

In this work we use as cluster mass the mass M_{200} contained within a radius r_{200} where the mean mass density is 200 times the critical density of the universe. The scale radius is given by $r_s = r_{200}/c_{200}$, where c is the so-called concentration parameter. In our fitting procedure we follow Kettula et al. [2015], van Uitert et al. [2012] and use the concentration-mass ($c(M)$) scaling relation from Duffy et al. [2008] given by

$$c_{200} = 5.71 \times \left(\frac{M_{200}}{2 \times 10^{12} h^{-1}}\right)^{-0.084} \times (1+z)^{-0.47}. \quad (4.9)$$

The mass measurements only have a weak dependence on the adopted $c(M)$ relation, at least within a radius where the profile is measured. Then, we would not expect our choice of $c(M)$ to be relevant in the mass estimation.

[Bartelmann \[1996\]](#), [Wright and Brainerd \[2000\]](#) provide an analytical expression for the projected NFW profile, $\Delta\Sigma_{\text{NFW}}$ and we use a Python implementation³ of these results for our profile-fitting procedure.

The central galaxy of a cluster is usually very bright but is not necessarily the BCG. For instance, [Rykoff et al. \[2016\]](#) pointed out that only $\sim 80 - 85$ per cent of the redMaPPer central galaxies are BCGs and [Zitrin et al. \[2012\]](#) show that some BCGs present an offset from the center of their host dark matter halo. This miscentering affects the observed shear profile [[Yang et al. 2006](#), [Johnston et al. 2007](#), [Ford et al. 2014](#)]. We follow the correction scheme presented in [Johnston et al. 2007](#), [Ford et al. 2015](#), [Simet et al. 2017](#) to account for this effect.

If the 2-dimensional offset in the lens plane is R_s , the azimuthal average of the profile is

$$\Sigma_{\text{misc}}(R) = \int_0^\infty dR_s P(R_s) \Sigma(R|R_s), \quad (4.10)$$

where

$$\Sigma(R|R_s) = \frac{1}{2\pi} \int_0^{2\pi} d\theta \Sigma \left(\sqrt{R^2 + R_s^2 + 2RR_s \cos\theta} \right). \quad (4.11)$$

In other words, the angular integral of the profile $\Sigma(R)$ is shifted by R_s from the center. We also use a probability distribution for R_s given by

$$P(R_s) = \frac{R_s}{\sigma_{\text{off}}^2} \exp \left(-\frac{1}{2} \frac{R_s^2}{\sigma_{\text{off}}^2} \right), \quad (4.12)$$

which is an *ansatz*, assuming the mismatching between the center and R_s follows a 2-dimensional Gaussian distribution. We use the Python implementation⁴ of [Ford and VanderPlas \[2016\]](#) to compute the miscentering term. The width of the miscentering distribution (σ_{off}) is fixed as $0.4h^{-1}$ Mpc for simplicity. As noted in S17, this is an expected value for clusters with mass $\sim 10^{14}M_\odot$.

Our complete theoretical modeling for $\Delta\Sigma$, considering the centered halo and miscentering terms, is given by

$$\Delta\Sigma^{\text{theo}} = p_{\text{cc}} \Delta\Sigma_{\text{NFW}} + (1 - p_{\text{cc}}) \Delta\Sigma_{\text{misc}}. \quad (4.13)$$

³<https://github.com/joergdietrich/NFW>, v0.1

⁴<https://github.com/jesford/cluster-lensing>, v0.1.2

Systematic:	Summary:
Shear measurement	Apply additive calibration correction factor c_2 to ϵ_2 component Apply multiplicative shear calibration $m(\nu_{\text{SN}}, r)$
Photometric redshifts	Remove BPZ.ODDS ≤ 0.5 to reduce systematic errors due to catastrophic outliers Apply $z_s > z_l + 0.1$ and $z_s > z_l + \frac{\sigma_{95}}{2}$
Miscentering	Apply same correction as Yang et al. 2006 , Johnston et al. 2007 , Shan et al. 2017

TABLE 4.3: Summary of the systematics we are take into account in the measurements of the lensing signal and in the profile-fitting. Note that since we apply a radial cut in innermost and outer range, following the same procedure as S17, our measurements are not affected by the central point mass and the 2-halo terms.

In addition to the contribution from single (centered and miscentered) cluster halos, a variety of studies in the literature have pointed out the need to consider other terms to better model the measured profile. These often include a *point mass* term for a possible stellar-mass contribution of the central galaxies and a so-called *2-halo* term due to neighboring halos (i.e., due to the large-scale structure of the Universe). In this work we avoid these two contributions as we are only interested in measuring M_{200} and we do not have enough precision to fit for many free parameters in each mass-proxy bin. For this sake, we perform the model-fitting in a restricted radial range. We follow S17 and use $R_{\min} = 0.3 h^{-1}$ Mpc as the inner radius limit to avoid problems with the selection of background galaxies and the increased scatter due to the low sky area, and also to reduce the effects of the point mass contribution [see also [Mandelbaum et al. 2010](#)]. We define a richness-dependent outer limit in the range $R_{\max} \simeq (2.5 - 3.5) h^{-1}$ Mpc to avoid the 2-halo contribution. S17 show that the results are insensitive to the specific values of R_{\max} for a wide range of values.

Finally, for each sample in the radial range mentioned above, we perform the profile-fitting via Bayesian formalism and Markov Chain Monte-Carlo (MCMC) method to compute the *posterior* distribution $Pr(M_{200}, p_{\text{cc}} | \Delta\Sigma^{\text{obs}})$ and then obtain the best estimate for the cluster mass (see Appendix A for a brief description of Bayesian approach and MCMC). Following [Vitorelli et al. \[2018\]](#), we use the logarithm of a flat prior for the mass in the rage of $10^{12} h^{-1} M_{\odot} < M_{200} < 10^{15} h^{-1} M_{\odot}$ and a Gaussian prior on the miscentering term, $\mathcal{N}(p_{\text{cc}}; \overline{P}_{\text{cen}}, \sigma_{P_{\text{cen}}})$, for $0 < p_{\text{cc}} < 1$, where $\overline{P}_{\text{cen}}$ and $\sigma_{P_{\text{cen}}}$ are the mean and standard deviation of the highest centering probabilities P_{cen} . We use the same modeling approach for P_{cen}^* , in both the redMaPPer and VT catalogs.

After performing the MCMC, a useful way to diagnose the posterior distributions is to look for the “triangle” plots [[Foreman-Mackey 2016](#)]. The triangle plot shows all the one and two dimensional projections of the posterior probability distributions of the parameters. This is useful to visualize all of the covariances between parameters. In Figure 4.4 we present the triangle plots for the z_{low} redMaPPer clusters in bins of λ , but using P_{cen} in the prior for miscetering term (top) and P_{cen}^*

(bottom). Although they reach similar profile-fitting results (as we will see later), it is interesting to see that the use of P_{cen}^* in the miscentering prior seems to better constrain the parameters. In Figure 4.5 we show the same plot, but for z_{low} redMaPPer clusters in μ_* bins and again P_{cen}^* seems to behave better. In Figure 4.6 we show the triangle plot for z_{low} (top) and z_{high} (bottom) VT clusters in μ_* bins and using P_{cen}^* for the prior in the miscentering term. We see that z_{low} parameters were better constrained than parameters of the z_{high} sample.

In Figure 4.7 we show the weak lensing profiles for the redMaPPer clusters. We present the measured signal (*black dots*) and the best fits using P_{cen} in the Gaussian prior for miscentering (*purple solid line*) and using P_{cen}^* in the prior (*orange dotted line*). We also show the centered halo contribution (*purple dashed-dotted line*) and the miscentering term (*purple dotted line*) from Equation (4.13) as computed in the P_{cen} prior case. The dotted vertical lines correspond to R_{max} and R_{min} , which define the range where the fit is performed. We show the low redshift sample in bins of λ (in the top panel) and μ_* (in the bottom).

We see from Figure 4.7 that the best fit results using P_{cen} and P_{cen}^* are very similar, validating the use of P_{cen}^* for the miscentering correction, and in particular its application to the VT clusters. In Figures 4.8 and 4.9 we show the profile-fitting results for the VT clusters in the low and high redshift samples in bins of μ_* . The best-fit values of the two parameters for all cases considered here are presented in Table 4.4.

In our analyses we use M_{200} relative to critical matter density (hereafter M_{200c}) of the Universe, however, to enable the comparison with other works in the literature, it is useful to express the results in terms of M_{200} relative to the mean density (M_{200m}). To convert from M_{200c} to M_{200m} we use the Colossus code⁵ [Diemer 2015]. In Table 4.4 we show the results in terms of both mass definitions.

4.3 Mass-calibration of redMaPPer and VT clusters

From the weak lensing masses in Table 4.4 we obtain a mass calibration for redMaPPer clusters and compare with the current results from literature. We then apply the same methodology to obtain the mass-observable scaling relation for the new mass proxy μ_* , both for the redMaPPer and VT clusters.

⁵<https://bitbucket.org/bdiemer/colossus>

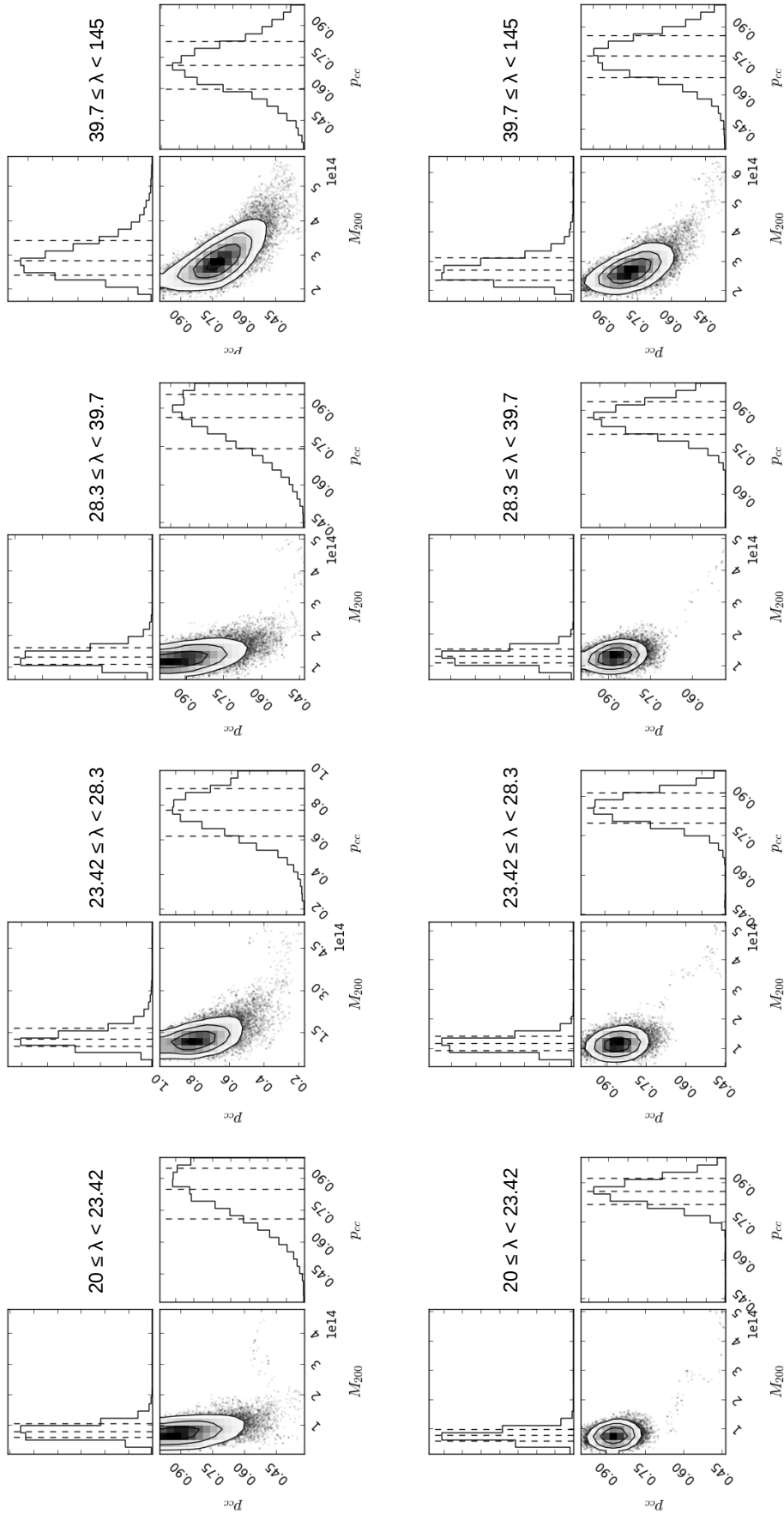


FIGURE 4.4: Triangle plot showing the one and two-dimensional posterior distributions of the parameters (M_{200}, p_{cc}). The concentric contours correspond to the 68%, 95% and 99.7% confidence levels. This plot was generated using the python module corner [Foreman-Mackey 2016]. We show the plots for the profile-fitting of redMaPPer clusters in bins of λ for the z_{low} interval, using P_{cen} (top) and P_{cen}^* (bottom) for the miscentering prior.

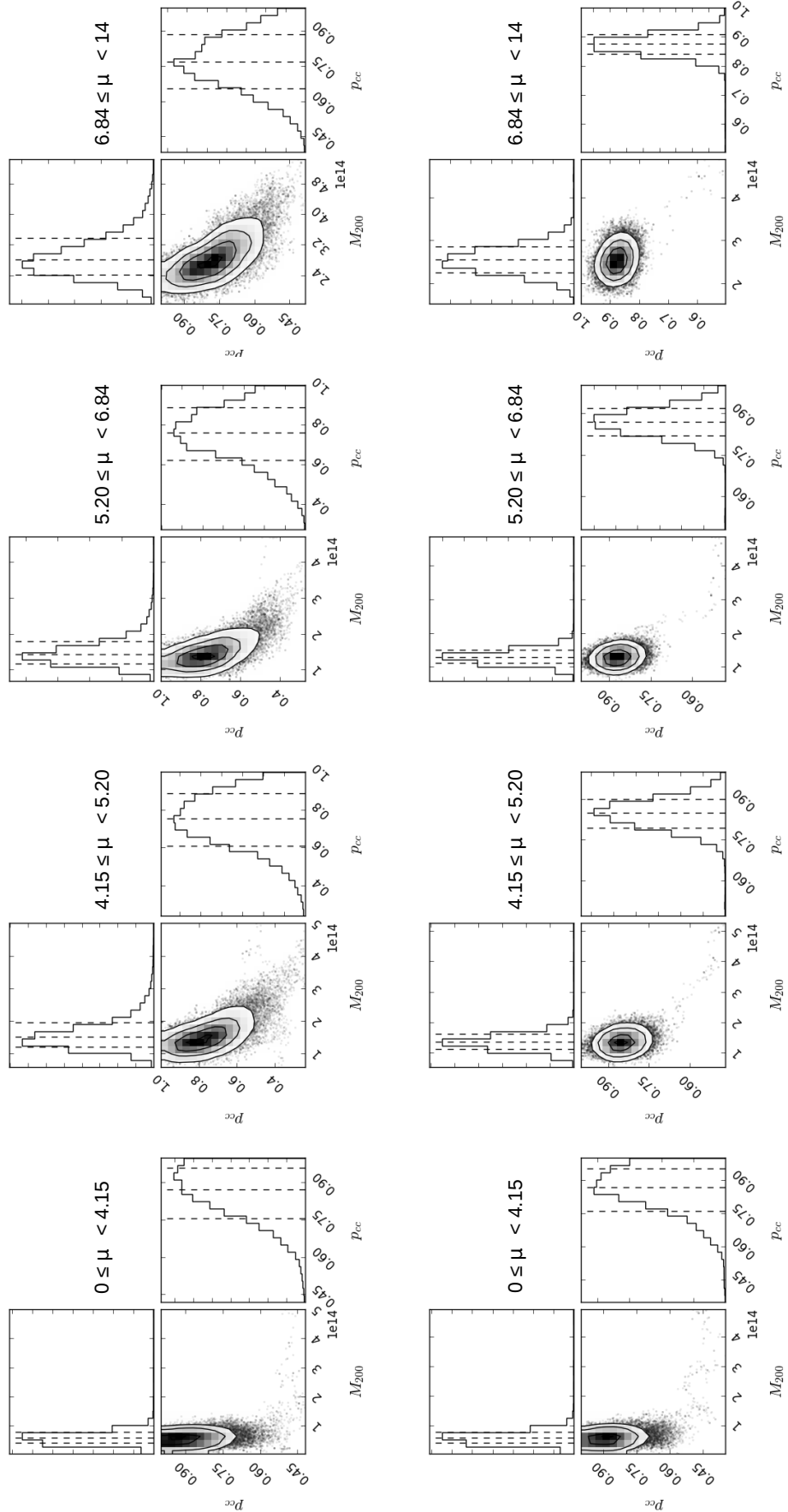


FIGURE 4.5: Triangle plot showing the one and two-dimensional posterior distributions of the parameters (M_{200}, p_{cc}). The concentric contours correspond to the 68%, 95% and 99.7% confidence levels. We show the triangle plots for the profile-fitting of redMaPPer clusters in bins of μ_* for the z_{low} interval, using P_{cen} (top) and P^* (bottom) for the miscentering prior.

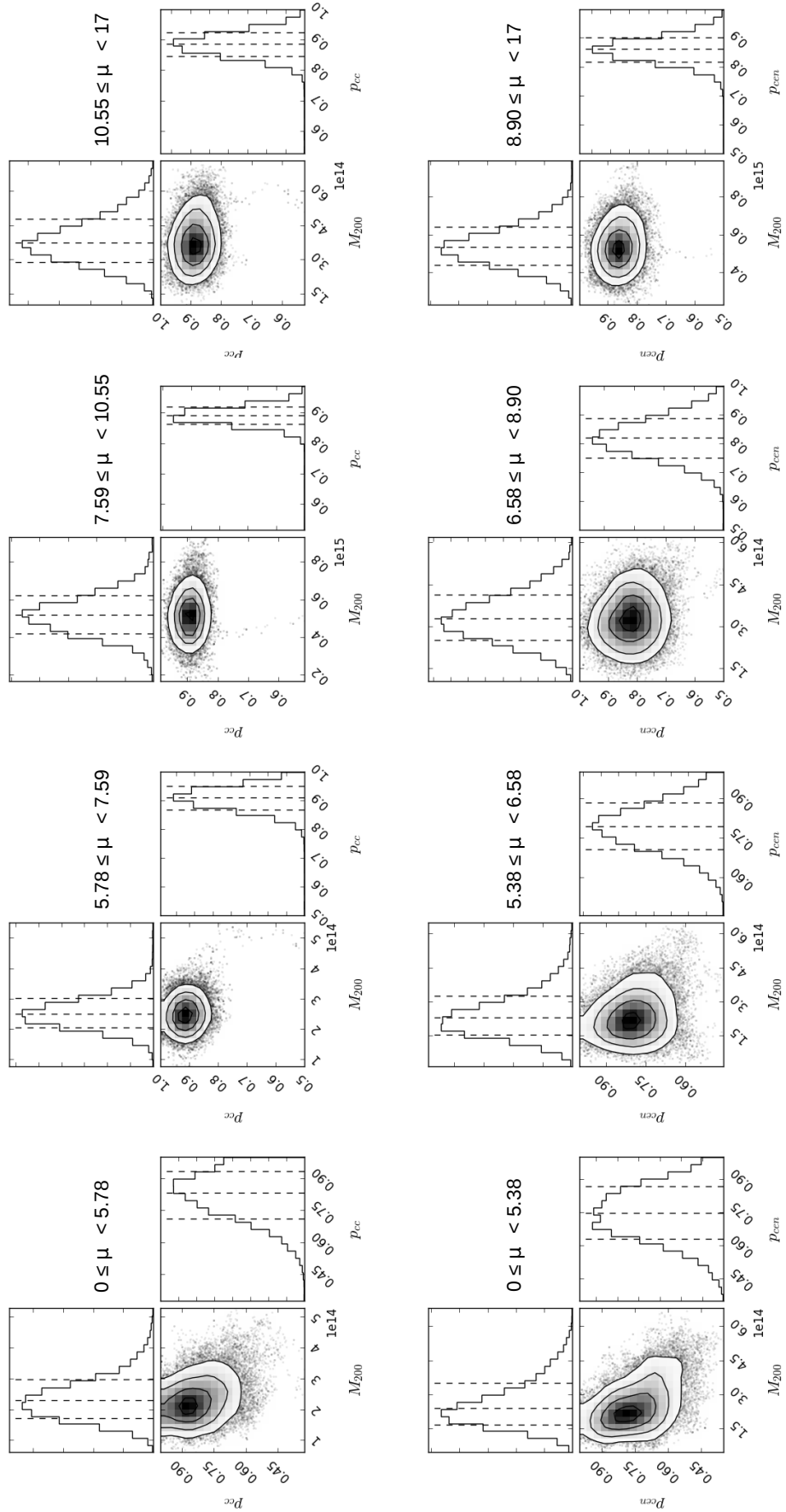


FIGURE 4.6: Triangle plot showing the one and two-dimensional posterior distributions of the parameters (M_{200}, p_{cc}). The concentric contours correspond to the 68%, 95% and 99.7% confidence levels. We show the triangle plots for the profile-fitting of VT clusters in bins of μ_* for the z_{low} (top) and z_{high} (bottom) intervals, using P_{cen}^* for the miscentering prior.

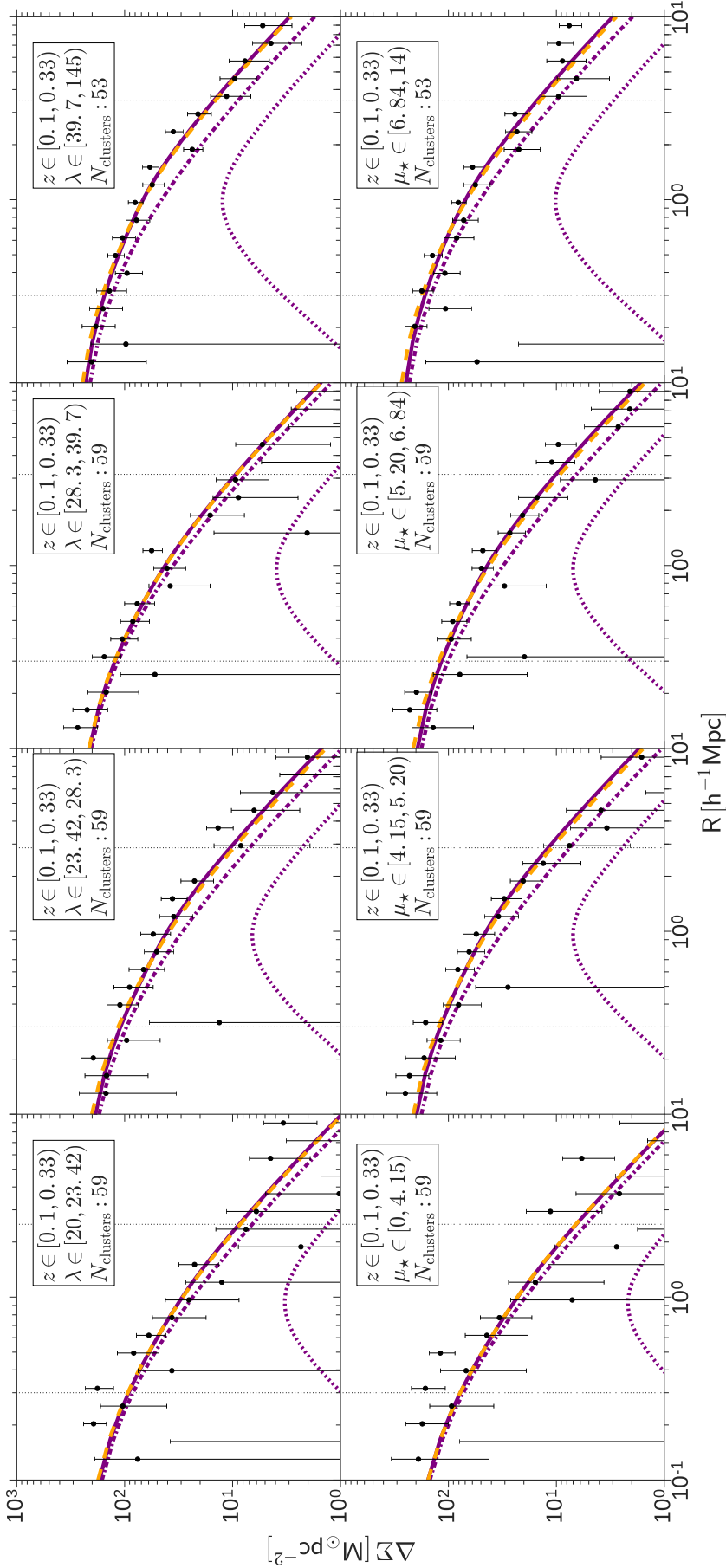


FIGURE 4.7: The $\Delta\Sigma$ measurements and the profile-fitting results for the stacked redMaPPer clusters in the low redshift interval in four observable mass proxy bins. The errorbars are computed with the bootstrap method. In the top panel we show the results for the binning using λ and in the bottom panel the results for binning in μ_* (in units of $10^{12} M_\odot$). The fit to the models is performed for the radial bins within the two vertical dotted lines. The *solid purple* line shows the best-fit results for a combination of NFW and miscentering term, using the information of P_{cen} as a *prior* for the miscentering offset. The *dashed orange* line shows the best-fit using P_{cen}^* as the information for the *prior* when performing the fit. The *dashed-dotted* and *dotted* lines show the contribution of the two terms to the best fit profile: the centered NFW profile $p_{\text{cc}} \Delta\Sigma_{\text{NFW}}$ (*dashed-dotted purple*) and the miscentering term $(1 - p_{\text{cc}}) \Delta\Sigma_{\text{mis}}$ (*dotted purple*).

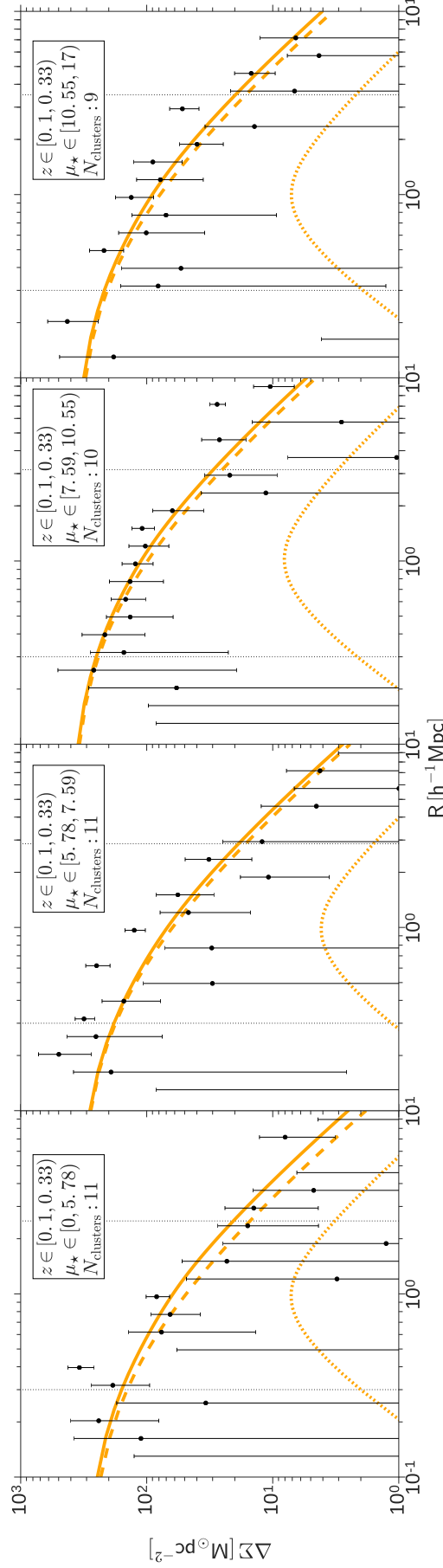


FIGURE 4.8: The $\Delta\Sigma$ measurements and the profile-fitting results for the stacked VT clusters in the low redshift interval in four bins of μ_* (in units of $10^{12} M_\odot$). The errorbars are computed with the bootstrap method. The fit is performed for the radial bins within the two vertical dotted lines. The *solid orange* line shows the best-fit using F_{cen}^* in the *prior* for the miscentering offset in the fit. The *dashed* and *dotted* lines show the contribution of the two terms to the best fit profile: the centered NFW profile (*dashed orange*) and the miscentering term (*dotted orange*).

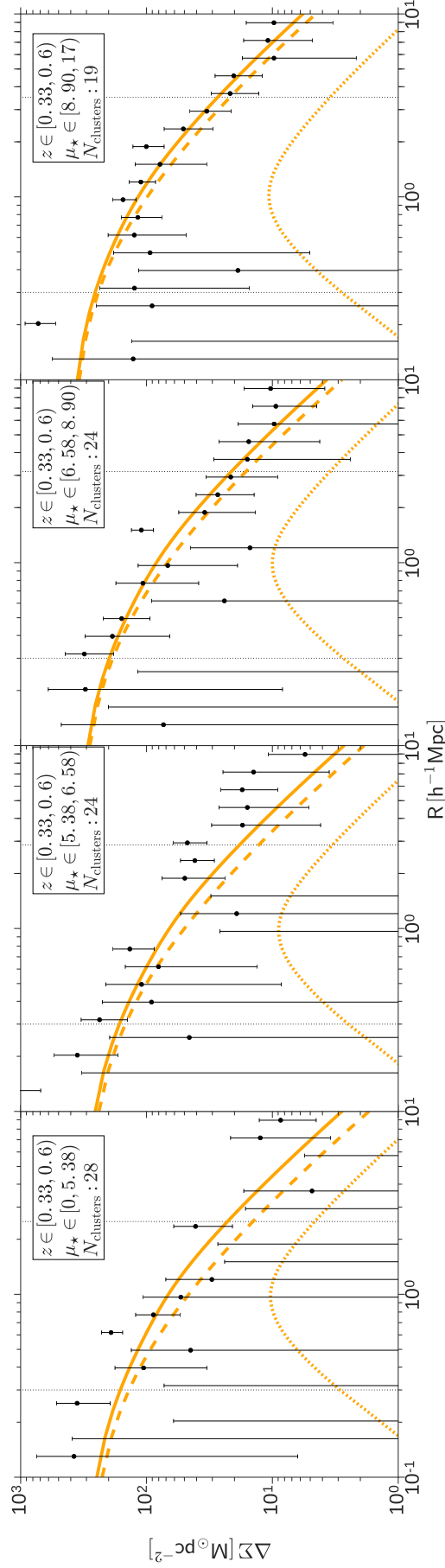


FIGURE 4.9: The $\Delta\Sigma$ measurements and the profile-fitting results for the stacked VT clusters in the high redshift interval in four bins of μ_* (in units of $10^{12} M_\odot$). The errorbars are computed with the bootstrap method. The fit is performed for the radial bins within the two vertical dotted lines. The *solid orange* line shows the best-fit using F_{cen}^* in the *prior* for the miscentering offset in the fit. The *dashed* and *dotted* lines show the contribution of the two terms to the best fit profile: the centered NFW profile (*dashed orange*) and the miscentering term (*dotted orange*).

	z	$M_{200c} (10^{14} h^{-1} M_\odot)$	$M_{200m} (10^{14} h^{-1} M_\odot)$	p_{cc}
redMaPPer				
$20 \leq \lambda < 23.42$		0.83 ± 0.23	1.08 ± 0.30	0.83 ± 0.11
$23.42 \leq \lambda < 28.3$		1.30 ± 0.38	1.71 ± 0.49	0.75 ± 0.13
$28.3 \leq \lambda < 39.7$	$0.1 \leq z < 0.33$	1.30 ± 0.27	1.71 ± 0.35	0.86 ± 0.10
$39.7 \leq \lambda < 145$		2.90 ± 0.55	3.84 ± 0.71	0.71 ± 0.12
$0 \leq \mu_* < 4.15$		0.59 ± 0.19	0.77 ± 0.25	0.86 ± 0.10
$4.15 \leq \mu_* < 5.20$		1.60 ± 0.42	2.10 ± 0.54	0.75 ± 0.13
$5.20 \leq \mu_* < 6.84$	$0.1 \leq z < 0.33$	1.50 ± 0.36	1.97 ± 0.47	0.75 ± 0.13
$6.84 \leq \mu_* < 14$		2.90 ± 0.52	3.82 ± 0.67	0.77 ± 0.11
VT				
$0 \leq \mu_* < 5.78$		2.40 ± 0.65	3.20 ± 0.85	0.82 ± 0.10
$5.78 \leq \mu_* < 7.59$		2.50 ± 0.49	3.27 ± 0.63	0.91 ± 0.04
$7.59 \leq \mu_* < 10.55$	$0.1 \leq z < 0.33$	5.20 ± 1.10	6.86 ± 1.42	0.89 ± 0.03
$10.55 \leq \mu_* < 17$		3.80 ± 0.92	4.97 ± 1.18	0.88 ± 0.04
$0 \leq \mu_* < 5.38$		2.50 ± 0.92	3.09 ± 1.13	0.75 ± 0.12
$5.38 \leq \mu_* < 6.58$		2.40 ± 0.90	2.99 ± 1.11	0.79 ± 0.09
$6.58 \leq \mu_* < 8.90$	$0.33 \leq z < 0.6$	3.30 ± 0.81	4.15 ± 1.00	0.82 ± 0.07
$8.90 \leq \mu_* < 17$		5.50 ± 1.00	7.01 ± 1.25	0.86 ± 0.04

TABLE 4.4: Best-fit results for redMaPPer clusters in Figure 4.7 and for VT clusters in Figures 4.8 and 4.9. In the fitting we use a concentration-mass relation from Duffy et al. [2008] to fix c_{200} and we fix the width of miscentering distribution as $\sigma_{\text{off}} = 0.4 h^{-1} \text{ Mpc}$. Our final model has just two free parameters, the mass M_{200} (computed using the critical density and converted to the mean density with Colossus) and the fraction of clusters that is correctly centered p_{cc} . For the redMaPPer clusters, we use the mean and standard deviation (σ) of P_{cen} in a Gaussian prior for p_{cc} , while for the VT clusters we use the mean and σ of P_{cen}^* for the Gaussian prior. The values of μ_* that define each stack are given in units of $10^{12} M_\odot$. The uncertainties reported are statistical only.

In this work, the mass-richness relation for the redMaPPer mass proxy λ is given by the power law expression

$$\langle M_{200} | \lambda \rangle = M_0 \left(\frac{\lambda}{\lambda_0} \right)^\alpha, \quad (4.14)$$

where λ_0 is a fixed pivot richness and the normalization M_0 and the slope α are the free parameters.

For the new mass proxy we fit a power-law relation to the mass obtained in the μ_* bins akin to Equation (4.14):

$$\langle M_{200} | \mu_* \rangle = M_0 \left(\frac{\mu_*}{\mu_*^0} \right)^\alpha, \quad (4.15)$$

where the pivot value μ_*^0 is chose as the median value of the proxy in each sample.

4.3.1 redMaPPer mass-richness relation

To validate our mass estimates we make a comparison with S17, which uses the same redMaPPer catalog in the same low redshift bin to compute a mass-richness relation. However, the analysis in

	$M_0(10^{14}h^{-1}M_\odot)$	α
This work	2.46 ± 0.44	1.18 ± 0.38
Simet et al. 2017	2.21 ± 0.22	$1.33_{-0.10}^{+0.09}$
Melchior et al. 2017	2.21 ± 0.35	1.12 ± 0.20
Oguri et al. 2014	2.53 ± 0.30	1.44 ± 0.27

TABLE 4.5: Comparison of the redMaPPer mass-richness relation in the z_{low} bin with three recent results from the literature. The normalization M_0 from Melchior et al. [2017] is converted to our units. We also have to convert M_0 from Oguri [2014] to our units and find a relation between their richness \hat{N}_{cor} and λ . All calibrations are computed or converted to the pivot $\lambda_0 = 40$.

S17 is not limited to the SDSS Stripe 82 region, which implies that they have more statistics than us. On the other hand, our shape measurements are made in better quality images than SDSS and using the state-of-the-art code Lensfit, which enables us to have a good SNR for our lensing signal to make this comparison.

In Figure 4.10 we show our best-fit M_{200m} versus λ relation (*orange solid* line) and its 2σ confidence intervals (*orange shaded* regions). We show, for comparison, the S17 mass-richness relation (*green solid* line). Using the same pivot richness as S17, $\lambda_0 = 40$, we find $M_0 = (2.46 \pm 0.44) \times 10^{14}h^{-1}M_\odot$ and $\alpha = 1.18 \pm 0.38$ while they have obtained $M_0 = (2.21 \pm 0.22) \times 10^{14}h^{-1}M_\odot$ and $\alpha = 1.33_{-0.10}^{+0.09}$. Additionally, we present the mass-richness relation obtained by [Melchior et al. 2017, *blue dashed* line] for clusters identified with redMaPPer in the DES Science Verification data, with shears measured on that same data, in a similar low redshift bin ($0.2 < z_{\text{low}} < 0.4$). Their results, converted to our units and pivot $\lambda_0 = 40$, are $M_0 = (2.21 \pm 0.35) \times 10^{14}h^{-1}M_\odot$ and $\alpha = 1.12 \pm 0.20$.

We also compare our results to the mass-richness relation for the red sequence based CAMIRA code of Oguri [2014]. The CAMIRA code was applied to the same SDSS DR8 data and has its own richness estimator, \hat{N}_{cor} . In order to convert their result to our units, we first performed a cylindrical match between our sample and their catalog to find the mean relation between \hat{N}_{cor} and λ . Our cylindrical match uses a search radius of 1 arcmin and $\Delta z = 0.05$. We found 339 matched clusters from which we derived the CAMIRA-redMaPPer richness scaling relation $\hat{N}_{\text{cor}} = A\lambda$ with $A = 0.819 \pm 0.009$. The mass calibration for CAMIRA is obtained for $M_{200\text{vir}}$, which we convert to M_{200m} using Colossus, and we converted their calibration to the pivot $\lambda_0 = 40$ as well. We find that their converted results are $M_0 = (2.53 \pm 0.30) \times 10^{14}h^{-1}M_\odot$ and $\alpha = 1.44 \pm 0.27$. These results are summarized in Table 4.5.

Despite using different data and slightly different approaches, we see that our mass measurements are in excellent agreement with those results from the literature, which validates our methodology to obtain average mass estimates from the stacked weak lensing signal.

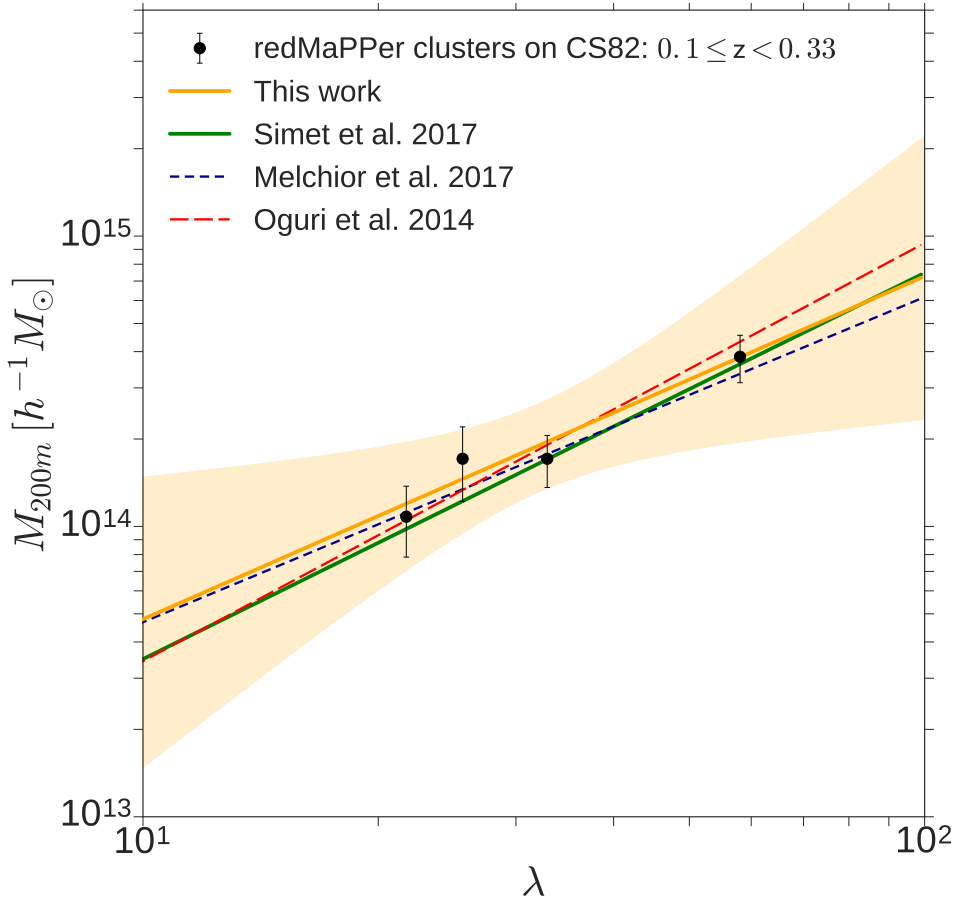


FIGURE 4.10: Comparison of the mass-richness relations of redMaPPer clusters in the z_{low} interval. The adopted z_{low} interval is the same for S17 (green solid line) and this work (orange solid line). Melchior et al. [2017, blue dashed line] work in the range $0.2 \leq z < 0.4$ while Oguri [2014, red dashed line] use the range $0.1 < z < 0.3$ for its low redshift interval. We show the 2σ confidence intervals (orange shaded region) for the cluster mass M_{200m} as a function of the richness λ from this work. The value of the normalizations and slopes are shown in Table 4.5. The uncertainties in the mass are statistical only.

As mentioned, we also computed μ_* for the redMaPPer clusters. We fit the power-law relation of Equation (4.15) with pivot value $\mu_*^0 = 5.16 \times 10^{12} M_\odot$. We find $M_0 = (1.77 \pm 0.36) \times 10^{14} h^{-1} M_\odot$ and $\alpha = 1.74 \pm 0.62$. In Figure 4.11 we show the best fit $M_{200m} \times \mu_*$ relation (solid orange line) and its 2σ confidence intervals (orange shaded region) for the z_{low} interval.

4.3.2 VT – μ_* mass-calibration

In Figure 4.12 we show $M_{200m} \times \mu_*$ for VT clusters in the z_{low} interval, following the same approach we used to calibrate the mass as a function of μ_* in the redMaPPer cluster sample. The *orange solid* line is the best-fit result and the *orange shaded* regions are the 2σ confidence intervals for this VT sample. The pivot is $\mu_*^0 = 7.30 \times 10^{12} M_\odot$ and we find $M_0 = (4.31 \pm 0.89) \times 10^{14} h^{-1} M_\odot$

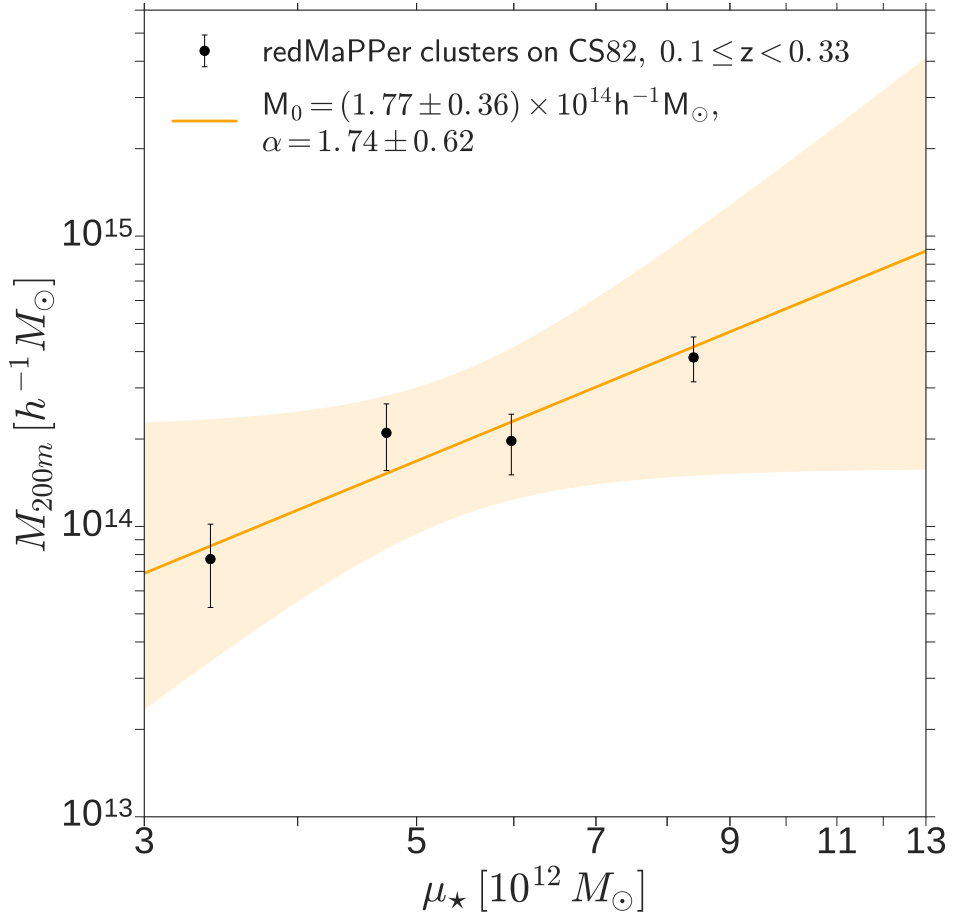


FIGURE 4.11: Mass-calibration with 2σ confidence intervals for redMaPPer clusters binned in μ_* in the z_{low} interval. For the mass estimates we apply the miscentering correction. In the mass– μ_* relation we adopt the median of μ_* as the mass proxy pivot, $\mu_*^0 = 5.16 \times 10^{12} M_\odot$. The uncertainties in the mass are statistical only.

and $\alpha = 0.59 \pm 0.54$. For comparison, we show as *purple shaded* regions the same 2σ confidence intervals obtained for the redMaPPer clusters shown in Figure 4.11. We see a good agreement at this confidence level, despite the fact that the cluster samples are significantly different. Actually if we consider the VT and redMaPPer data points altogether, i.e., if we combine the VT μ_* bins and corresponding masses and the redMaPPer μ_* bins and respective masses, we obtain a power-law fit as good as the one for the VT points only. In other words the redMaPPer mass– μ_* relation is compatible the the VT one.

We present the mass-calibration results for the z_{high} interval of VT clusters in Figure 4.13. The *solid orange* line and *orange shaded* regions are the best-fit and the 2σ confidence intervals, respectively. We have used a pivot $\mu_*^0 = 6.30 \times 10^{12} M_\odot$ and find $M_0 = (3.67 \pm 0.56) \times 10^{14} h^{-1} M_\odot$ and $\alpha = 0.68 \pm 0.49$. As previously mentioned, we were able to extend our analysis of the VT sample to the higher redshift range $0.33 < z < 0.6$ because the VT clusters were identified in the SDSS co-add

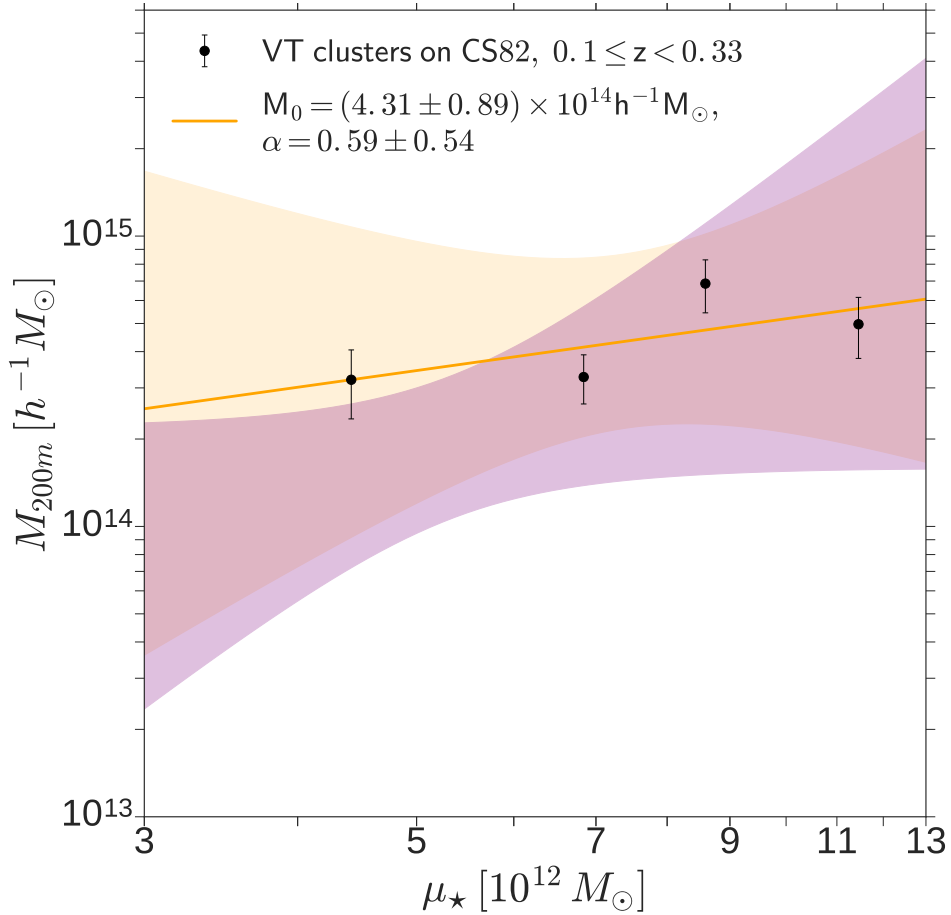


FIGURE 4.12: Mass-calibration with 2σ confidence intervals (*orange shaded regions*) for VT clusters binned in μ_\star in the z_{low} interval. Miscentering corrections were applied in the mass estimates. In the mass-richness relation the pivot is $\mu_\star^0 = 7.30 \times 10^{12} M_\odot$. For comparison, we also present the 2σ confidence intervals (*purple shaded regions*) for the redMaPPer z_{low} clusters. The uncertainties in the mass are statistical only.

Sample	$\mu_\star^0 (10^{12} M_\odot)$	$M_0 (10^{14} h^{-1} M_\odot)$	α
RM z_{low}	5.16	1.77 ± 0.36	1.74 ± 0.62
VT z_{low}	7.30	4.31 ± 0.89	0.59 ± 0.54
VT z_{high}	6.30	3.67 ± 0.56	0.68 ± 0.49

TABLE 4.6: Summary of mass- μ_\star calibration for redMaPPer (RM) and VT clusters obtained from this work. We present the normalization M_0 and slope α values by fitting the Equation 4.15 as well the proxy pivot μ_\star^0 adopted for each sample, i.e. RM clusters at $0.1 \leq z_{\text{low}} < 0.33$ and VT clusters in the same RM low redshift bin as well as a high redshift bin $0.33 \leq z_{\text{high}} < 0.6$.

data, which is deeper than SDSS single epoch data used to identify the redMaPPer sample. In addition, the CS82 shear catalog is still reliable for lenses at these redshifts. The results of the all mass- μ_\star calibrations are summarized in Table 4.6.

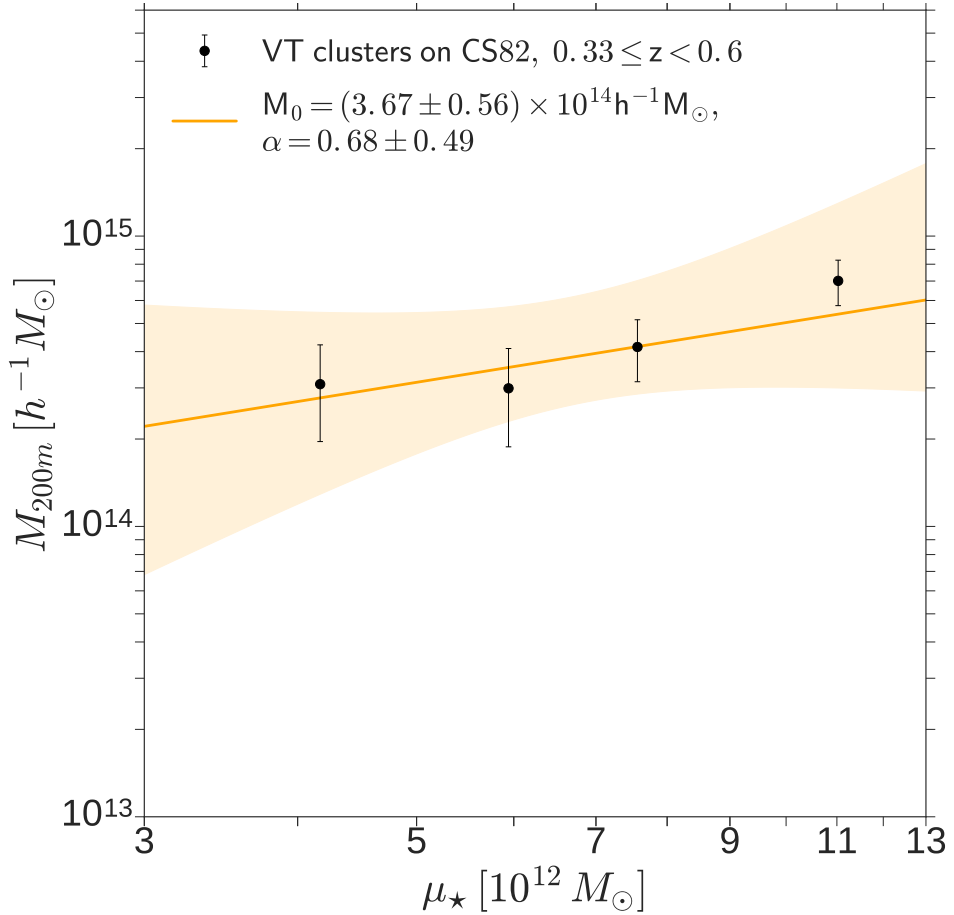


FIGURE 4.13: Mass-calibration with 2σ confidence intervals (*orange shaded regions*) for VT clusters binned in μ_\star in the z_{high} interval and pivot $\mu_\star^0 = 6.30 \times 10^{12} M_\odot$. The uncertainties in the mass are statistical only.

4.4 Matching redMaPPer and VT clusters

As we mentioned, some of the most popular methods to find clusters rely on the assumption that such objects are formed by an agglomeration of red galaxies. These red-sequence methods, however, will have diminished performance for clusters with a large blue-to-red fraction of galaxies and lacking the red-sequence feature (“blue clusters”). Blue clusters are expected to be a small fraction of the total number of clusters, but might be a selection effect that is not taken into account.

In addition to the mass-calibration analysis, we performed a more detailed study of the redMaPPer and VT clusters, in order to identify possible blue clusters. We assume that if we performed a matching between redMaPPer and VT clusters and find unmatched VT clusters, this would be an evidence for the presence of blue clusters. The key point is to have a precise procedure to match the catalogs. In order to do that, we chose to follow a procedure based on the positional matching and fractions of members, to avoid the matching of clusters at different redshifts, for example. These

fractions f are defined as the number of matchings with respect to the number of members in common for a given catalog, $f = \frac{N_{\text{VT,RM}}^{\text{match}}}{N_{\text{RM,VT}}^{\text{members}}}.$

In practice, we perform the positional matching of the member in the catalogs in a radius of 1 arcmin, which is the typical scale for the angular size of galaxies. Each member in both catalogs has the host cluster ID. Then, after the matching we can group this members again and identify how many clusters remain. After, we apply a cut in z and richness to keep the most massive clusters. Then, we take one of the catalogs as reference e compute the matching fractions. In our final matching catalog, only clusters that share more than 50 % of the members are kept, i.e. clusters with $f > 0.5$. It is important to note that in the grouping step, some of the clusters are identified as multiple objects in the other catalog. To solve this issue, we rank the clusters by richness and just keep the ones that present more shared members. For instance, if a redMaPPer cluster is identified as 3 others VT clusters that have 20, 10 and 5 shared members, we just keep the VT cluster with 20 shared member as the matched cluster and then compute its matching fractions.

After apply this procedure both taking RM and VT as reference catalog, we obtained a final matching catalog of 53 clusters and 30 unmatched VT clusters. We investigate this unmatched clusters and after some tests, we just found out that this VT clusters were not in redMaPPer catalog because of the applied mask. Then, our hypothesis that we could have selection effects due to the galaxy population in the cluster did not hold, giving evidence that redMaPPer is a robust method to identify galaxy clusters.

4.5 Weak lensing on SOGRAS

As we have discussed in Section 3.3, SOGRAS is a survey that observed 47 galaxy clusters and some of them are in the CS82 footprint. Also, the SOGRAS clusters had their masses measured by Cibirka [2013] through the velocity dispersion technique (i.e. dynamical mass). Since we have the shape measurements for some of them, we could also perform a weak lensing analysis in this sample to estimate their masses and compare with the dynamical masses. In the CS82 footprint there are 28 SOGRAS clusters (see Figure 4.14), which are used in our weak lensing mass estimates. For the dynamical analysis all the 47 clusters were used. In this section, I describe the preliminary results for the weak lensing mass measurements for the SOGRAS survey. In this analysis we use the tools and methods described in the previous sections.

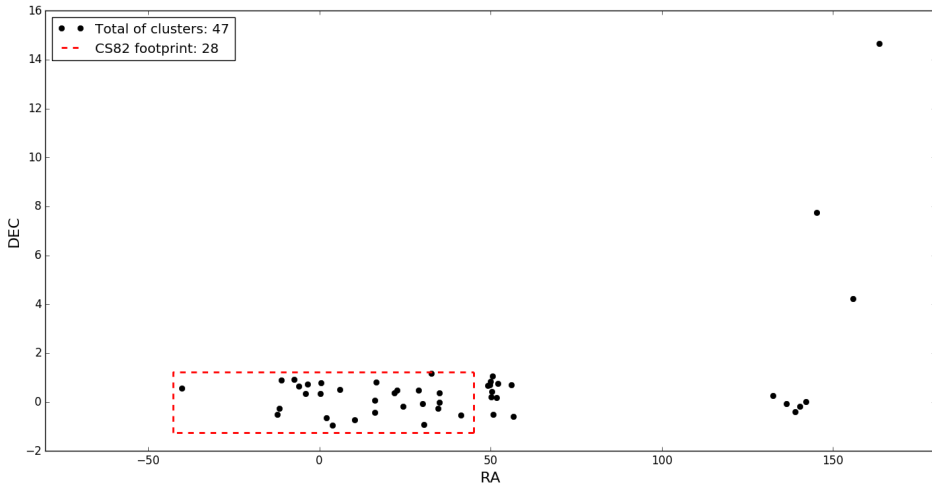


FIGURE 4.14: Sky distribution of SOGRAS clusters in the CS82 footprint.

First, we reproduce the same binning scheme of the dynamical estimates. The clusters are divided in two redshift bins, centered in $z = 0.3$ and $z = 0.5$, and in a low and a high richness N_{gals} ⁶ intervals of $N_{gals} < 35$ (low) and $N_{gals} \geq 35$ (high), respectively. We also compute the mass estimates without this richness binning.

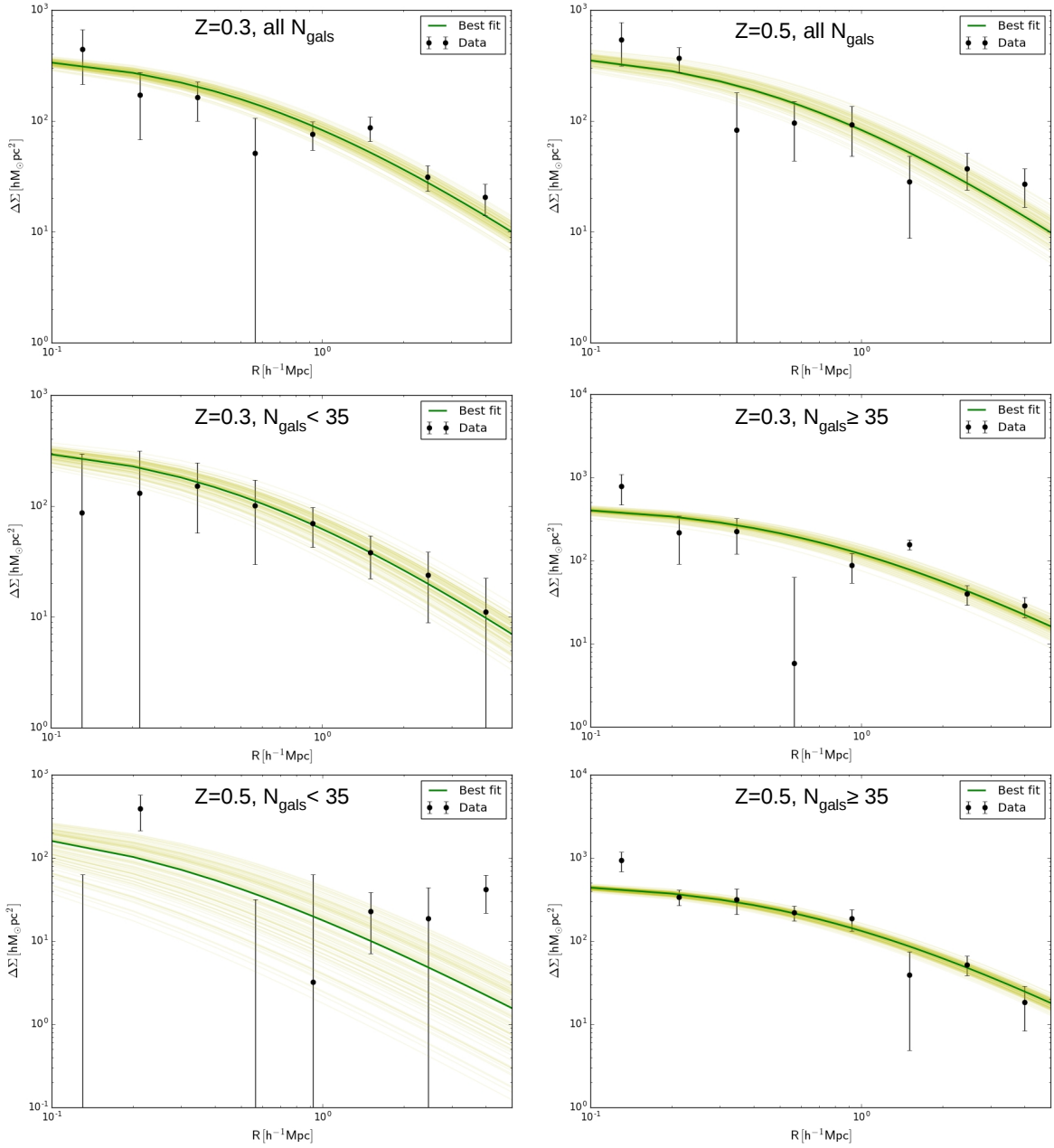
We perform a simple NFW profile-fitting to these samples in 8 logarithmic bin from $0.1 - 5 h^{-1}$ Mpc and fix the concentration by a Duffy concentration-mass relation.

In Figure 4.15 we present our preliminary results for the measured signal (black dots) together with the best-fit model (green curve) and projection of our MCMC results into the space of the observed data, i.e. 100 samples from the MCMC chains (yellow curves). In Table 4.7 we summarize our weak lensing preliminary results in comparison with the dynamical estimates.

z	N_{gals}	$M_{\text{dyna.}} (10^{14} M_{\odot})$	$M_{\text{WL}} (10^{14} M_{\odot})$
0.3	all	$6.33_{-3.87}^{+2.14}$	$2.10_{-0.42}^{+0.40}$
0.5	all	$8.60_{-5.20}^{+1.58}$	$1.97_{-0.56}^{+0.49}$
0.3	low	$3.46_{-2.62}^{+0.83}$	$1.41_{-0.50}^{+0.43}$
0.3	high	$10.4_{-7.50}^{+3.96}$	$3.79_{-0.65}^{+0.62}$
0.5	low	$6.82_{-5.88}^{+1.78}$	$0.20_{-0.25}^{+0.14}$
0.5	high	$13.6_{-3.40}^{+6.53}$	$3.97_{-0.71}^{+0.69}$

TABLE 4.7: Preliminary results for SOGRAS cluster weak lensing masses in different bins of z and richness.

⁶The richness N_{gals} is computed with the code ECGMM [Hao et al. 2010] and the intervals were chosen such that each richness bin has a similar number of clusters for the dynamical mass analysis.

FIGURE 4.15: Best-fit results for SOGRAS clusters in different bins of z and richness N_{gals} .

In this preliminary analysis we can see a discrepancy in the mass estimates. The weak lensing masses are systematically lower than the dynamical masses. However, we should have a more careful look in the profile-fitting choices, since this preliminary analysis was done with arbitrary choices (e.g. radial range for the fit, concentration-mass relation, etc). The interesting thing is that even though we just have 28 clusters, we still have an appreciable lensing signal for most of the samples.

Chapter 5

Summary

In this chapter I summarize the results of the projects developed in this thesis, with a focus on the main topic of weak lensing mass-calibration of redMaPPer and VT clusters with the new mass proxy μ_\star . Other studies were carried out during the PhD, including searches for strong lenses, strong lensing modeling and galaxy morphometry.

5.1 Imaging surveys

In Chapter 3, I described the surveys which provided the data used throughout this thesis. In particular, SOGRAS, CS82 and VICS82 were planned and motivated for gravitational lensing studies. In SOGRAS I have participated from the target selection in the two observing seasons (which is described in [Furlanetto et al. \[2013\]](#)) to developing strong lensing studies to estimate the cluster mass from the curvature radius (however, this project is still in its early stages, see Section 5.2). Recently, I have measured the weak lensing signal for 28 SOGRAS clusters that are in the CS82 footprint. In this analysis we have split the clusters in redshift ($z = 0.3$ and $z = 0.5$) and richness ($N_{gals} \leq 35$ and $N_{gals} > 35$) bins in order to perform the stacked measurements and determine the cluster mass to be compared with the dynamical mass estimates from [Cibirka \[2013\]](#). The preliminary results show a discrepancy between the weak lensing and dynamical masses, with the weak lensing estimates systematically lower. However, this analysis should be reviewed in more details, specially in relation to the choices in the profile-fitting. The results from this work will be described in [Pereira et al. \[2018a\]](#) (in preparation), together with the characterization of the strong lensing systems.

Most of the work I developed in this thesis was related to the CS82 survey. This survey has an excellent imaging quality as was designed for weak and strong lensing studies. I participated in several analyses developed for this survey. First, I performed tests to determine the optimal configurations with SExtractor to obtain a detection catalog of the objects in the images. These catalogs were crucial for all analyses carried out in CS82 (e.g. shape measurements with Lensfit, photo-z with BPZ, etc). Because of this contribution, I participated in several publications of the CS82 collaboration [[Comparat et al. 2013](#), [Charbonnier et al. 2017](#), [Leauthaud et al. 2017](#), [Niemiec et al. 2017](#), [Shan et al. 2017](#), [Wang et al. 2018](#)].

Once we generated the detection catalogs, we were also able to obtain the morphology catalogs for the survey. I developed similar tests for the optimal configurations in the object model-fitting with SExtractor+PSFEx. I have also compared the morphological parameters derived from this analysis, mainly the ellipticity of the objects, with the ones obtained from standard weak lensing codes (Lensfit and Imcat). I have found that SExtractor+PSFEx has comparable estimates with them, which make us confident that our morphological catalogs are robust to be apply in scientific studies. The first applications of the morphometric catalogs are described in [Charbonnier et al. \[2017\]](#) and [Soo et al. \[2018\]](#). Finally, I performed stacking weak lensing measurements with the CS82 shape catalog, which is described in Section 5.3 and in the submitted paper [Pereira et al. \[2018b\]](#).

CS82 motivated VICS82 [[Geach et al. 2017](#)], which is an infrared survey performed in the same footprint as CS82. VICS82 aims to have applications in gravitational lensing, quasars and galaxy evolution studies among others scientific cases. I started to work with VIC82 data in the checking of object detections and generation of masks for the survey images in order to have catalogs with good quality for scientific applications. For future work, we are interested in using VICS82 data for the stellar mass estimates, which might be useful to improve our μ_* mass proxy.

5.2 Strong lensing studies

In Appendix B, I describe the strong lensing studies in which I have been involved during the past years. I have started these studies by participating in visual searches for strong lensing systems such as the one described in [Nord et al. \[2016\]](#).

I have also started to be familiar with the mass estimates from strong lensing systems through the curvature radius of gravitational arcs obtained with Mediatrix code. Although the way Mediatrix works is simple, the big difficulty is to provide a good input image for the code, with isolated and not

fragmented objects. I have been working in this issue with SOGRAS data. Once I have optimized the input images for Mediatrix, it will be straightforward to obtain the mass estimates from the curvature radius, allowing the comparison with dynamical and inverse modeling estimates [Pereira et al. 2018a].

5.3 Weak lensing mass-calibration of VT and redMaPPer clusters

The main result of this thesis is described in Chapter 4, namely the weak lensing mass-calibration of redMaPPer and VT clusters in bins of redshift and two different mass proxies.

We perform a weak lensing mass calibration of μ_* , a cluster mass proxy that includes information about galaxies regardless of their color. Unlike the empirically determined red sequence-based mass proxies, μ_* is physically motivated: the stellar mass inside a dark matter halo can be expected to trace the dark matter halo mass. Furthermore, it turns out that the stellar mass is a relatively robust observable [see Conroy 2013, and references therein] and independent of the history of the formation of the red sequence. The redshift at which the red sequence forms in clusters is not currently known, and at high enough redshifts redMaPPer will become increasingly incomplete in terms of finding dark matter halos. Additionally, stellar masses are easier to model in simulations than the red sequence [e.g., Roediger et al. 2017].

It is natural to use a well studied sample of clusters in the development of a new mass proxy, and to use a well-studied mass proxy to validate our methodology. We have measured the redMaPPer λ -mass scaling relation and showed results consistent with similar scaling relations reported in the literature. We then performed the scaling relation measurement on the same redMaPPer clusters binning on μ_* instead of λ . The most direct comparison between the two scaling relations is made at the pivot point: the slope and the mass at the pivot point are consistent between the λ and μ_* proxies.

Since we applied the methodology on the same clusters in measuring both scaling relations, our results can be directly interpreted. Imagine a scenario in which all cluster members are in the red sequence. There would be a maximal correlation between λ and μ_* as all red galaxies have very similar mass-to-light ratios. The scaling relations would, therefore, be nearly identical. If we change the scenario to include blue galaxies and compute a λ -like proxy, the slope of the λ -like proxy with mass would be shallower because the luminosity of the blue galaxies is most often driven by single star formation events and the high luminosity of young massive stars, and large numbers of low

luminosity galaxies would be pushed above the threshold. If the μ_* proxy were similarly affected by blue galaxies our measured slope would be shallow. The fact that our measurements of the scaling relations in redMaPPer are so close to each other indicate that the stellar mass in these systems is tracing dark matter mass with not much worse scatter than λ . In low z clusters it is known that nearly all members are red and therefore our results are not surprising here. At high redshift, however, this is not true. A red-sequence selected high z sample might show a significant difference between λ and μ_* mass calibrations as the red sequence begins to form.

We explore the applicability of our methodology to color agnostic cluster finders by performing the scaling relation measurement of VT clusters. The results are again consistent with those obtained for the redMaPPer clusters in this redshift range, as expected, indicating that our methods hold for other cluster selection algorithms. A clear result of our work is the recommendation that μ_* be incorporated as the mass proxy for VT clusters.

Appendix A

Bayesian approach and MCMC

To perform the profile-fitting we use the Bayesian formalism together with the Markov Chain Monte-Carlo (MCMC) method. In the following, we will briefly review these methods largely based on [van Ravenzwaaij et al. \[2018\]](#) and [Lee and Wagenmakers \[2014\]](#). The general principles of Bayesian inference rely on the use of the information from the observed data X about a set of parameters θ , i.e. the likelihood, to update a prior state of beliefs about θ to become a posterior state of beliefs about θ . Formally, the Bayes's rule specifies how we can combine the likelihood $Pr(X|\theta)$ with the information of the prior distribution $Pr(\theta)$, to arrive at the posterior distribution $Pr(\theta|X)$

$$Pr(\theta|X) = \frac{Pr(X|\theta)Pr(\theta)}{Pr(X)}. \quad (\text{A.1})$$

This equation is often stated as

$$\text{posterior} = \frac{\text{likelihood} \times \text{prior}}{\text{evidence}}, \quad (\text{A.2})$$

where the evidence (i.e. $Pr(X)$) is the probability of the observed data. It does not involve the parameters θ and is given by a single number that ensures that the area under the posterior distribution equals 1. Equation [A.1](#) is commonly written as

$$Pr(\theta|X) \propto Pr(X|\theta)Pr(\theta), \quad (\text{A.3})$$

which says that the posterior is proportional to the likelihood times the prior. In summary, the posterior distribution is a combination of what we knew before we saw the data (i.e., prior distribution), and what we have learned from the data.

In general, the posterior distribution for a restricted set of relatively simple models can be obtained analytically. In practice, one does not have access to such an analytical expression for posterior distributions. In Bayesian inference, this problem is most often solved via MCMC, which is a computer-driven sampling method. It allows one to characterize a distribution without knowing all of the distribution's mathematical properties by randomly sampling values out of the distribution.

The method combines two features: Monte-Carlo and Markov chain. Monte-Carlo is the practice of estimating the properties of a distribution by examining random samples from the distribution. The Markov chain feature of MCMC is the idea that the random samples are generated by a special sequential process. Each random sample is used as a stepping stone to generate the next random sample (hence the chain). A special property of the chain is that, while each new sample depends on the one before it, new samples do not depend on any samples before the previous one (this is the “Markov” property). Then, MCMC is particularly useful in Bayesian inference because of its ability of drawing a sequence of samples from the posterior, and examining their mean, range, and so on. From MCMC techniques such as Gibbs sampling or the Metropolis-Hastings algorithm, we can directly sample sequences of values from the posterior distribution of interest, forgoing the need for closed-form analytic solutions.

To describe the basic idea of the Metropolis-Hastings algorithm [[Metropolis et al. 1953](#), [Hastings 1970](#)], we closely follow references [Marshall \[2003\]](#), [Robert \[2015\]](#), [Zheng \[2016\]](#). Given a probability density π called the *target*, defined in the state (i.e parameter) space \mathcal{X} , which is known only up to some multiplicative constant , $\pi(\theta) \propto \tilde{\pi}(\theta)$, the Metropolis-Hastings algorithm proposes a generic way to construct a Markov chain on \mathcal{X} that is ergodic and stationary with respect to π – meaning that, if $\mathbf{x}^{(t)} \sim \pi(\theta)$, then $\mathbf{x}^{(t+1)} \sim \pi(\theta)$ – and that therefore converges in distribution to π . If the chain is running for a sufficiently long time, the generated values from the chain can be regarded as an approximate sample from the target distribution and used as a basis for summarizing important characteristics of π . The standard approach to generate a Markov chain with an invariant distribution π consists of using the Metropolis-Hastings algorithm where new values θ^* are drawn from an arbitrary *proposal* distribution q and then to be accepted or rejected according to the acceptance function

$$A(\theta, \theta^*) = \min \left\{ 1, \frac{\tilde{\pi}(\theta^*|X)q(\theta|\theta^*)}{\tilde{\pi}(\theta|X)q(\theta^*|\theta)} \right\}, \quad (\text{A.4})$$

where the candidate $\mathbf{x}^{(t+1)}$ is more likely than $\mathbf{x}^{(t)}$, if $A \geq 1$. That is how the algorithm covers the parameter space \mathcal{X} .

This accept-reject criteria is therefore sufficient to turn a simulation from an almost arbitrary proposal density q into a generation that preserves π as the stationary distribution. In other words, this algorithm enables us to compute the posterior distribution – $\pi(\theta|X) = Pr(\theta|X) \propto Pr(X|\theta)Pr(\theta)$ – of our Bayesian approach. In our notation, implementing the Metropolis-Hastings algorithm requires computing the acceptance function

$$A(\theta, \theta^*) = \min \left\{ 1, \frac{Pr(\theta^*|X)Pr(\theta^*)q(\theta|\theta^*)}{Pr(\theta|X)Pr(\theta)q(\theta^*|\theta)} \right\}. \quad (\text{A.5})$$

Appendix B

Strong Lensing studies

B.1 Arcs visual search in DES

As described in [Nord et al. 2016], the visual inspection carried out in the DES SV images relied on morphology and color to identify lens candidates. In this inspection we searched for arc- and ring-like features, and multiple imaged sources, in association with red lensing galaxies or galaxy groups. Another typical search criteria is to look for blue source images in association with red galaxies, but some systems with red source images were also identified.

Two types of visual inspections were performed: a non-targeted search of all ~ 250 sq. deg. of the SV DES data and a targeted inspection of previously identified galaxy clusters. I have participated in the non-targeted search, examining 11 tiles from a total of 136 distributed between the inspectors. The combined non-targeted and targeted search samples were merged, and assessed by a team of experienced inspectors that ranked the systems and obtained a result of 53 promising candidates. From this sample, 24 candidates were selected because they were most suitable for spectroscopic follow-up. After the observations, 6 candidates were confirmed as new strong lensing systems (see Figure B.1).

B.2 Morphometric modeling with Mediatrix

Recently, a large number of surveys to search for strong lensing system have been carried out. Currently, 674 systems¹ are known and this number will continue to increase with the current and

¹<http://admin.masterlens.org/index.php>

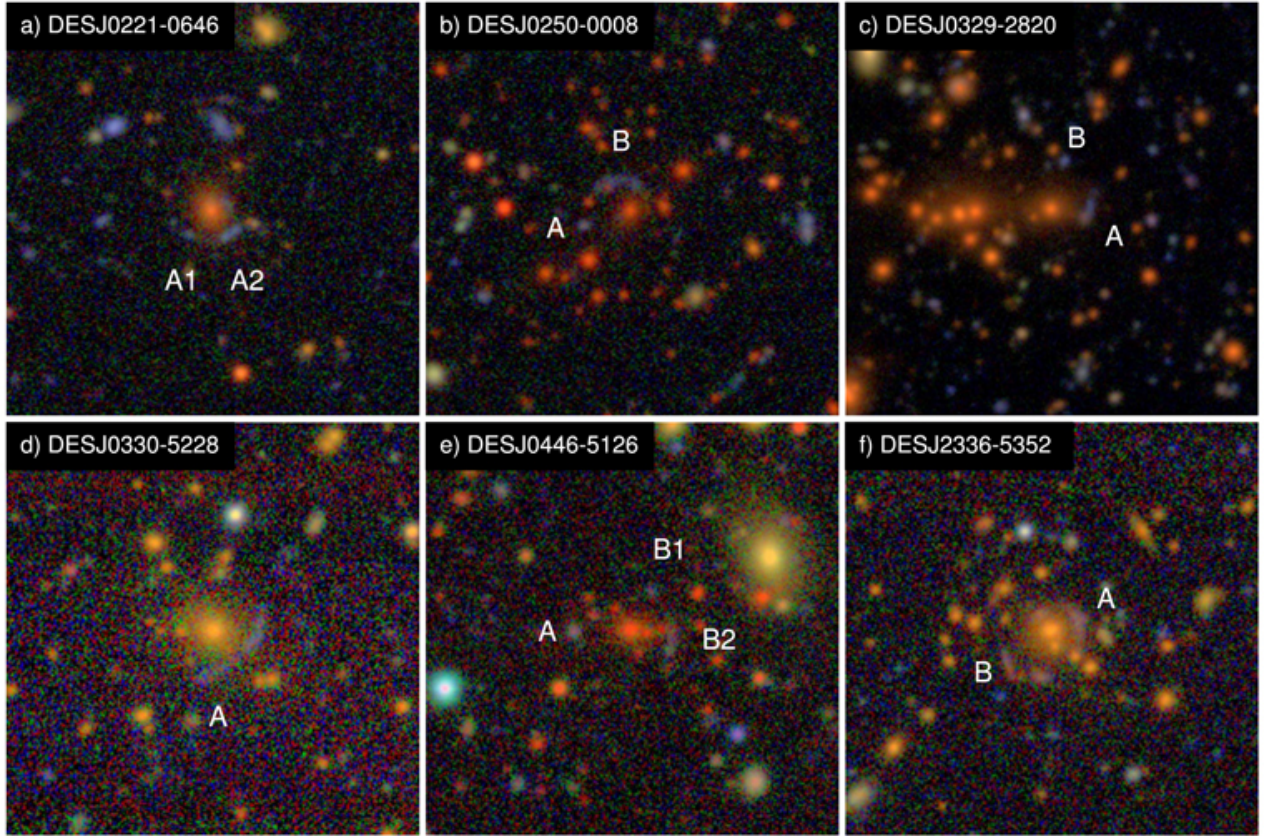


FIGURE B.1: Color coadded DES images of the six spectroscopically confirmed strong lensing systems. Credits: Nord et al. [2016]

future surveys wide-field imaging surveys. These systems can be used to model the mass of galaxies and clusters. As shown in Section 2.2, the mass modeling can be done through the curvature radius of the systems or by the inverse modeling technique applied to multiple images, with algorithms such as *lenstool*². Caminha [2014] presented the modeling with *lenstool* for two of the 47 clusters of the SOGRAS survey.

In addition, many more systems with arcs allow us to estimate a curvature radius than those who have multiple images. For the case of mass modeling via curvature radius, it is important to verify that there is no biases in mass measurements.

In this analysis we are interested in comparing the results of the inverse modeling from Caminha [2014] with estimates from the curvature radius. We also want to obtain the mass estimates for SOGRAS clusters by this technique, even if there are no independent estimates to compare. In the following we describe the code that allows implementing this technique, the *Mediatrix*, and its preliminary results obtained for the SOGRAS clusters.

²<https://projets.lam.fr/projects/lenstool/wiki>

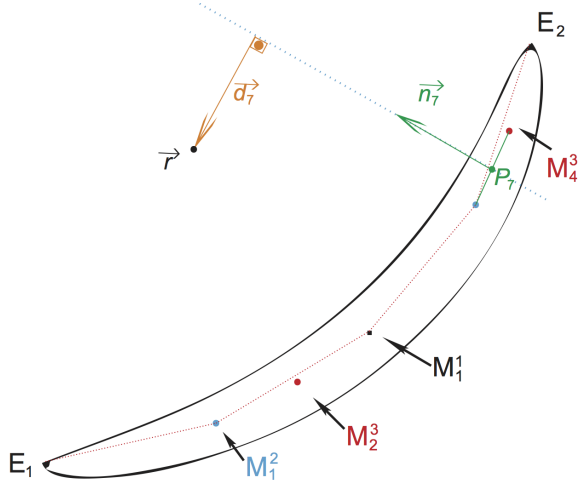


FIGURE B.2: Steps in the Mediatrix Filamentation method for a iteration of $n = 3$ in a object ArcEllipse. For clarity, only one vector and some points and segments are shown. Credits: [Bom et al. \[2017\]](#).

The Mediatrix [[Bom et al. 2012](#), [Bom et al. 2017](#)] is an algorithm developed for measuring and search for gravitational arcs, whose operation is based on the geometric property of the perpendicular bisector of a pair of points in a circle. In this case, for any pair of points the lines that mark the perpendicular bisector always intersect in the center of the circle. Starting from this idea one can decompose an elongated object into a set of points along its length using an iterative method that uses recurrently bisectors between points of the object to create new points. If this object is an arc shaped segment the perpendicular bisector to the pairs of points will intersect points near the center of curvature. An advantage is that this method can be used to determine segments along the extension of elongated object, i.e. to “filament” an object regardless of the presence of curvature.

The output of Mediatrix is a set of N vectors \mathbf{n}_i with $|\mathbf{n}_i| = l_i$, where l_i is the distance between pairs of neighboring perpendicular bisector points. The orientation is perpendicular to l_i and its origin is in the midpoint of l_i .

We can define a center of curvature based on all Mediatrix filament points, i.e. the point that minimizes the distance to the lines defined by vectors \mathbf{n}_i . For this purpose the following function is defined

$$M(\mathbf{r}) := \frac{1}{N} \sum_{i=1}^N |\mathbf{d}(\mathbf{r}, \mathbf{n}_i)|^2, \quad (\text{B.1})$$

where $|\mathbf{d}|$ is the distance from the point \mathbf{r} to the line defined by \mathbf{n}_i (see Figure B.2). The center of curvature is defined as the point \mathbf{r}_0 which minimizes $M(\mathbf{r})$.

This center of curvature defines a curvature radius r_{arc} , in the case of gravitational arcs, which can

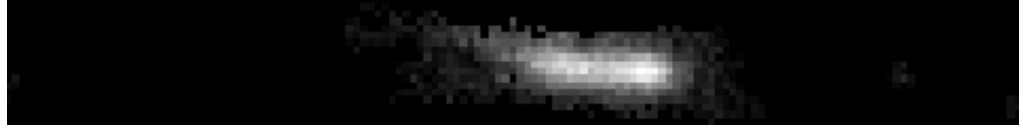


FIGURE B.3: Example of an input image for Mediatrix from a arc in SOGRAS/GEMINI. In this image there is another detected object in the image, which causes Mediatrix to not correctly determine the extremes of the main object.

be seen as an approximation to the Einstein radius θ_E of the system. Thus, $\theta_E \sim r_{arc}$, and the mass within this radius can be obtained by the expression

$$M(r_{arc}) = \Sigma_{crit}\pi(D_l r_{arc})^2. \quad (\text{B.2})$$

Then, we can compare this mass estimate with those from the inverse modeling of lenses or from the dynamic masses estimates.

In the SOGRAS survey, 8 clusters with gravitational arcs were identified. From these, four were observed with the Gemini Multi-Object Spectrograph (GMOS) telescope with the GEMINI telescope. These images are deeper and with better resolution, in addition, the spectra of the cluster member galaxies were taken, allowing the determination of their dynamical masses.

We use these images with better quality to apply Mediatrix. To have a good result, we need the arcs to be well segmented with SExtractor, e.g. to use a configuration that does not “break” the arcs. We need to cut the input images so that we have only one arc in each Mediatrix input, without contamination with neighboring objects, as this may hinder the determination of the extremes of the object. In Figure B.3, we show an example of an object that was not well separated to be a Mediatrix input image.

At the moment, we are determining the best configurations and cuts in the input images of the SOGRAS/GEMINI samples. After these tests, running Mediatrix in this sample is a relatively straightforward process, since this code was developed in Python by our group and is available in the *SLtools* library.

Appendix C

List of publications and talks

First author papers

- **M. E. S. Pereira**, M. Soares-Santos, M. Makler, J. Annis, H. Lin, A. Palmese, A. Z. Vitorelli, B. Welch, G. B. Caminha, T. Erben, B. Moraes and H. Shan. *Weak-lensing calibration of a stellar mass-based mass proxy for redMaPPer and Voronoi Tessellation clusters in SDSS Stripe 82*. MNRAS, Volume 474, Issue 1, Pages 1361–1372, Feb 2018.

Papers in preparation

- **M. E. S. Pereira** and the SOGRAS team. *The SOAR Gravitational Arc Survey - II: The Strong Lensing Sample*. In preparation.

Published co-authored papers

- C. Wang, R. Li, L. Gao, H. Shan, J.-P. Kneib, W. Wang, G. Chen, M. Makler, **M. E. S. Pereira**, L. Wang, M. Maia and T. Erben. *Do satellite galaxies trace matter in galaxy clusters*. MNRAS, volume 475, Issue 1, pages 4020–4026, Apr 2018 .
- J. Y. H. Soo , B. Moraes, B. Joachimi, W. Hartley, O. Lahav, A. Charbonnier, M. Makler, **M. E. S. Pereira**, J. Comparat, T. Erben, A. Leauthaud, H. Shan and L. Van Waerbeke. *Morpho-z: improving photometric redshifts with galaxy morphology*. MNRAS, volume 475, Issue 1, pages 3613–3632, Apr 2018.

- A. Z. Vitorelli, E. S. Cypriano, M. Makler, **M. E. S. Pereira**, T. Erben and B. Moraes. *On Mass Concentrations & Magnitude Gaps of Galaxy Systems in the CS82 Survey.* MNRAS, volume 474, Issue 1, pages 866–875, Feb 2018.
- A. Niemiec, E. Jullo, M. Limousin, C. Giocoli, T. Erben, H. Hildebrandt, J-P. Kneib, A. Leauthaud, M. Makler, B. Moraes, **M. E. S. Pereira**, H. Shan, E. Rozo, E. Rykoff, L. Van Waerbeke. *Stellar-to-halo mass relation of cluster galaxies.* MNRAS, Volume 471, Issue 1, Pages 1153–1166, October 2017.
- A. Charbonnier, M. H. Company, T. S. Gonçalves, K. Bundy, K. Menéndez-Delmestre, E. Galliano, B. Moraes, **M. E. S. Pereira**, M. Makler, T. Erben, H. Hildebrandt, H. Shan, G. B. Caminha, M. Grossi, L. Riguccini. *The abundance of compact quiescent galaxies since $z \sim 0.6$.* MNRAS, Volume 469, Issue 4, Pages 4523–4536, August 2017.
- J. Geach, Y-T. Lin, M. Makler, J-P. Kneib, N. Ross, W-H. Wang, B-C. Hsieh, A. Leauthaud, K. Bundy, H. McCracken, J. Comparat, G. Caminha, P. Hudelot, L. Lin, L. Van Waerbeke, **M. E. S. Pereira**, D. Mast. *VICS82: the VISTA-CFHT Stripe 82 near-infrared survey.* ApJS, Volume 231, Issue 1, article id. 7, 10 pp, July 2017
- H. Shan, J-P. Kneib, R. Li, J. Comparat, T. Erben, M. Makler, B. Moraes, L. Van Waerbeke, J. E. Taylor, A. Charbonnier, **M. E. S. Pereira**. *The Mass-Concentration Relation and the Stellar-to-Halo Mass Ratio in the CFHT Stripe 82 Survey.* ApJ, Volume 840, Issue 2, article id. 104, 9 pp, May 2017.
- A. Leauthaud, S. Saito , S. Hilbert , A. Barreira, S. More, M. White, S. Alam, P. Behroozi, K. Bundy, J. Coupon, T. Erben, C. Heymans, H. Hildebrandt, R. Mandelbaum, B. Moraes, **M. E. S. Pereira**, S. A. Rodríguez-Torres, H. Shan. *Lensing is Low: Cosmology, Galaxy Formation, or New Physics?.* MNRAS, Volume 467, Issue 3, pages 3024-3047, May 2017.
- B. Nord, E. Buckley-Geer, H. Lin, H. T. Diehl, J. Helsby, N. Kuropatkin, A. Amara, T. Collett, S. Allam, G. B. Caminha, C. De Bom, S. Desai H. Dúmet-Montoya, **M. E. S. Pereira**, and The DES Collaboration. *Observation and Confirmation of Six Strong-lensing Systems in the Dark Energy Survey Science Verification Data.* ApJ, Volume 827, Issue 1, article id. 51, 16 pp, August 2016.
- J. Comparat, E. Jullo, J.-P. Kneib, C. Schimd, H. Shan, T. Erben, O. Ilbert, J. Brownstein, A. Ealet, S. Escoffier, B. Moraes, N. Mostek J. A. Newman, **M. E. S. Pereira**, F. Prada, D. J. Schlegel, D. P. Schneider, and C. H. Brandt. *Stochastic bias of colour-selected BAO tracers by*

joint clustering-weak lensing analysis. MNRAS, Volume 433, Issue 2, pages 1146-1160, August 2013.

- C. Furlanetto, B. X. Santiago, M. Makler, E. S. Cypriano, G. B. Caminha, **M. E. S. Pereira**, A. F. Neto, J. Estrada, H. Lin, J. Hao, T. A. McKay, L. N. da Costa and M. A. G. Maia. *The SOAR Gravitational Arc Survey - I. Survey overview and photometric catalogues.* MNRAS, Volume 432, Issue 1, pages 73-88, June 2013.

Submitted co-authored papers

- A. Niemiec, E. Jullo, L. Gao, A. D. Montero-Dorta, S. Rodriguez-Torres, E. Perez, A. Klypin, T. Erben, M. Makler, B. Moraes, **M. E. S. Pereira** and H. Shan. *Probing galaxy assembly bias with LRG weak lensing observations.* Accepted for publication in MNRAS, April 2018.
- M. Chalela, E. J. Gonzalez, M. Makler, D. G. Lambas, **M. E. S. Pereira**, A. O'mill and H. Shan. *Compact Groups analysis using weak gravitational lensing II: CFHT Stripe82 data.* Submitted for MNRAS, March 2018.

Presentations at conferences and workshops

- Jul 2017: School on Open Problems in Cosmology, ICTP/SAIFR, São Paulo, Brazil. *Weak-lensing mass calibration of redMaPPer and Voronoi Tessellation clusters in SDSS Stripe 82.*
- Aug 2016: Astro Hack Week 2016, University of California, Berkeley, USA. *Density profile-fitting from cluster weak lensing.*
- Jul 2016: 21st International Conference on General Relativity and Gravitation, Columbia University, New York, USA. *Density profiles of galaxy clusters in the CFHT Stripe 82 survey from weak gravitational lensing.*
- Apr 2016: Third Argentinian-Brazilian Meeting on Gravitation, Astrophysics and Cosmology, Brazilian Center for Physics Research, Rio de Janeiro, Brazil. *Weak lensing signal of Voronoi-selected galaxy clusters [un]detected by red-sequence algorithm.*
- Sep 2015: Astro Hack Week 2015, New York University, New York, USA. *Bayesian inference 4 dummies.*

- Apr 2014: ICRA10, Brazilian Center for Physics Research, Rio de Janeiro, Brazil. *Measuring galaxy morphologies in the CFHT Stripe-82 Survey.*
- Oct 2013: VI International Workshop on Astronomy and Relativistic Astrophysics, Brazilian Center for Physics Research, Rio de Janeiro, Brazil. *Measuring galaxy morphologies in the CFHT/MegaCam Stripe-82 Survey.*
- Jul 2013: Post-Planck Cosmology, École de Physique des Houches, Les Houches, France. *Galaxy morphology on CS82 survey.*

Bibliography

- Abazajian, K. et al. (2003). The First Data Release of the Sloan Digital Sky Survey. *AJ*, 126:2081–2086.
- Aihara, H. et al. (2011). The Eighth Data Release of the Sloan Digital Sky Survey: First Data from SDSS-III. *ApJS*, 193:29.
- Albareti, F. D. et al. (2017). The 13th Data Release of the Sloan Digital Sky Survey: First Spectroscopic Data from the SDSS-IV Survey Mapping Nearby Galaxies at Apache Point Observatory. *ApJS*, 233:25.
- Alcock, C. et al. (1993). Possible gravitational microlensing of a star in the Large Magellanic Cloud. *Nature*, 365:621–623.
- Allen, S. W., Evrard, A. E., and Mantz, A. B. (2011). Cosmological Parameters from Observations of Galaxy Clusters. *ARA&A*, 49:409–470.
- Andreon, S. (2012). A low-scatter survey-based mass proxy for clusters of galaxies. *A&A*, 548:A83.
- Annis, J. et al. (2014). The Sloan Digital Sky Survey Coadd: 275 deg² of Deep Sloan Digital Sky Survey Imaging on Stripe 82. *ApJ*, 794:120.
- Barnothy, J. M. (1965). Quasars and the Gravitational Image Intensifier. *AJ*, 70:666.
- Bartelmann, M. (1996). Arcs from a universal dark-matter halo profile. *A&A*, 313:697–702.
- Battaglia, N. et al. (2016). Weak-lensing mass calibration of the Atacama Cosmology Telescope equatorial Sunyaev-Zeldovich cluster sample with the Canada-France-Hawaii telescope stripe 82 survey. *J. Cosmology Astropart. Phys.*, 8:013.
- Benítez, N. (2000). Bayesian Photometric Redshift Estimation. *ApJ*, 536:571–583.

- Benjamin, J. et al. (2013). CFHTLenS tomographic weak lensing: quantifying accurate redshift distributions. *MNRAS*, 431:1547–1564.
- Binney, J. and Tremaine, S. (1987). Galactic dynamics.
- Blandford, R. and Narayan, R. (1986). Fermat’s principle, caustics, and the classification of gravitational lens images. *ApJ*, 310:568–582.
- Blanton, M. R. and Roweis, S. (2007). K-Corrections and Filter Transformations in the Ultraviolet, Optical, and Near-Infrared. *AJ*, 133:734–754.
- Bom, C. R. et al. (2017). A neural network gravitational arc finder based on the Mediatrix filamentation method. *A&A*, 597:A135.
- Bom, C. R., Makler, M., and Albuquerque, M. P. (2012). Mediatrix method for filamentation of objects in images. ArXiv e-prints: 1212.1799.
- Bond, I. A. et al. (2004). OGLE 2003-BLG-235/MOA 2003-BLG-53: A Planetary Microlensing Event. *ApJ*, 606:L155–L158.
- Bradac, M. (2004). Exploring Dark Matter Properties from the Smallest to the Largest Scales. PhD thesis, Rheinischen Friedrich-Wilhelms Universität Bonn, Bonn.
- Bridle, S. et al. (2009). Handbook for the GREAT08 Challenge: An image analysis competition for cosmological lensing. *Annals of Applied Statistics*, 3:6–37.
- Bridle, S. et al. (2010). Results of the GREAT08 Challenge: an image analysis competition for cosmological lensing. *MNRAS*, 405:2044–2061.
- Bundy, K. et al. (2015). The Stripe 82 Massive Galaxy Project. I. Catalog Construction. *ApJS*, 221:15.
- Caminha, G. B. (2009). Cálculo da abundância de arcos gravitacionais em aglomerados de galáxias. PhD thesis, Centro Brasileiro de Pesquisas Físicas, Rio de Janeiro.
- Caminha, G. B. (2014). Um Prelúdio para o Lenteamento Gravitacional Forte em Levantamentos de Grandes Áreas. PhD thesis, Centro Brasileiro de Pesquisas Físicas, Rio de Janeiro.
- Charbonnier, A. et al. (2017). The abundance of compact quiescent galaxies since $z \sim 0.6$. *MNRAS*, 469:4523–4536.

- Chwolson, O. (1924). Über eine mögliche Form fiktiver Doppelsterne. *Astronomische Nachrichten*, 221:329.
- Cibirka, N. (2013). Espectroscopia Multi-objeto de Aglomerados de Galáxias com Arcos Gravitacionais. Master's thesis, Universidade de São Paulo, São Paulo.
- Clampitt, J. and Jain, B. (2015). Lensing measurements of the mass distribution in SDSS voids. *MNRAS*, 454:3357–3365.
- Coil, A. L. et al. (2011). The PRISM Multi-object Survey (PRIMUS). I. Survey Overview and Characteristics. *ApJ*, 741:8.
- Colless, M. et al. (2001). The 2dF Galaxy Redshift Survey: spectra and redshifts. *MNRAS*, 328:1039–1063.
- Comparat, J. et al. (2013). Stochastic bias of colour-selected BAO tracers by joint clustering-weak lensing analysis. *MNRAS*, 433:1146.
- Conroy, C. (2013). Modeling the Panchromatic Spectral Energy Distributions of Galaxies. *ARA&A*, 51:393–455.
- Cornell, J. and Lightman, A. (1983). Revealing the Universe: Prediction and Proof in Astronomy. The MIT Press.
- Croom, S. M. et al. (2001). The 2dF QSO Redshift Survey - V. The 10k catalogue. *MNRAS*, 322:L29–L36.
- Croom, S. M. et al. (2004). The 2dF QSO Redshift Survey - XII. The spectroscopic catalogue and luminosity function. *MNRAS*, 349:1397–1418.
- Croom, S. M. et al. (2009a). The 2dF-SDSS LRG and QSO Survey: the spectroscopic QSO catalogue. *MNRAS*, 392:19–44.
- Croom, S. M., Richards, G. T., et al. (2009b). The 2dF-SDSS LRG and QSO Survey: the spectroscopic QSO catalogue. *MNRAS*, 392:19–44.
- de Jong, J. T. A. et al. (2013). The Kilo-Degree Survey. *The Messenger*, 154:44–46.
- de la Torre, S. et al. (2013). The VIMOS Public Extragalactic Redshift Survey (VIPERS). Galaxy clustering and redshift-space distortions at $z \simeq 0.8$ in the first data release. *A&A*, 557:A54.

- Diemer, B. (2015). Colossus: COsmology, haLO, and large-Scale StrUcture toolsS. *Astrophysics Source Code Library*.
- Dietrich, J. P. et al. (2007). BLOX: the Bonn lensing, optical, and X-ray selected galaxy clusters. I. Cluster catalog construction. *A&A*, 470:821–834.
- Drinkwater, M. J. et al. (2010). The WiggleZ Dark Energy Survey: survey design and first data release. *MNRAS*, 401:1429–1452.
- Duffy, A. R. et al. (2008). Dark matter halo concentrations in the Wilkinson Microwave Anisotropy Probe year 5 cosmology. *MNRAS*, 390:L64–L68.
- Dyson, F. W., Eddington, A. S., and Davidson, C. (1920). A Determination of the Deflection of Light by the Sun's Gravitational Field, from Observations Made at the Total Eclipse of May 29, 1919. *Philosophical Transactions of the Royal Society of London A: Mathematical, Physical and Engineering Sciences*, 220(571-581):291–333.
- Eddington, A. (1921). *Space, Time and Gravitation: An Outline of the General Relativity Theory*. University Press.
- Einasto, J. (1965). On the Construction of a Composite Model for the Galaxy and on the Determination of the System of Galactic Parameters. *Trudy Astrofizicheskogo Instituta Alma-Ata*, 5:87–100.
- Einstein, A. (1911). Über den Einfluß der Schwerkraft auf die Ausbreitung des Lichtes. *Annalen der Physik*, 340(10):898–908.
- Einstein, A. (1916). Die Grundlage der allgemeinen Relativitätstheorie. *Annalen der Physik*, 49:771.
- Einstein, A. (1936). Lens-Like Action of a Star by the Deviation of Light in the Gravitational Field. *Science*, 84:506–507.
- Eisenstein, D. J. et al. (2011). SDSS-III: Massive Spectroscopic Surveys of the Distant Universe, the Milky Way, and Extra-Solar Planetary Systems. *AJ*, 142:72.
- Erben, T. et al. (2009). CARS: the CFHTLS-Archive-Research Survey. I. Five-band multi-colour data from 37 sq. deg. CFHTLS-wide observations. *A&A*, 493:1197–1222.
- Erben, T. et al. (2013). CFHTLenS: the Canada-France-Hawaii Telescope Lensing Survey - imaging data and catalogue products. *MNRAS*, 433:2545–2563.

- Erben, T. et al. (2018). The CFHT Stripe 82 Survey. In preparation.
- Ettori, S. and Meneghetti, M. (2013). Preface. *Space Sci. Rev.*, 177:1–2.
- Falco, E. E., Gorenstein, M. V., and Shapiro, I. I. (1985). On model-dependent bounds on $H(0)$ from gravitational images Application of Q0957 + 561A,B. *ApJ*, 289:L1–L4.
- Figueiró, P. S. (2011). Weak Lensing Analysis of Galaxy Groups. PhD thesis, Ludwig-Maximilians-Universität München, Munich.
- Ford, J. et al. (2014). Cluster magnification and the mass-richness relation in CFHTLenS. *MNRAS*, 439:3755–3764.
- Ford, J. et al. (2015). CFHTLenS: a weak lensing shear analysis of the 3D-Matched-Filter galaxy clusters. *MNRAS*, 447:1304–1318.
- Ford, J. and VanderPlas, J. (2016). Cluster-lensing: A Python Package for Galaxy Clusters and Miscentering. *AJ*, 152:228.
- Foreman-Mackey, D. (2016). corner.py: Scatterplot matrices in python. *The Journal of Open Source Software*, 1(2).
- Fortune, S. (1986). A Sweepine Algorithm for Voronoi Diagrams. In Proceedings of the Second Annual Symposium on Computational Geometry, SCG '86, pages 313–322.
- Frieman, J. A. et al. (2008). The Sloan Digital Sky Survey-II Supernova Survey: Technical Summary. *AJ*, 135:338–347.
- Furlanetto, C. et al. (2013). The SOAR Gravitational Arc Survey - I. Survey overview and photometric catalogues. *MNRAS*, 432:73–88.
- Garilli, B. et al. (2008). The Vimos VLT deep survey. Global properties of 20,000 galaxies in the $I_{AB} < 22.5$ WIDE survey. *A&A*, 486:683–695.
- Geach, J. E. et al. (2017). VICS82: The VISTA-CFHT Stripe 82 Near-infrared Survey. *ApJS*, 231:7.
- Gladders, M. D. and Yee, H. K. C. (2000). A New Method For Galaxy Cluster Detection. I. The Algorithm. *AJ*, 120:2148–2162.
- Gonzalez, E. J. et al. (2017). Weak-lensing measurement of the mass-richness relation using the SDSS data base. *MNRAS*, 465:1348–1357.

- Haiman, Z., Mohr, J. J., and Holder, G. P. (2001). Constraints on Cosmological Parameters from Future Galaxy Cluster Surveys. *ApJ*, 553:545–561.
- Hao, J. et al. (2010). A GMBCG Galaxy Cluster Catalog of 55,424 Rich Clusters from SDSS DR7. *ApJS*, 191:254–274.
- Harvey, D. et al. (2015). The nongravitational interactions of dark matter in colliding galaxy clusters. *Science*, 347:1462–1465.
- Hastings, W. K. (1970). Monte Carlo Sampling Methods Using Markov Chains and Their Applications. *Biometrika*, 57(1):97–109.
- Hewitt, J. N. et al. (1988). Unusual radio source MG1131+0456 - A possible Einstein ring. *Nature*, 333:537–540.
- Heymans, C. et al. (2006). The Shear Testing Programme - I. Weak lensing analysis of simulated ground-based observations. *MNRAS*, 368:1323–1339.
- Heymans, C. et al. (2012). CFHTLenS: the Canada-France-Hawaii Telescope Lensing Survey. *MNRAS*, 427:146–166.
- Hildebrandt, H. et al. (2012). CFHTLenS: improving the quality of photometric redshifts with precision photometry. *MNRAS*, 421:2355–2367.
- Hudson, M. J. et al. (2015). CFHTLenS: co-evolution of galaxies and their dark matter haloes. *MNRAS*, 447:298–314.
- Irwin, M. J. et al. (1989). Photometric variations in the Q2237 + 0305 system - First detection of a microlensing event. *AJ*, 98:1989–1994.
- Jaki, S. (1978). Johann Georg von Soldner and the gravitational bending of light, with an English translation of his essay on it published in 1801. *Foundations of Physics*, 8:927–950.
- Jarvis, M. et al. (2016). The DES Science Verification weak lensing shear catalogues. *MNRAS*, 460:2245–2281.
- Johnston, D. E. et al. (2007). Cross-correlation Weak Lensing of SDSS galaxy Clusters II: Cluster Density Profiles and the Mass–Richness Relation. *ArXiv e-prints*: 0709.1159.
- Jones, D. H. et al. (2009). The 6dF Galaxy Survey: final redshift release (DR3) and southern large-scale structures. *MNRAS*, 399:683–698.

- Kaiser, N., Squires, G., and Broadhurst, T. (1995). A Method for Weak Lensing Observations. *ApJ*, 449:460.
- Kelly, P. L. et al. (2015). Multiple images of a highly magnified supernova formed by an early-type cluster galaxy lens. *Science*, 347(6226):1123–1126.
- Kettula, K. et al. (2015). CFHTLenS: weak lensing calibrated scaling relations for low-mass clusters of galaxies. *MNRAS*, 451:1460–1481.
- Kitching, T. D. et al. (2008). Bayesian galaxy shape measurement for weak lensing surveys - II. Application to simulations. *MNRAS*, 390:149–167.
- Kitching, T. D. et al. (2012). Image analysis for cosmology: results from the GREAT10 Galaxy Challenge. *MNRAS*, 423:3163–3208.
- Kneib, J.-P. et al. (1996). Hubble Space Telescope Observations of the Lensing Cluster Abell 2218. *ApJ*, 471(2):643.
- Kneib, J.-P. et al. (2010). CFHT Megacam High-Resolution Imaging of the SDSS Stripe 82. CFHT programs 10BF023, 10BC022, 10BB009.
- Koester, B. P. et al. (2007). A MaxBCG Catalog of 13,823 Galaxy Clusters from the Sloan Digital Sky Survey. *ApJ*, 660:239–255.
- Kormann, R., Schneider, P., and Bartelmann, M. (1994). Isothermal elliptical gravitational lens models. *A&A*, 284:285–299.
- Kravtsov, A. V. and Borgani, S. (2012). Formation of Galaxy Clusters. *ARA&A*, 50:353–409.
- Kuijken, K. (2006). Shears from shapelets. *A&A*, 456:827–838.
- Kuijken, K. et al. (2015). Gravitational lensing analysis of the Kilo-Degree Survey. *MNRAS*, 454:3500–3532.
- LaMassa, S. M. et al. (2016). The 31 Deg² Release of the Stripe 82 X-Ray Survey: The Point Source Catalog. *ApJ*, 817:172.
- Lawrence, A. et al. (2007). The UKIRT Infrared Deep Sky Survey (UKIDSS). *MNRAS*, 379:1599–1617.
- Le Fèvre, O. et al. (2013). The VIMOS VLT Deep Survey final data release: a spectroscopic sample of 35 016 galaxies and AGN out to $z \sim 6.7$ selected with $17.5 \leq i_{AB} \leq 24.75$. *A&A*, 559:A14.

- Leauthaud, A. et al. (2017). Lensing is low: cosmology, galaxy formation or new physics? *MNRAS*, 467:3024–3047.
- Lee, M. and Wagenmakers, E. (2014). *Bayesian Cognitive Modeling: A Practical Course*. Cambridge University Press.
- Li, R. et al. (2016). Measuring subhalo mass in redMaPPer clusters with CFHT Stripe 82 Survey. *MNRAS*, 458:2573–2583.
- Liu, X. et al. (2015). Cosmological constraints from weak lensing peak statistics with Canada-France-Hawaii Telescope Stripe 82 Survey. *MNRAS*, 450:2888–2902.
- Lynds, R. and Petrosian, V. (1986). Giant Luminous Arcs in Galaxy Clusters. In *Bulletin of the American Astronomical Society*, volume 18 of *BAAS*, page 1014.
- Mandelbaum, R. et al. (2010). Precision cluster mass determination from weak lensing. *MNRAS*, 405:2078–2102.
- Mandelbaum, R. et al. (2014). The Third Gravitational Lensing Accuracy Testing (GREAT3) Challenge Handbook. *ApJS*, 212:5.
- Marshall, P. J. (2003). Bayesian Analysis of Clusters of Galaxies. PhD thesis, University of Cambridge, Cambridge.
- Melchior, P. et al. (2014). First measurement of gravitational lensing by cosmic voids in SDSS. *MNRAS*, 440:2922–2927.
- Melchior, P. et al. (2017). Weak-lensing mass calibration of redMaPPer galaxy clusters in Dark Energy Survey Science Verification data. *MNRAS*, 469:4899–4920.
- Menci, N. et al. (2016). A Stringent Limit on the Warm Dark Matter Particle Masses from the Abundance of $z = 6$ Galaxies in the Hubble Frontier Fields. *ApJ*, 825:L1.
- Mendes de Oliveira, C. et al. (2018). The Southern Photometric Local Universe Survey. In preparation.
- Merritt, D. et al. (2006). Empirical Models for Dark Matter Halos. I. Nonparametric Construction of Density Profiles and Comparison with Parametric Models. *ApJ*, 132:2685–2700.
- Metropolis, N. et al. (1953). Equation of State Calculations by Fast Computing Machines. *The Journal of Chemical Physics*, 21(6):1087–1092.

- Miller, L. et al. (2007). Bayesian galaxy shape measurement for weak lensing surveys - I. Methodology and a fast-fitting algorithm. *MNRAS*, 382:315–324.
- Miller, L. et al. (2013). Bayesian galaxy shape measurement for weak lensing surveys - III. Application to the Canada-France-Hawaii Telescope Lensing Survey. *MNRAS*, 429:2858–2880.
- Miralda-Escude, J. (1991). Gravitational lensing by clusters of galaxies - Constraining the mass distribution. *ApJ*, 370:1–14.
- Mollerach, S. and Roulet, E. (2002). *Gravitational Lensing and Microlensing*. World Scientific.
- Montoya, H. S. D. (2011). Modelagens Semianalíticas para Arcos Gravitacionais: Seção de Choque e Método Perturbativo em Lentes Pseudoelípticas. PhD thesis, Centro Brasileiro de Pesquisas Físicas, Rio de Janeiro.
- Moraes, B. et al. (2014). The CFHT/MegaCam Stripe-82 Survey. In *Revista Mexicana de Astronomía y Astrofísica Conference Series*, volume 44, pages 202–203.
- Moraes, B. et al. (2018). CS82 Morphology Catalogue. In preparation.
- Moreira, I. d. C. and Videira, A. A. P. (1995). *Einstein e o Brasil*. Editora UFRJ.
- Narayan, R. and Bartelmann, M. (1996). Lectures on Gravitational Lensing. ArXiv e-prints: 9606001.
- Navarro, J. F., Frenk, C. S., and White, S. D. M. (1996). The Structure of Cold Dark Matter Halos. *ApJ*, 462:563.
- Newman, J. A. et al. (2013). The DEEP2 Galaxy Redshift Survey: Design, Observations, Data Reduction, and Redshifts. *ApJS*, 208:5.
- Niemiec, A. et al. (2017). Stellar-to-halo mass relation of cluster galaxies. *MNRAS*, 471:1153–1166.
- Nord, B. et al. (2016). Observation and Confirmation of Six Strong-lensing Systems in the Dark Energy Survey Science Verification Data. *ApJ*, 827:51.
- Oguri, M. (2014). A cluster finding algorithm based on the multiband identification of red sequence galaxies. *MNRAS*, 444:147–161.
- Palmese, A. et al. (2016). Comparing Dark Energy Survey and HST-CLASH observations of the galaxy cluster RXC J2248.7-4431: implications for stellar mass versus dark matter. *MNRAS*, 463:1486–1499.

- Palmese, A. et al. (2018). Stellar mass as a galaxy cluster mass proxy and stellar-to-halo connection in the Dark Energy Survey redMaPPer clusters. In preparation.
- Penna-Lima, M., Makler, M., and Wuensche, C. A. (2014). Biases on cosmological parameter estimators from galaxy cluster number counts. *J. Cosmology Astropart. Phys.*, 5:039.
- Pereira, M. E. S. (2012). Determinação da Elipticidades Intrínsecas das Galáxias para Medidas do Lenteamento Gravitacional Fraco. Master's thesis, Centro Brasileiro de Pesquisas Físicas, Rio de Janeiro.
- Pereira, M. E. S. et al. (2018a). The SOAR Gravitational Arc Survey - II: The Strong Lensing Sample. In preparation.
- Pereira, M. E. S. et al. (2018b). Weak-lensing calibration of a stellar mass-based mass proxy for redMaPPer and Voronoi Tessellation clusters in SDSS Stripe 82. *MNRAS*, 474:1361–1372.
- Petters, A., Levine, H., and Wambsganss, J. (2001). Singularity Theory and Gravitational Lensing. *Progress in Mathematical Physics*. Birkhäuser Boston.
- Pizzuti, L. et al. (2016). CLASH-VLT: testing the nature of gravity with galaxy cluster mass profiles. *J. Cosmology Astropart. Phys.*, 4:023.
- Ramella, M. et al. (1999). Cluster Identification via Voronoi Tesselation. In *Observational Cosmology: The Development of Galaxy Systems*, volume 176 of *Astronomical Society of the Pacific Conference Series*, page 108.
- Refsdal, S. (1964). On the Possibility of Determining Hubble's Parameter and the Masses of Galaxies from the Gravitational Lens Effect. *MNRAS*, 128(4):307–310.
- Refsdal, S. (1964). The gravitational lens effect. *MNRAS*, 128:295.
- Refsdal, S. and Surdej, J. (1994). Gravitational lenses. *Reports on Progress in Physics*, 57(2):117.
- Reis, R. R. R. et al. (2012). The Sloan Digital Sky Survey Co-add: A Galaxy Photometric Redshift Catalog. *ApJ*, 747:59.
- Reyes, R. et al. (2012). Optical-to-virial velocity ratios of local disc galaxies from combined kinematics and galaxy-galaxy lensing. *MNRAS*, 425:2610–2640.
- Robert, C. P. (2015). The Metropolis-Hastings algorithm. ArXiv e-prints: 1504.01896.

- Roediger, J. C. et al. (2017). The Next Generation Virgo Cluster Survey (NGVS). XXIV. The Red Sequence to $\sim 10^6 L_\odot$ and Comparisons with Galaxy Formation Models. *ApJ*, 836:120.
- Rozo, E. and Rykoff, E. S. (2014). redMaPPer II: X-Ray and SZ Performance Benchmarks for the SDSS Catalog. *ApJ*, 783:80.
- Rykoff, E. S. et al. (2012). Robust Optical Richness Estimation with Reduced Scatter. *ApJ*, 746:178.
- Rykoff, E. S. et al. (2014). redMaPPer. I. Algorithm and SDSS DR8 Catalog. *ApJ*, 785:104.
- Rykoff, E. S. et al. (2016). The RedMaPPer Galaxy Cluster Catalog From DES Science Verification Data. *ApJS*, 224:1.
- Saro, A. et al. (2015). Constraints on the richness-mass relation and the optical-SZE positional offset distribution for SZE-selected clusters. *MNRAS*, 454:2305–2319.
- Schmidt, M. (1963). 3C 273 : A Star-Like Object with Large Red-Shift. *Nature*, 197:1040.
- Schneider, P. (2005). Weak Gravitational Lensing. ArXiv e-prints: 0509252.
- Schneider, P., Ehlers, J., and Falco, E. E. (1992). Gravitational Lenses. Springer-Verlag.
- Schneider, P. and Seitz, C. (1995). Steps towards nonlinear cluster inversion through gravitational distortions. 1: Basic considerations and circular clusters. *A&A*, 294:411–431.
- Shan, H. et al. (2017). The Mass-Concentration Relation and the Stellar-to-halo Mass Ratio in the CFHT Stripe 82 Survey. *ApJ*, 840:104.
- Sheldon, E. S. et al. (2001). Weak-Lensing Measurements of 42 SDSS/RASS Galaxy Clusters. *ApJ*, 554:881–887.
- Simet, M. et al. (2012). The Sloan Digital Sky Survey Co-add: Cross-correlation Weak Lensing and Tomography of Galaxy Clusters. *ApJ*, 748:128.
- Simet, M. et al. (2017). Weak lensing measurement of the mass-richness relation of SDSS redMaPPer clusters. *MNRAS*, 466:3103–3118.
- Soares-Santos, M. et al. (2011). The Voronoi Tessellation Cluster Finder in 2+1 Dimensions. *ApJ*, 727:45.
- Soo, J. Y. H. et al. (2018). Morpho-z: improving photometric redshifts with galaxy morphology. *MNRAS*, 475:3613–3632.

- Soucail, G. et al. (1987). A blue ring-like structure, in the center of the A 370 cluster of galaxies. *A&A*, 172:L14–L16.
- Stott, J. P. et al. (2009). The evolution of the red sequence slope in massive galaxy clusters. *MNRAS*, 394:2098–2108.
- Timlin, J. D. et al. (2016). SpIES: The Spitzer IRAC Equatorial Survey. *ApJS*, 225:1.
- Tremaine, S. and Gunn, J. E. (1979). Dynamical role of light neutral leptons in cosmology. *Phys. Rev. Lett.*, 42:407–410.
- van de Weygaert, R. and Icke, V. (1989). Fragmenting the universe. II - Voronoi vertices as Abell clusters. *A&A*, 213:1–9.
- van Ravenzwaaij, D., Cassey, P., and Brown, S. D. (2018). A simple introduction to Markov Chain Monte–Carlo sampling. *Psychonomic Bulletin & Review*, 25(1):143–154.
- van Uitert, E. et al. (2012). Constraints on the shapes of galaxy dark matter haloes from weak gravitational lensing. *A&A*, 545:A71.
- Velander, M. et al. (2014). CFHTLenS: the relation between galaxy dark matter haloes and baryons from weak gravitational lensing. *MNRAS*, 437:2111–2136.
- Vitorelli, A. Z. et al. (2018). On mass concentrations and magnitude gaps of galaxy systems in the CS82 survey. *MNRAS*, 474:866–875.
- Voit, G. M. (2005). Tracing cosmic evolution with clusters of galaxies. *Rev. Mod. Phys.*, 77:207–258.
- Walsh, D., Carswell, R. F., and Weymann, R. J. (1979). 0957 + 561 A, B - Twin quasistellar objects or gravitational lens. *Nature*, 279:381–384.
- Wang, C. et al. (2018). Do satellite galaxies trace matter in galaxy clusters? *MNRAS*, 475:4020–4026.
- Welch, B. et al. (2018). 80,000 DES Clusters: redMaPPer red sequence properties using a new galaxy membership assignment algorithm. In preparation.
- Wiesner, M. P., Lin, H., and Soares-Santos, M. (2015). Mass calibration of galaxy clusters at redshift 0.1–1.0 using weak lensing in the Sloan Digital Sky Survey Stripe 82 co-add. *MNRAS*, 452:701–714.
- Wright, C. O. and Brainerd, T. G. (2000). Gravitational Lensing by NFW Halos. *ApJ*, 534(1):34.

- Yang, X. et al. (2006). Weak lensing by galaxies in groups and clusters - I. Theoretical expectations. MNRAS, 373:1159–1172.
- Zheng, X. (2016). Pseudo-Marginal Metropolis-Hastings Approach and its Application to Bayesian Copula Model. PhD thesis, University of New South Wales, Sydney.
- Zitrin, A. et al. (2012). Miscentring in galaxy clusters: dark matter to brightest cluster galaxy offsets in 10 000 Sloan Digital Sky Survey clusters. MNRAS, 426:2944–2956.
- Zwicky, F. (1937a). Nebulae as gravitational lenses. Phys. Rev., 51:290–290.
- Zwicky, F. (1937b). On the probability of detecting nebulae which act as gravitational lenses. Phys. Rev., 51:679–679.